Analysis of New Microstrip Type Antennas Using the Modal Expansion Method

by

Yiyu Lin

A dissertation
presented to the University of Manitoba
in partial fulfillment of the
requirements for the degree of
Doctor of Philosophy
in
Electrical Engineering

Winnipeg, Manitoba, 1990

ISBN 0-315-71842-0

ANALYSIS OF NEW MICROSTRIP TYPE ANTENNAS USING THE MODAL EXPANSION METHOD

BY

YIYU LIN

A thesis submitted to the Faculty of Graduate Studies of the University of Manitoba in partial fulfillment of the requirements of the degree of

DOCTOR OF PHILOSOPHY

I hereby declare that I am the sole author of this dissertation.

I authorize the University of Manitoba to lend this dissertation to other institutions or individuals for the purpose of scholarly research.

Yiyu Lin

I further authorize the University of Manitoba to reproduce this dissertation by photocopying or by other means, in total or in part, at the request of other institutions or individuals for the purpose of scholarly research.

Yiyu Lin

Abstract

This dissertation investigates new microstrip type antennas and presents their analyses. They are the concentrically shorted circular patch antennas, annular rings shorted at the outer periphery and biconical microstrip antennas. In the analysis, the modal expansion method is used to obtain the characteristics of concentrically shorted circular patch microstrip antennas and annular ring patch antennas shorted at the outer periphery. The analytical results of these antennas for the dominant and higher modes are substantiated by experimental data. Their characteristics show that they are useful antennas with much more flexible and better performance properties than the conventional circular patch antennas. The comparison with the annular ring patch microstrip antennas indicates that their electrical performance parameters are sufficiently adjustable by a modification of the radius of the centrally shorted post or outerly shorted periphery. Their flexible characteristics can be used readily for different applications.

The analysis of biconical microstrip antennas is also presented. The investigation of biconical structures shows that for the nonzero order modes, which are of interest, only the radial *TE* modes can be excited. Also, it is found that for each nonzero *TE* mode, a unique nontrivial eigenvalue ν exists. The biconical microstrip antenna is then modeled as a resonant cavity bounded by a wall admittance at the spherical aperture surface. The wall admittance is found by the radiation power and the energies reactively stored outside the cavity. The electromagnetic fields inside the cavity are thus expanded in terms of the existing resonant modes in the spherical coordinates. It is found that they can provide superior properties, such as wider bandwidths and higher gains in the broadside direction. The analysis shows that the conical microstrip antenna, a special case of such antennas, is an excellent alternative for the circular patch antenna. They are also able to conform to the tip of high speed vehicles to provide desirable performances for practical applications.

Acknowledgements

The author wishes to express his sincere appreciation to Prof. L. Shafai of the Electrical and Computer Engineering Department, University of Manitoba, for his guidance, constant encouragement and constructive criticism, throughout all phases of this work.

The financial support by the Natural Science and Engineering Research Council of Canada in the form of Research Assistantship and also through the University of Manitoba in the form of University Fellowship are appreciated.

Table of Contents

Abstract iv
Acknowledgements v
Table of Contents vi
List of Figures v
List of Tables xv

Chapter 1: Introduction 1

1.1. **Introduction** 1

1.2. **The Statement of the Problem** 3

1.3. **The Analytic Methods Used in This Dissertation** 5

Chapter 2: Literature Review 7

2.1. **Definition of Microstrip Antennas** 7

2.2. **Advantages and Fundamental Limitations** 8

2.3. **Applications** 9

2.4. **Methods of Analyzing Microstrip Antennas** 9

Chapter 3: Characteristics of Concentrically Shorted Circular Patch Microstrip Antennas 17

3.1. **Introduction** 17

3.2. **Mode Charts and Modal Field Expressions** 18

3.3. **Input Impedance and Bandwidth** 22

3.4. Radiation Fields 24

3.5. Results and Discussion 29

3.6. Conclusion 36

Chapter 4: Characteristics of Annular Ring Patch Antennas Shorted at the Outer Periphery 50

4.1. Introduction 50

4.2. Modal Field Expressions and Input Impedance 51

4.3. The Wall Admittance 53

4.4. Radiation Fields 55

4.5. Results and Discussion 57

4.6. Conventional Annular Ring Microstrip Antennas 60

4.7. Conclusion 63

Chapter 5: Analysis of Biconical Microstrip Antennas 83

5.1. Introduction 83

5.2. Eigenvalues of Spherical Wave Eigenfunctions 84

5.2.1. The ϕ Dependent Characteristic Equations 85

5.2.2. Computation of the Eigenvalues ν 87

5.2.3. Results and Discussion 88

5.3. Modal Field Expressions 89

5.4. Wall Admittance of Biconical Microstrip Antennas 95

5.5. Input Impedance, Bandwidth and Radiation Patterns 101

5.6. Summary 118

Chapter 6: Summary and Further Work 123

6.1. **Summary** 123

6.2. **Recommendation for Further Research Work** 124

References 126

List of Figures

Figure		page
2.1	Conically depressed circular patch microstrip antenna	15
3.1	Microstrip circular patch with a central short	23
3.2	Network model over a narrowband for an isolated mode	23
3.3	Mapping of the complex planes	28
3.4	Mode chart of circular cavity with a central short	30
3.5	Input impedance of the TM_{11} mode for a circular patch antenna with a central short	31
3.6	Input impedance of the TM_{21} mode for a circular patch antenna with a central short	32
3.7a	Computed E_θ patterns of the TM_{11} mode for a circular patch antenna with a central short	37
3.7b	Computed E_ϕ patterns of the TM_{11} mode for a circular patch antenna with a central short	38
3.7c	Computed E_θ patterns of the TM_{11} mode for a circular patch antenna with a central short	39
3.7d	Computed E_ϕ patterns of the TM_{11} mode for a circular patch antenna with a central short	40
3.8a	Computed E_θ patterns of the TM_{21} mode for a circular patch antenna with a central short	41
3.8b	Computed E_ϕ patterns of the TM_{21} mode for a circular patch antenna with a central short	42
3.9a	Variation of efficiency and bandwidth with tickness for a circular patch antenna with a central short	43
3.9b	Variation of efficiency and bandwidth with ε_r for a circular patch antenna with a central short	44
3.10	Input resistance and frequency at resonance of the TM_{11} and TM_{21} modes	

for a circular patch antenna with a central short 45

3.11a Directivity and bandwidth of the TM_{11} mode for a circular patch antenna with a central short 46

3.11b Input resistance and frequency at resonance of the TM_{11} mode for a circular patch antenna with a central short 47

3.12a Directivity and bandwidth of the TM_{21} mode for a circular patch antenna with a central short 48

3.12b Input resistance and frequency at resonance of the TM_{21} mode for a circular patch antenna with a central short 49

4.1 Annular ring patch shorted at the outer periphery 52

4.2 Vertically cut cross sections for the ring patch antennas shorted at the outer or inner edge 52

4.3 Complementary screen. (a) infinite, thin conducting screen with aperture (b) Complement of screen with aperture. 56

4.4 The calculation of the effective radius b_e 56

4.5 Input impedance of the TM_{11} mode for a annular patch shorted at the outer periphery 65

4.6 Input resistance and frequency at resonance of the TM_{11} mode for annular ring patches shorted at the outer periphery 66

4.7 Outer radius and input resistance and frequency at resonance of TM_{11} for annular ring patches shorted at the outer periphery 67

4.8 Gain and Directivity of TM_{11} mode for annular ring patches shorted at the outer periphery 68

4.9 Bandwidth and efficiency at resonance of TM_{11} mode for annular ring patches shorted at the outer periphery 69

4.10 Computed radiation patterns of TM_{11} for annular ring patches shorted at the outer periphery at the resonant frequency of 3.1536 GHz 70

4.11 Computed radiation patterns of TM_{11} for annular ring patches shorted

	at the outer periphery at the resonant frequency of 3.1536 GHz	71
4.12	Computed radiation patterns of TM_{11} for annular ring patches shorted at the outer periphery at the resonant frequency of 3.1536 GHz	72
4.13	Measured radiation patterns of TM_{11} for annular ring patches shorted at the outer periphery at the resonant frequency of 3.1 GHz	73
4.14	Mode chart of TM_{1n} for annular ring antenna	74
4.15	Mode chart of TM_{n1} for annular ring antenna	75
4.16	Input resistance and frequency at resonance of TM_{11} for annular ring antennas	76
4.17	Directivity and bandwidth of TM_{11} for annular ring antennas	77
4.18	Input resistance and frequency at resonance of TM_{12} for annular ring antennas	78
4.19	Directivity and bandwidth of TM_{12} for annular ring antennas	79
4.20	Computed radiation patterns of TM_{11} for annular ring antennas where the outer radius is constant	80
4.21	Computed radiation patterns of TM_{12} for annular ring antennas where the outer radius is constant	81
4.22	Computed radiation patterns of TM_{11} for annular ring antennas at resonant frequency of 3.7428 GHz	82
5.1	The geometries of biconical and coaxial structures	86
5.2	Eigenvalues ν v.s. θ_1 for the geometry of Fig.4.1c	90
5.3	Eigenvalues ν v.s. θ_2 for the geometry of Fig.4.1a	91
5.4	Eigenvalues ν v.s. θ_2 for the geometry of Fig.4.1a	92
5.5	The geometry of the biconical microstrip antenna	93
5.6	The current loops and the fields outside the cavity	97
5.7	*EM* fields at the cavity aperture	102
5.8	Mode chart of the *TM* mode for fields outside the cavity	103
5.9	Normalized wall conductances and susceptances for $k_0 b = \pi$	104

5.10 Normalized wall conductances and susceptances for $k_0 b = \pi/2$ 105

5.11 Normalized wall conductances and susceptances for $\theta_2 = 90^0$ 106

5.11a Convergence of the wall conductances and susceptances for $\theta_2 = 90^0$ 107

5.12 Normalized wall conductances and susceptances for $\theta_2 = 120^0$ 108

5.12a Convergence of the wall conductances and susceptances for $\theta_2 = 120^0$ 109

5.13 Normalized wall conductances and susceptances for $\theta_2 = 135^0$ 110

5.13a Convergence of the wall conductances and susceptances for $\theta_2 = 135^0$ 111

5.14 Normalized wall conductances and susceptances for $\theta_2 = 150^0$ 112

5.14a Convergence of the wall conductances and susceptances for $\theta_2 = 150^0$ 113

5.15 Computed radiation patterns for $\theta_2 = 120^0$ 119

5.16 Computed radiation patterns for $\theta_2 = 120^0$ 120

5.17 Computed radiation patterns for $\theta_2 = 135^0$ 121

5.18 Computed radiation patterns for $\theta_2 = 150^0$ 122

List of Tables

Table		page
3.1	Comparison of the measured and calculated data for a circular patch antenna with a central short	33
3.2	Performance parameters of TM_{11} for circular patch antennas with different central shorts	34
4.1	Performance parameters of the TM_{12} mode for annular ring antennas	62
4.2	Performance parameters of the TM_{11} mode for annular ring antennas	62
5.1	Eigenvalues ν for the TE modes with $\Delta\theta = 6^0$	89
5.2	Near field characteristics of conical microstrip antennas	116
5.3	Near field characteristics of circular patch antennas with similar in size with the antennas in Table 5.2.	116
5.4	Near field characteristics of biconical microstrip antennas	117
5.5	Far field characteristics of biconical microstrip antennas	118

Chapter 1
Introduction

1.1. Introduction

In the past two decades, designing microwave antennas using microstrips has attracted intense attention and viable designs are incorporated in many systems, such as phased arrays. This new generation of antennas is known as microstrip antennas. The basic idea is that of utilizing a printed conductor on the upper surface of a dielectric substrate as the radiating element, with the opposite side of the substrate being backed by a conducting ground plate. This type of antennas is, sometimes, referred to as printed antennas due to the manufacturing process which is the same as that of printed circuits.

Microstrip antennas are popular, because of the following geometric properties. In general, they are low profile, and can be made conformal with the surface of vehicles so as not to disturb the aerodynamics of their host vehicles. Because of the compatibility of microstrip antennas with integrated electronics, together with their ease of fabrication and low cost, they have been widely used as radiating elements in numerous applications. They can be used in diverse equipment, from manpack microwave systems to very large phased arrays involving applications from medical instrumentation to military installations. They have enabled the use of the printed circuit technology that resulted in a considerable reduction of microwave antenna size and, consequently, the antenna system is no longer the most bulky device in the communication equipment.

Although their advantages are evident, this new generation of antennas has fundamental limitations in the electronic properties, compared with the traditional microwave antennas, such as reflector antennas. Since microstrip antennas are inherently resonant structures and electrically very thin (thus have small resonant volumes), the bandwidth of microstrip antennas is extremely narrow. Also, essentially being similar to other printed integrated devices, their loss is high and thus their gain and the power handling capability are quite low.

Since the emergence of the first practical microstrip antennas, considerable effort has been put into the reduction of these intrinsic limitations. Numerous papers suggest different variations of the most basic rectangular and circular patch microstrip antennas, which have provided desirable and improved performances for various applications. Among these, the most common configurations are the annular ring [1], triangular patch [2], multiple-coupled lines as a rectangular patch [3] and microstrip antennas with different parasitic elements [4]. Other research attempts involve multilayer stacked microstrip antennas [5] and the so-called superstrate (cover) microstrip antennas [6]. Their analyses and properties will be reviewed in the next Chapter.

To continue in this endeavor, this dissertation proposes two new microstrip antennas based on the simplest geometry, the circular patch. The first one is the concentrically shorted circular patch microstrip antenna with superior electronic and geometric properties, while retaining the basic properties of conformability and ease of fabrication [7]. The other is the microstrip annular ring patch antenna shorted at the outer periphery with wide variable radiation characteristics [8]. In addition to the planar microstrip antennas, a new type of conformal microstrip antennas, i.e., biconical microstrip antenna, is also investigated. Biconical microstrip antennas may be installed at the tip of high speed vehicles, such as missiles, to satisfy the forward radiation requirement (radiation along the axis of the vehicle) and certain superior electronic performances.

1.2. The Statement of the Problem

The research is initially concentrated on one of the most basic and simple configurations, the circular patch antenna. Similar to other microstrip antennas, ordinary circular patch antennas are inherently resonant structures, and their dimensions are determined by the wavelength in the substrate and the order of their resonant modes. The antenna designer therefore has a limited flexibility to alter their input impedance and radiation characteristics. However, in practical applications, one desires to control and improve, to some degree, the gain or other performance parameters of the antenna. For single circular patch antennas, a convenient parameter to alter is the size of the patch. To retain the resonance frequency constant, one may incorporate a shorting rod, coaxially located at the patch center. For a given resonant frequency, increasing the rod radius increases the patch size and thus the gain. Since the size of the radiation ring at the antenna periphery increases, the pattern shape and the cross-polarization are also modified. The radius of the controlling rod thus can be effectively used to modify the radiation characteristics.

Based on the above consideration, the following modified circular patch microstrip antennas are proposed in this dissertation. They are the concentrically shorted circular patch microstrip antennas and the annular ring patch microstrip antenna shorted at the outer periphery.

The analysis of the concentrically shorted circular patch microstrip antennas is presented in Chapter 3.

The characteristics of the annular ring patch antennas shorted at the outer periphery and their comparison with the conventional annular ring data are provided in Chapter 4.

Chapter 5 deals with the biconical microstrip antenna. It is a completely new microstrip antenna which can be conformal to the tip of high speed vehicles . The early applications of microstrip antennas were long rectangular microstrip patches wrapped

around the cylindrical missile body [9]-[11]. However, for these structures, no radiation occurs at the forward direction, the movement direction of the vehicle (the axis of the cylinder). On the other hand, for tracking and aiming systems, the forward looking capability is a basic requirement, and the wraparound type of conformal microstrip antennas cannot be utilized for these applications. The thin and low profile antennas can be made conformal to the tip of high speed vehicles, which usually is conical in shape. They may take the shape of biconical structures and may radiate in the forward direction. They are no longer of a planar configuration and have not been studied previously.

This new type of conformal microstrip antenna is investigated in this dissertation. It consists of a conducting cone with a finite arm, the radiating element, electrically driven with respect to the grounded conducting cone, which is infinite in extent. A dielectric conical layer of infinite extent fills between the two cones. When the two cones have nearly the same apex angles, the antenna is of microstrip type, and is named here as the biconical microstrip antenna. A special case of biconical microstrip antennas is the conical patch microstrip antenna, that is, when the grounded cone becomes a plane (the angle of the grounded cone becomes 90^0), and the antenna geometry becomes a planar configuration again. The conical patch microstrip antennas offer certain superior performances in bandwidth and efficiency [12], and hence are excellent alternative for the circular patch antenna. Their analysis is also presented in Chapter 5.

The last chapter summarizes the whole dissertation and recommends further research work.

1.3. The Analytic Methods Used in This Dissertation

Numerous techniques have been proposed to analyze various microstrip antennas with differing degrees of accuracy and flexibility. They can be classified into two categories of the analytic modeling and numerical solutions.

The earliest mathematical model is the transmission-line model [13] which has recently been improved as the generalized transmission line model [14]. The merit of this model lies in its simplicity. The more useful and rigorous analytical modeling is the modal-expansion cavity model which considers the microstrip antennas as a thin cavity with a wall admittance at the periphery of the patch. The fields between the conducting patch and the ground plane are expanded in terms of resonant cavity modes, or eigenfunctions along with their eigenvalues (i.e., resonant frequencies associated with each mode) [15,16,17]. By means of this method, field solutions for regular or symmetric shape antennas with different feed types and locations are obtained much more accurately. Its usefulness, however, depends on finding appropriate orthogonal mode vectors.

Numerical techniques provide another powerful method, when considering arbitrary type microstrip antennas. The key to analyzing microstrip antennas with numerical methods lies in finding either the integral or differential equations from the physical or mathematical models. The suitability of the technique and the accuracy of their results depend on the available computational resources.

The geometries of the microstrip antennas proposed in this dissertation are symmetric and regular. The appropriate orthogonal mode vectors can therefore be determined readily to satisfy the boundary conditions. The mode-expansion cavity model is therefore adopted to analyze the problems in hand.

For the biconical microstrip antennas, the analysis begins by determining the eigenvalues of spherical wave functions, for the general biconical structures [18]. The fields between the cones are then expanded in terms of the available cavity modes, i.e.,

the *TE* modes. The coefficients of the series are determined by a mode matching method at the boundaries containing the feed and the radiating cone. The wall admittance (or impedance) at the aperture links the fields interior and exterior to the cavity. The study of the wall admittance or impedance was illustrated in [19].

Chapter 2
Literature Review

2.1. Definition of Microstrip Antennas

The idea of microstrip radiators was first proposed by Deschamps in the early 1950's [20] and is almost as old as the microstrip transmission lines. The intrinsic radiation loss of microstrips, which was considered as a harmful effect to be inhibited in printed circuit operation, was naturally taken advantage of by the antenna theoreticians to form a radiating element using the printed conductor. However, only two decades later, did the first practically viable design of microstrip antennas come into being. The appearance of practical microstrip antennas followed the development of improved theoretical models and photo-etching techniques. But, this increased utilization depended on progressive improvement and commercial availability of copper or gold-clad dielectric substrates with a wide range of dielectric constants, attractive thermal and mechanical properties and a low loss tangent. Nevertheless, since the emergence of first practical microstrip antennas in the early 1970's [9,10], extensive research and development have led to their diversified applications and to the establishment of microstrip antennas as a separate topic within the broad field of microwave antennas.

Many new types of microstrip antennas have evolved, which are variants of the basic sandwich structures, but the underlying concept is the same, that is, the printed radiating element is electrically driven with respect to a ground plane [21]. This definition admits a wide range of dielectric substrate thicknesses and permittivities, but to enhance the fringing fields which account for the radiation, the dielectric constant

should be low. The radiating element, which is a printed conductor of copper or gold, can assume virtually any shape or geometry [22,12].

2.2. Advantages and Fundamental Limitations

Compared with conventional microwave antennas, the advantages of microstrip antennas lie mainly in their geometry and ease of fabrication that enable miniaturizing and integrating with the electronic circuits. The frequency range suitable for them covers from 100 MHz to 50 GHz, including the mm-wave frequencies.

These geometrical and fabrication advantages are:

lightweight, low volume, low profile configuration which can be made conformal;

low fabrication cost, readily amenable to mass production;

thin shape that does not perturb the aerodynamics of host vehicles;

compatibility with modular design (solid state integrated devices);

feed line and matching network are fabricated simultaneously with the antenna.

Related to the geometrical properties, the advantages from the electrical point of view are their low scattering cross section and their suitability for linear and circular polarizations.

Microstrip antennas have fundamental limitations in the electronic properties when compared with traditional microwave antennas, such as reflector antennas. Since microstrip antennas are inherently resonant structures and electrically very thin (thus less resonant volumes), the bandwidth of microstrip antennas is extremely narrow. Also, essentially similar to the printed integrated devices, the loss in microstrip antennas is high and thus their gain and the power handling capability are quite low. Also, when they are used in mm-wave frequencies, mechanical tolerances are likely to be a

key factor, which leads to fabrication difficulties.

2.3. Applications

Microstrip antennas have been successfully used in various kinds of equipment from manpack microwave systems to very large phased arrays and involving diverse applications from medical instrumentation to military installations. With continuing research and development, the usage of microstrip antennas is still increasing. Some notable system applications for which microstrip antennas have been developed include [22]:

satellite communication,
doppler and other radars,
phased array radars,
manpack equipment,
feed element in complex antenna,
command and control,
missile telemetry,
biomedical radiator, and
satellite navigation receiver.

The list is by no means exhaustive. As the possibilities for microstrip antennas uses increase, the number of applications continues to grow.

2.4. Methods of Analyzing Microstrip Antennas

Since the emergence of the first practical microstrip antenna, considerable effort has been put into investigating the radiation mechanism and analyzing their general characteristics. Among many types of microstrip antennas, the rectangular and circular patch microstrip antennas have been suggested, which, in turn, have provided desirable and improved performances for various applications.

Many approaches exist to analyze microstrip antennas with differing degrees of accuracy and flexibility. These approaches can be classified into two categories: the analytic modeling and numerical solutions.

The earliest mathematical model is the transmission-line model [10,13], which uses the transmission line analogy to analyze rectangular patch microstrip antennas fed at the center of a radiating wall. The merit of this model lies in its simplicity, but it can only treat the rectangular shaped radiators. Recently, the generalized transmission line model [14] has extended the method to other microstrip patches where the separation of variables for the wave equation is possible.

Bhattacharyya proposed and used the generalized transmission line model to analyze the annular ring microstrip antennas. By taking the mutual coupling between the two radiating apertures into account, he has obtained more accurate expressions for the input impedance and bandwidth [23].

A more useful and rigorous analytical modeling is the model-expansion cavity model which considers the microstrip antennas as a thin cavity with a magnetic wall at its periphery. The fields between the conducting patch and the ground plane are expanded in terms of cavity resonant modes or eigenfunctions along with their eigenvalues or resonant frequencies [15,16,17]. The cavity modes are usually *TM* type, which are transverse magnetic fields and the TM_{11} is the dominant mode. By means of this method, field solutions for regular or symmetric shape antennas with different feed types and locations are more satisfactorily obtained. Recent improvements for

this modeling is the use of the admittance or impedance boundary condition at the wall, to take into account the effect of power radiation from the apertures, instead of assuming the magnetic wall at the periphery. The suitability of this modeling depends on finding appropriate orthogonal mode vectors.

The modal-expansion cavity model has been used to analyze microstrip antennas of various shapes, first the circular and rectangular patches, and then triangular, ellipse, disk sector, annular ring, and ring sector, etc [1,2,24,25,26].

Using the cavity model for the analysis, Bahl proposed a annular ring patch microstrip radiator for a medical application [1]. It is found that operating at the higher modes, such as TM_{12} mode, the antenna bandwidth increases to almost twice that of a circular patch antenna [22,23,26].

Krowne [11] used the modal-expansion cavity model to analyze the cylindrical-rectangular microstrip antenna, i.e., the wraparound conformal microstrip antenna, in the cylindrical coordinate system to estimate the effect of the curved surface. His results demonstrated that the assumption of conformally mounted microstrip antennas to be treated as a planar structure is satisfactory when h (thickness of the substrate) is small compared to the surface curvature, and is excellent when considering excitation of the antenna with no spatial field variation normal to the surface.

Related to the above cavity modal, the mode matching method is successfully used to determine the distributions along the modes [17]. By matching each mode at the boundaries, along the periphery containing the feed and the edges of the assumed cavity, the coefficients of the expansion series are obtained that include the effect of the feed location in the analysis.

Numerical techniques are powerful methods, when arbitrary type microstrip antennas are considered. The key to analyzing microstrip antennas by numerical methods lies in finding either the integral or differential equations which are obtainable from the physical and mathematical points of view. The suitability of the method and the accuracy of the results depend on the computational resources available.

The finite element method is a variational technique, coupled with the Raleigh-Ritz Method. Carver and Coeffey applied the finite element method to deal with the fields interior to a five-sided polygonal patch by solving the inhomogeneous wave equation along with an impedance boundary condition on the patch perimeter walls [16]. They produced reasonably accurate results but the method is computationally expensive.

The moment method, however, seems to be more straightforward and easy to handle mathematically as well as for numerical computation. Agrawal and Bailey [27] modeled the microstrip patch as a fine wire grid immersed in a dielectric medium and used the Richmond's reaction integral to evaluate the currents on the wire grid segments. They then modified the results to account for the dielectric slab by a frequency shift and an impedance scaling as obtained from experiment.

Newman and Tulyathan [28] also dealt with the use of moment methods in treating microstrip antennas. They demonstrated the use of interior surface currents in modeling an air-dielectric substrate microstrip patch. These unknown currents were determined by solving Richmond's reaction formula and the dielectric substrate was taken into account by using the volume equivalence theorem.

Bailey and Deshpande proposed a method to analyze the microstrip antenna by Galerkin's method [29]. They first derived the dyadic Green's function which satisfied the boundary conditions for a unit current located in the plane of the microstrip patch. Then, by using Galerkin's method, they solved the integro-differential equation for unknown patch current. This method avoids the reaction integral, but still calculates only the radiated electromagnetic fields inside the dielectric.

Pozar [30] presented a moment method solution of the impedance and mutual coupling of microstrip antennas using the same formulation as Newman [28], except that he utilized the rigorous grounded dielectric slab Green's function and that his results were more accurate than those of Newman.

A. Kishk and L. Shafai [31] applied the moment method to circular patch microstrip antennas to obtain the numerical solution of the radiation patterns including the effect of the finite circular ground plane. In their study, the integral equations were developed and applied to rotationally symmetric objects and then reduced to a matrix equation using the procedure commonly used to solve the problem of bodies of revolution. When the method was applied to the circular microstrip antenna, it provided a convenient approach to solve the contribution of various modes that are present in the structure and correspond to those of the modal expansion method. Their method allowed one to study the effect of each mode separately and to determine their excitation efficiency. The technique can also be used to study the annular ring microstrip patch or annular slot antennas on a finite circular ground plane, as well as covered microstrip antennas and stacked multiple band configurations.

Other techniques using the moment method have also been developed [32,33] that are only applicable to surface currents which are on the interior sides of both the patch and the associated ground plane. For an accurate study from radiation of microstrip antennas, however, a precise knowledge of the surface currents on both sides of the patch, and hence the near fields on the dielectric interface, are required. For this purpose, Lin and Shafai [34] presented a moment method technique, in which, applying the equivalence principle to the divided regions, the field distributions on both sides of the entire intersurface were properly determined. The method was general, in that the information on behavior of field distributions over and near the patch provides a rigorous study of microstrip antennas. It was therefore a useful numerical method for investigating arbitrary shape microstrip antennas. Its main disadvantage was in the large size of resulting matrix equation. This limited its usefulness only to small antennas.

The full wave analysis of microstrip antennas has been widely used in the past few years [35,36,37]. Sometimes, it is referred to as the spectral domain method.

T. Itoh and W. Menzel [35] modeled the microstrip structures as transmission lines with a short circuit at one terminal and a current source at an associated position on the line, which were analogous to the ground plane and current on the patch, respectively. Then by taking a integral transformation, the integral or the partial differential equations were converted to a set of algebraic equations suitably solved by a conventional moment method.

The spectral domain method is efficient in numerical computation and can give good approximate results. The realizability of the method lies in finding the basic and weighting functions which are both analytically transformable and converging fast enough mathematically, as well as being able to satisfy all boundary conditions in the physical sense.

This dissertation is an effort to continue the above research and development and to propose new types of microstrip antennas to enlarge the microstrip antenna family.

Also included in this dissertation is a detailed review of N. Das and J. S. Chatterjee's work "Conically depressed microstrip antennas" [12], and Jeddari, Mahdjoubi's "Broadband conical microstrip antenna" [38], the only papers in the literature that are related to the microstrip antenna investigated in the present study, i.e., the conical patch microstrip antennas.

In reference [12], the cavity between a slightly depressed cone and the ground plane is divided into two regions as shown in Fig.2.1. The antenna, which is assumed to be electrically thin, is fed by a TEM-line exciting a TM mode, as in the case of a circular patch antenna. In region R1, the fields are presumably the same as those of a circular patch antenna without the radial component of the electric field, as long as the height of region R1 is much larger than that of region R2. Along the slanting conducting surface, the tangential component of the electric field is zero, and hence the radial field E_r exists such that

$$E_z \cos\psi + E_r \sin\psi = 0$$

In region R2 (above the line A'B' in Fig.2.1b) of the resonant structure, therefore, the radial field E_r exists, having zero magnitude at $z = 0$ (along the line A'B') and $E_z \cos\psi$ at $z = r \cos\psi$ (along the conducting edge OB") as boundary conditions and varying uniformly in the z direction as the first approximation. The presence of E_r in region R2 induces H_z and hence E_ϕ which must exist, in addition to the existing fields E_z, H_r and H_ϕ, as extra internal fields.

In their analysis, this antenna is treated as a planar unit. The perturbational technique is successfully used to modify the cavity-mode expansion modeling for the fields in the slightly depressed region. It is found that the bandwidth of the antenna is twice that of a circular patch antenna, when the cone angle (ψ) equals 85^0 . This is a significant improvement for microstrip antennas. Also, the radiation efficiency is improved due to the enhancement of the fringing field at the radiating periphery by a slight depression of the circular patch conically into the substrate.

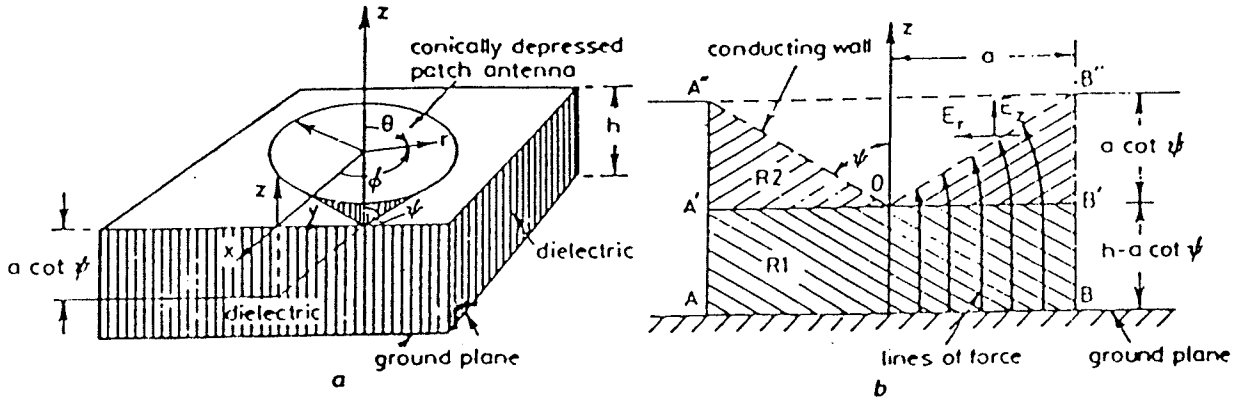

Fig.2.1 Conically depressed circular patch microstrip antenna

a . Conically depressed microstrip circular patch antenna

b . Vertically cut cross section of conically depressed patch antenna

In reference [38], by analogy to the circular patch antenna, Jeddari and Mahdjoubi chose a radial TE- mode and an effective spherical radius for the conical microstrip antenna. They found the TE_{11} mode resonance frequencies for different conical angles and dielectric constants. Although, their results are compared with the experimental data, their theoretical estimation seems too crude to be followed. The analogy to the circular patch antenna to determine the effective spherical radius lacks rigorous theoretical basis.

For the conical patch microstrip antenna, the special case of biconical microstrip antennas or deep depressed circular patch antennas (the height of region R1 is not much larger than that of region R2 as shown in Fig.2.1), the above technique is invalid and the structures are no longer planar. Therefore, the fields under the conical patch structures must be solved exactly in the spherical coordinate system and expanded in terms of spherical wave eigenfunctions as depicted in Chapter 5.

Chapter 3
Characteristics of Concentrically Shorted Circular Patch Microstrip Antennas

3.1. Introduction

Microstrip antennas are inherently resonant structures, and their dimensions are determined by the wavelength in the substrate and the order of its resonant modes. The antenna designer therefore has a limited flexibility to alter their input impedance and radiation characteristics. However, in practical applications, one desires to control, to some degree, the gain or other performance parameters of the antenna. For single patch antennas, a convenient parameter to alter is the size of the patch. To retain the resonant frequency constant, one may incorporate a shorting rod, coaxially located at the patch center. For a given resonant frequency increasing the rod radius increases the patch size and thus the gain. Since the size of the radiation ring at the antenna periphery increases, the pattern shape and the cross-polarization also modify. The radius of the controlling rod thus can effectively be used to modify the radiation characteristics.

In addition, the cylindrical conducting post with the patch itself provides an electromagnetic shield which can be used to house the required electronics to minimize the unit size.

The configuration of the antenna is shown in Fig.3.1. The antenna is modeled as a coaxial cavity bounded by a finite admittance wall at the periphery of the patch edge, the inner conducting cylinder and conducting plates on top and bottom. The admittance boundary condition is determined by the radiation power and the fringing field at

the patch edge. The effects of the dielectric substrate on the radiation patterns are accounted for by the Fresnel reflection coefficients of the two-layer stratified medium. The far field radiation patterns are determined by an approximate evaluation of various integrals using the steepest descent method.

The analytical results are compared with experimental data and available published results.

3.2. Mode Charts and Modal Field Expressions

The geometry of the antenna is shown in Fig.3.1, where the thickness, h, of the dielectric slab satisfies $h \ll \lambda$, i.e, $k_1 h \ll 1$, and $k_1 = \omega\sqrt{\mu\varepsilon_1}$, ω being the angular frequency. The field distribution under the patch thus does not vary in the z direction. The electromagnetic field excitation is due to a current I_0 along the z direction and through the center conductor of a coaxial cable at $r = d$. The current source can therefore be expressed as

$$\mathbf{J} = \hat{k}\, I_0 \frac{\delta(r - d)}{r}\, \delta(\phi) \tag{3.1}$$

Because of the uniformity of the current on the feed probe along the z direction, only the *TM* modes can be excited within the cavity. None of the *TE* modes can be excited since they vary along the z direction [39]. The field distribution of the *TM* modes can be represented by the following equations [17],

$$E_z = \sum_{n=0}^{\infty} f_n(k_1 r) \cos n\phi \tag{3.2}$$

$$H_r = \frac{-j}{\omega\mu r} \sum_{n=0}^{\infty} n\, f_n(k_1 r) \sin n\phi \tag{3.3}$$

$$H_\phi = \frac{-jk}{\omega\mu} \sum_{n=0}^{\infty} f'_n(k_1 r) \cos n\phi \tag{3.4}$$

where

$$f_n = f_{n1} = A_n J_n(k_1 r) + B_n Y_n(k_1 r) \qquad a < r < d$$

$$f_n = f_{n2} = C_n J_n(k_1 r) + D_n Y_n(k_1 r) \qquad d < r < b \tag{3.5}$$

J_n and Y_n are Bessel functions of the first and second kinds, and the prime denotes the derivatives with respect to the argument, subscripts 1 and 2 represent the two regions separated by the cylinder $r = d$. A_n , B_n , C_n and D_n are constants to be determined.

The ϕ and r components of the electric field do not exist due to the assumed uniform field distribution along the z direction. The time factor $e^{j\omega t}$ is assumed and suppressed throughout the analysis.

The following boundary conditions are imposed

$$E_z = 0 \qquad (at \quad r = a) \tag{3.6}$$

$$H_{\phi n} = -y_{sn} E_{zn} \qquad (at \quad r = b) \tag{3.7}$$

$$E_{z1} = E_{z2} \quad or \quad H_{r1} = H_{r2} \qquad (at \quad r = d) \tag{3.8}$$

$$H_{\phi 1} - H_{\phi 2} = \frac{I_0 \delta(\phi)}{d} \qquad (at \quad r = d) \tag{3.9}$$

where $y_{sn}=g_{sn}+jb_{sn}$ is the wall admittance. There is an additional boundary condition at the periphery of the assumed cavity with a magnetic wall at $r=b_e$

$$H_\phi = 0 \qquad (at \quad r = b_e) \tag{3.10}$$

For a cavity with a magnetic wall at $r = b_e$, an electric wall at $r=a$, a conducting top patch and a lower ground plane, the characteristic equation can be derived from eqns 3.6 and 3.10 and is given by

$$J_n(k_1 a)\, Y'_n(k_1 b_e) = Y_n(k_1 a)\, J'_n(k_1 b_e) \tag{3.11}$$

The resonant mode chart of these antennas can be obtained from eqn. 3.11 and the coefficients in eqn.3.5 can be determined by solving eqns 3.6 to 3.9. The results are

$$A_n = -\frac{j\omega\mu I_0}{2\,(1+\delta_n)} \frac{Y_n(k_1 a)\,[z_{n2}\,Y_n(k_1 d) - z_{n1} J_n(k_1 d)]}{I_n} \tag{3.12}$$

$$B_n = \frac{j\omega\mu I_0}{2\,(1+\delta_n)} \frac{J_n(k_1 a)\,[z_{n2}\,Y_n(k_1 d) - z_{n1} J_n(k_1 d)]}{I_n} \tag{3.13}$$

$$C_n = -\frac{j\omega\mu I_0}{2\,(1+\delta_n)} \frac{z_{n1}\,O_n}{I_n} \tag{3.14}$$

$$D_n = \frac{j\omega\mu I_0}{2\,(1+\delta_n)} \frac{z_{n2}\,O_n}{I_n} \tag{3.15}$$

where δ_n=1 for $n = 0$, δ_n=0 for $n > 0$, and

$$z_{n1} = Y'_n(k_1 b) + j\, y_{sn} Z_1\, Y_n(k_1 b) \tag{3.16}$$

$$z_{n2} = J'_n(k_1 b) + j\, y_{sn} Z_1\, J_n(k_1 b) \tag{3.17}$$

$$I_n = z_{n1}\, J_n(k_1 a) - z_{n2}\, Y_n(k_1 a) \tag{3.18}$$

$$O_n = Y_n(k_1 d)\, J_n(k_1 a) - J_n(k_1 d)\, Y_n(k_1 a) \tag{3.19}$$

and

$$Z_1 = \sqrt{\mu_1/\varepsilon_1}$$

In the above derivation, the Wronskian of the Bessel functions was used.

In eqns 3.12 to 3.19 the wall admittance should be determined. The wall conductance can be calculated from the radiation power leaving the side wall [17] in the form

$$g_{sn} = \frac{P_{rad}}{\frac{1}{2}\int_s |\, E_z \,|^2 d\, s} \tag{3.20}$$

The wall susceptance can be found from the energy stored in the volume between the patch edge at b and the cavity wall at b_e . It leads to the following first order asymptotic expression,

$$b_{sn} = \frac{F'_n(\zeta)}{Z_1\, F_n(\zeta)} \tag{3.21}$$

where

$$\zeta = \chi_b / (1 + \Delta)^{1/2} \quad , \tag{3.22}$$

and χ_b is the root of eqn.(3.11) and

$$F_n(\zeta) = J_n(k_1 a) Y_n(\zeta) - Y_n(k_1 a) J_n(\zeta) \tag{3.23}$$

The parameter Δ in eqn.3.22, to account for the effect of the fringing field, is normally calculated using the following equation[17]:

$$\Delta = \frac{2\ h\ \varepsilon_0}{b \varepsilon_1} [\ln(\frac{\pi b}{2\ h}) + 1.7726] \tag{3.24}$$

which is derived from the quasi-static capacitance of the microstrip circular disk with a relative permittivity of unity and a very thin substrate. However, due to the existence of the shorted rod at the center, it must be modified. That is, one needs to compute the mode capacitances of coaxially shorted circular cavity. This can be done using the Green's function method [25,40], where the zero order capacitance is given by

$$C_{00} = \frac{\pi \varepsilon (b^2 - a^2)}{h} \tag{3.25}$$

For this reason, one can assume an equivalent circular patch radius b_c to give the same capacitance as that given by 3.25. It leads to

$$b_c = \sqrt{b^2 - a^2} \tag{3.26}$$

Thus, the parameter Δ can be calculated using eqn.3.24 by replacing b with b_c . The approximate wall susceptance can now be obtained from eqns 3.21 to 3.23.

The cavity will then resonate when

$$k_1 b \ (1 + \Delta)^{1/2} = \chi_b \tag{3.27}$$

The expressions for fields inside the cavity will be used in the following sections to determine the near and far field characteristics such as the input impedance, radiation pattern, directivity and bandwidth.

3.3. Input Impedance and Bandwidth

The input impedance is calculated from an equivalent parallel resonant network as shown in Fig.3.2, which is the network model over a narrowband for the isolated TM_{11} mode. The resistive and reactive parts are determined by the radiation power, dielectric and conductor losses and stored energies [41]. It is given by

$$Z_{in} = \frac{\frac{1}{2}VV^*}{P_t + 2j\,\omega(W_e - W_m)} \tag{3.28}$$

where V is the voltage crossing the patch and ground plane at $r = d$ and $\phi=\phi_0$ calculated from

$$V = \int_0^d E_z \, dz \quad , \tag{3.29}$$

W_e and W_m are the stored electric and magnetic energies per cycle, given by

$$W_e = \frac{\varepsilon}{4}\int_v \mathbf{E}\cdot\mathbf{E}^* \, dv \quad , \tag{3.30}$$

$$W_m = \frac{\mu}{4}\int_v \mathbf{H}\cdot\mathbf{H}^* \, dv \quad , \tag{3.31}$$

P_t is the total lost power as

$$P_t = P_{rad} + P_d + P_l \tag{3.32}$$

where P_{rad}, P_d and P_l are the radiation power, the dielectric and conductor losses and given by

$$P_d = 2\,\omega\, W_e \tan\delta \tag{3.33}$$

$$P_l = \frac{2\,\omega\, r_s}{h} W_m \tag{3.34}$$

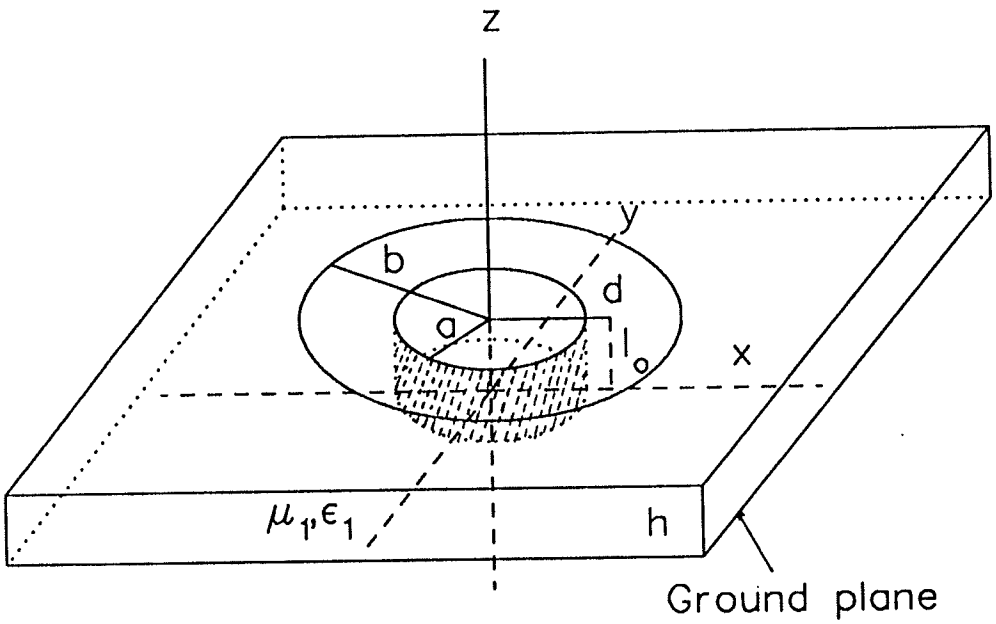

Fig.3.1: Microstrip circular patch with a central short

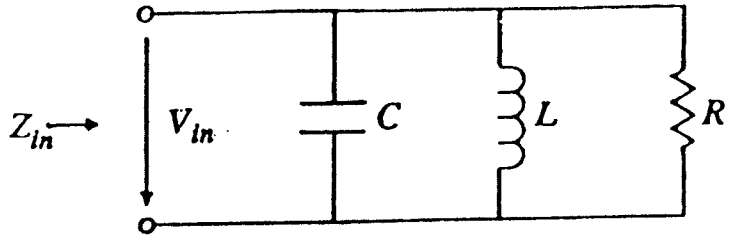

Fig.3.2: Network model over a narrowband for an isolated mode

where tan δ is the loss tangent of the dielectric and $r_s = (\pi\mu\sigma f)^{1/2}$.

The bandwidth is determined in terms of the Q factor and maximum allowable VSWR and is defined as [41]

$$BW = \frac{VSWR-1}{Q\sqrt{VSWR}} \tag{3.35}$$

where

$$Q = \frac{2\,\omega\,W_e}{P_t} \tag{3.36}$$

3.4. Radiation Fields

The far fields are calculated from the vector magnetic and electric potentials

$$\mathbf{A}(r) = \frac{\mu}{4\pi}\frac{e^{-jk_0 r}}{r}\int_s \mathbf{K}(r)e^{jk_0|\mathbf{r}-\mathbf{r}'|}\,d\,s' \tag{3.37}$$

and

$$\mathbf{F}(r) = \frac{1}{4\pi}\frac{e^{-jk_0 r}}{r}\int_s \mathbf{M}(r)e^{jk_0|\mathbf{r}-\mathbf{r}'|}\,d\,s' \tag{3.38}$$

where $\mathbf{K}(r)$ and $\mathbf{M}(r)$ are the surface electric and magnetic currents on the radiation aperture surrounding the conducting patch, S is the aperture ring with a width h, and for the distant region

$$|\mathbf{r}-\mathbf{r}'| = r'\sin\theta\cos(\phi-\phi') \tag{3.39}$$

The electric and magnetic currents are given by

$$\mathbf{K} = \hat{n}'\times H_\phi\hat{\phi}' \tag{3.40}$$

and

$$\mathbf{M} = \hat{h}' \times E_z \hat{z}' \tag{3.41}$$

where H_ϕ and E_z are the tangential components of the magnetic and electric fields on the radiation aperture at $r = b$ and $\hat{h}'$ is the unit vector normal to the aperture surface.

The electric fields in the far zone can be obtained from

$$E_\theta = -j\ \omega A_\theta - j\ k_0 F_\phi \tag{3.42}$$

$$E_\phi = -j\ k_0 F_\phi \tag{3.43}$$

Therefore, they can be written as

$$E_\theta = -\frac{1}{4\pi}\ [\ 1 - R^{TM}\ ] \int_0^h dz' \int_0^{2\pi} b d\phi'\ [j\omega\mu\ H_\phi \cos(\phi - \phi') - jk_0 E_z \sin\theta]\ e^{jk_0 b \sin\theta\ \cos(\phi - \phi')} \tag{3.44}$$

$$E_\phi = -\frac{jk_0}{4\pi}\ [\ 1 + R^{TE}\ ] \int_0^h dz' \int_0^{2\pi} b d\phi'\ [\ E_z\ \sin(\phi - \phi')] e^{jk_0 b\ \sin\theta\ \cos(\phi - \phi')} \tag{3.45}$$

After some integral manipulations, the far fields of a TM_{nm} mode are obtained as

$$E_{\theta n} = \frac{j^{n+1}}{2}\ h\ \cos n\phi\ \ [k_0 b\ f_{n2}(k_1 b)\ J'_n(k_0 b \sin\theta) + j\ k_1 b\ \sin\theta\ f'_{n2}(k_1 b)\ J_n(k_0 b \sin\theta)] \tag{3.46}$$

and

$$E_{\phi n} = \frac{j^{n+1}}{2} k_o n\ h\ \frac{\sin n\phi}{k_0 \sin\theta}\ f_{n2}(k_1 b)\ J_n(k_0 b \sin\theta)\ (1 + R^{TE}) \tag{3.47}$$

Note that the distance term $\frac{e^{-jk_0 r}}{r}$ is omitted from eqns 3.44 to 3.47.

One can see that the last term in the square brackets of eqn. 3.46 represent the contribution of the electric currents on the admittance wall. As the inner radius a increases, the contribution of the electric current on the admittance wall increases. It also increases the patch size and results in the appearance of a sidelobe, which affects both gain and bandwidth of the antenna.

The effect of the grounded dielectric substrate are taken into account by the factor $1-R^{TM}$ for E_θ and $1+R^{TE}$ for E_ϕ , where R represents the Fresnel reflect coefficients of a two-layer stratified medium [39].

For determining factors $1-R^{TM}$ and $1+R^{TE}$, the identity

$$\frac{e^{-jk_0r}}{r} = \frac{1}{2j}\int_{-\infty}^{\infty}\frac{k_r}{k_z}H_0^{(2)}(k_r r)\, e^{\pm jk_z z}\, dk_r \tag{3.48}$$

is used in eqn.3.37, where $H_0^{(2)}$ is the second kind of Hankel function and $k_z=(k_0^2-k_r^2)^{1/2}$.

In the far zone, i.e., when $|\mathbf{r}-\mathbf{r}'|\to\infty$ and $z\to\infty$, the current sheet in eqn.3.37

$$\mathbf{J}(r) = \mathbf{K}(x,y)\,\delta(z)$$

can be considered as a point source in the presence of the stratified medium. Thus, integrals of the form

$$I_1 = \int_{-\infty}^{\infty}\frac{k_r}{k_z}(1-R^{TM})\, e^{jk_z z}\, H_0^{(2)}(k_r\,|\mathbf{r}-\mathbf{r}'|)\, dk_r \tag{3.49}$$

$$I_2 = \int_{-\infty}^{\infty}\frac{k_r}{k_z}(1+R^{TM})\, e^{jk_z z}\, H_0^{(2)}(k_r\,|\mathbf{r}-\mathbf{r}'|)\, dk_r \tag{3.50}$$

are involved in the calculation of A_θ and A_ϕ, where [38]

$$1-R^{TM} = \frac{2\sin k_{1z}h}{\sin k_{1z}h + j\varepsilon_r\dfrac{k_z}{k_{1z}}\cos k_{1z}h} \tag{3.51}$$

and

$$1+R^{TE} = \frac{2\sin k_{1z}h}{\sin k_{1z}h + j\dfrac{k_{1z}}{k_z}\cos k_{1z}h} \tag{3.52}$$

where

$$k_{1z} = (k_1^2 - k_{1r}^2)^{1/2} \tag{3.53}$$

Using the steepest descent method to calculate I_1 and I_2, one can show that the dominant contribution to I_1 and I_2 comes from the stationary point at

$$k_{rs} = k_0 \sin\theta \tag{3.54}$$

and

$$I_1 \approx \frac{2}{j}[1 - R_{TM}]\frac{e^{j\mathbf{k}_0\cdot\mathbf{r} - j\mathbf{k}_0\cdot\mathbf{r}'}}{|\mathbf{r}-\mathbf{r}'|} \tag{3.55}$$

$$I_2 \approx \frac{2}{j}[1 + R_{TE}]\frac{e^{j\mathbf{k}_0\cdot\mathbf{r} - j\mathbf{k}_0\cdot\mathbf{r}'}}{|\mathbf{r}-\mathbf{r}'|} \tag{3.56}$$

These approximate results for I_1 and I_2 have already been used to obtain eqns. 3.42 and 3.43. The locations of the singularities, the stationary point and the steepest descent path passing it are shown in Fig.3.3 [42].

Substituting k_{1r} by k_{rs} in eqn. 3.51, one can obtain

$$1 - R^{TM} = \frac{2\sin[(k_1^2 - k_0^2\sin^2\theta)^{1/2}h]}{\sin[(k_1^2 - k_0^2\sin^2\theta)^{1/2}h] + j\dfrac{\varepsilon_r\cos\theta}{(\varepsilon_r - \sin^2\theta)^{1/2}}\cos[(k_1^2 - k_0^2\sin^2\theta)^{1/2}h]} \tag{3.57}$$

$$1 + R^{TE} = \frac{2\sin[(k_1^2 - k_0^2\sin^2\theta)^{1/2}h]}{\sin[(k_1^2 - k_0^2\sin^2\theta)^{1/2}h] + j\dfrac{(\varepsilon_r - \sin^2\theta)^{1/2}}{\cos\theta}\cos[(k_1^2 - k_0^2\sin^2\theta)^{1/2}h]} \tag{3.58}$$

In deriving eqns 3.55 and 3.56, the path of integration is deformed such that the contributions to the surface and leaky waves due to the poles of the integrand [43] are omitted. This approximation causes the fields at $\theta = \pi/2$, in eqns 3.51 and 3.52, to become zero. However, only the first surface wave mode may be excited for $k_1 h \ll \lambda$, and in most radiation directions, except for the horizontal direction ($\theta = \pi/2$), its contribution is negligible compared with that of the space wave.

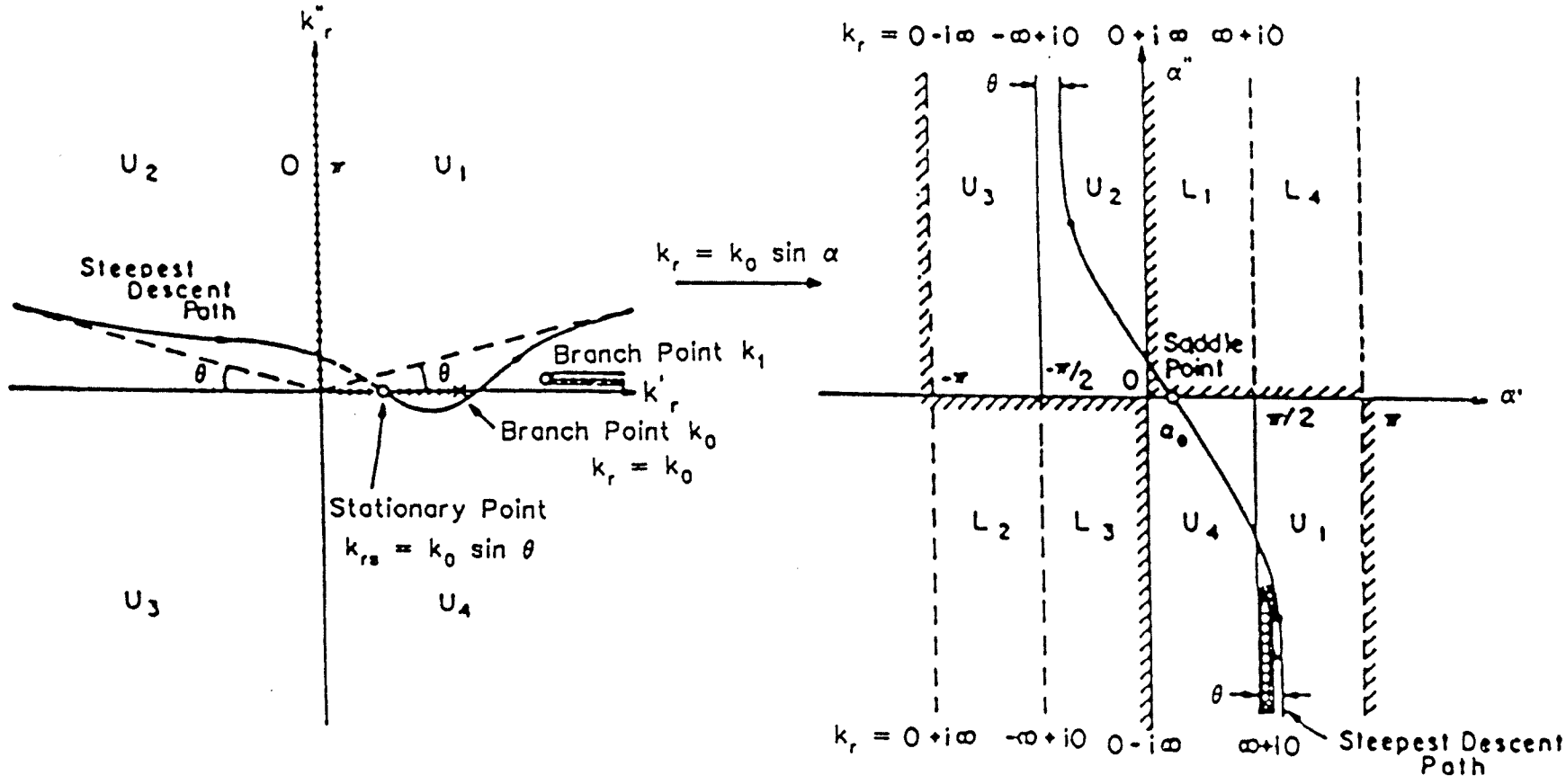

(a) (b)

Fig.3.3: Mapping of the complex k_r plane to the complex α plane by the transformation $k_r = k_0 \sin\alpha$. (a). k_r plane. (b). α plane

3.5. Results and Discussion

At resonance of TM_{11} to TM_{61} modes the dependence of the outer radius b on the inner radius a are shown in Fig.3.4. For the TM_{11} mode the relationship is almost linear and the effect of the rod radius is negligible only when $a \ll \lambda$ and $a \ll b$. But, as the mode number increases, the effect of a on b becomes less significant. That is, only for large values of a , the outer radius b increases with a. This means that for the dominant TM_{11} mode the parameter a can be used effectively to alter the antenna size and thus its radiation pattern and gain.

Figs 3.5 and 3.6 show the comparison of the experimental and calculated input impedances of the TM_{11} and TM_{21} modes, where the gauss-jacobi quadrature formula is used to calculate the integral in eqns. 3.30 and 3.31. The antenna dimensions are b=1.6335cm and a=0.6255cm; and the relative permittivity and the thickness of the substrate are 2.52 and 1.6 mm, respectively. The dielectric loss tangent of the substrate is 2×10^{-3} and the conductivity of the patch, the inner conducting wall and the ground plane is assumed to be $5.8\times10^{7} mho/m$. The feed position d is 0.85 cm from the patch center.

The calculated resonant frequencies of the TM_{11} and TM_{21} modes are 4.0412158 and 5.663978 GHz, respectively, and the measured ones are 4.0275 and 5.6702 GHz, respectively. Their differences are less than 1% and computed and measured input resistances show good agreement in Figs 3.5 and 3.6. Letting a approach 0, the calculated input impedance, resonant frequency and radiation patterns agree well with the results in [17] and [39].

The calculated input impedance with the effect of the coaxial feed is also shown in Fig.3.5, where the diameter of the feed probe, the central conductor of the standard connector is 1.2 mm. The method proposed by Lier [44] is used and it was found that the effect is of capacitive type for selected substrate thickness and frequency range. The total feed reactance is almost constant in magnitude, around 12Ω for the indicated

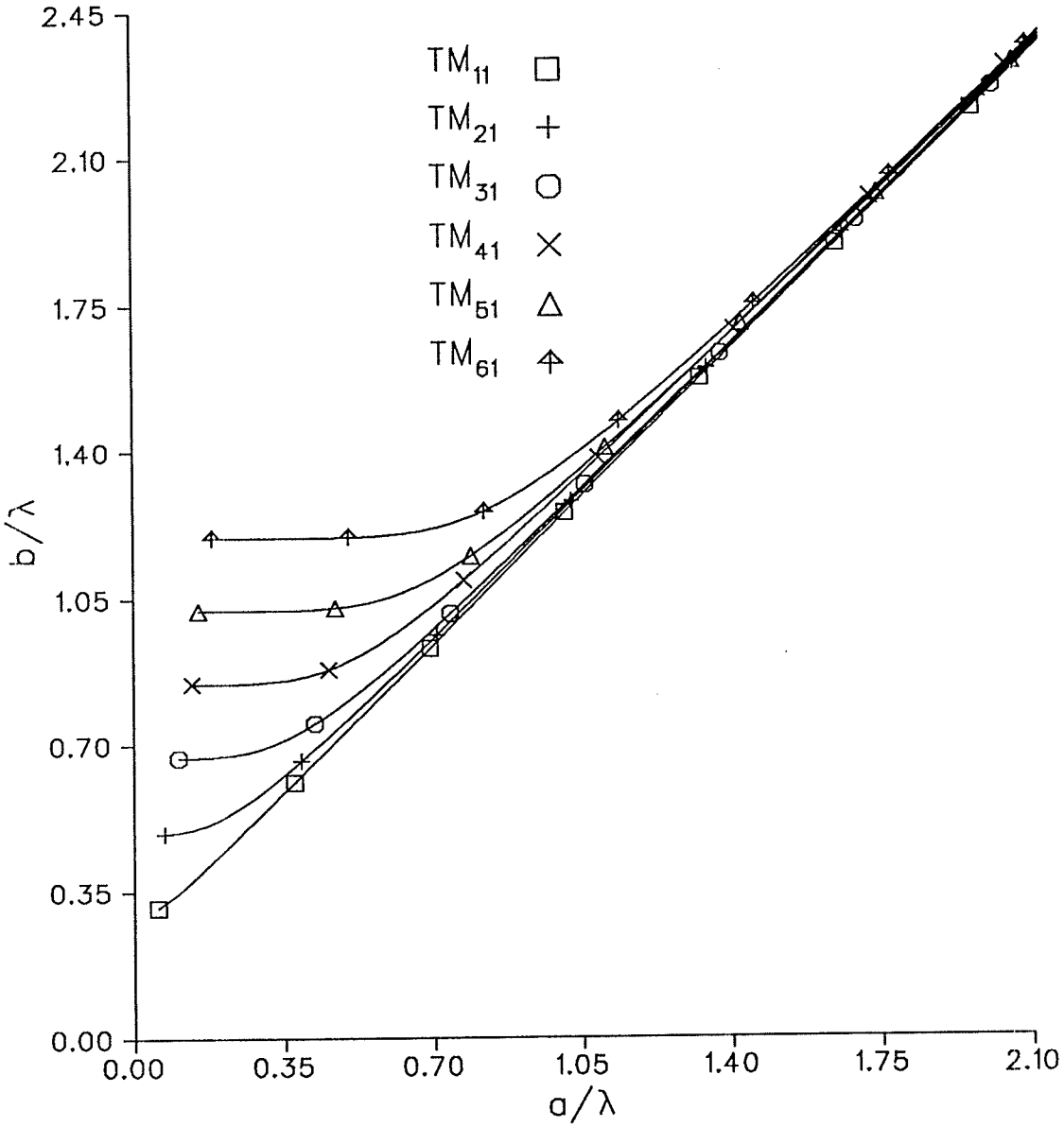

Fig.3.4: Mode chart, Relationship between the patch radius b and the radius, a, of the central short at resonance of TM_{n1} modes

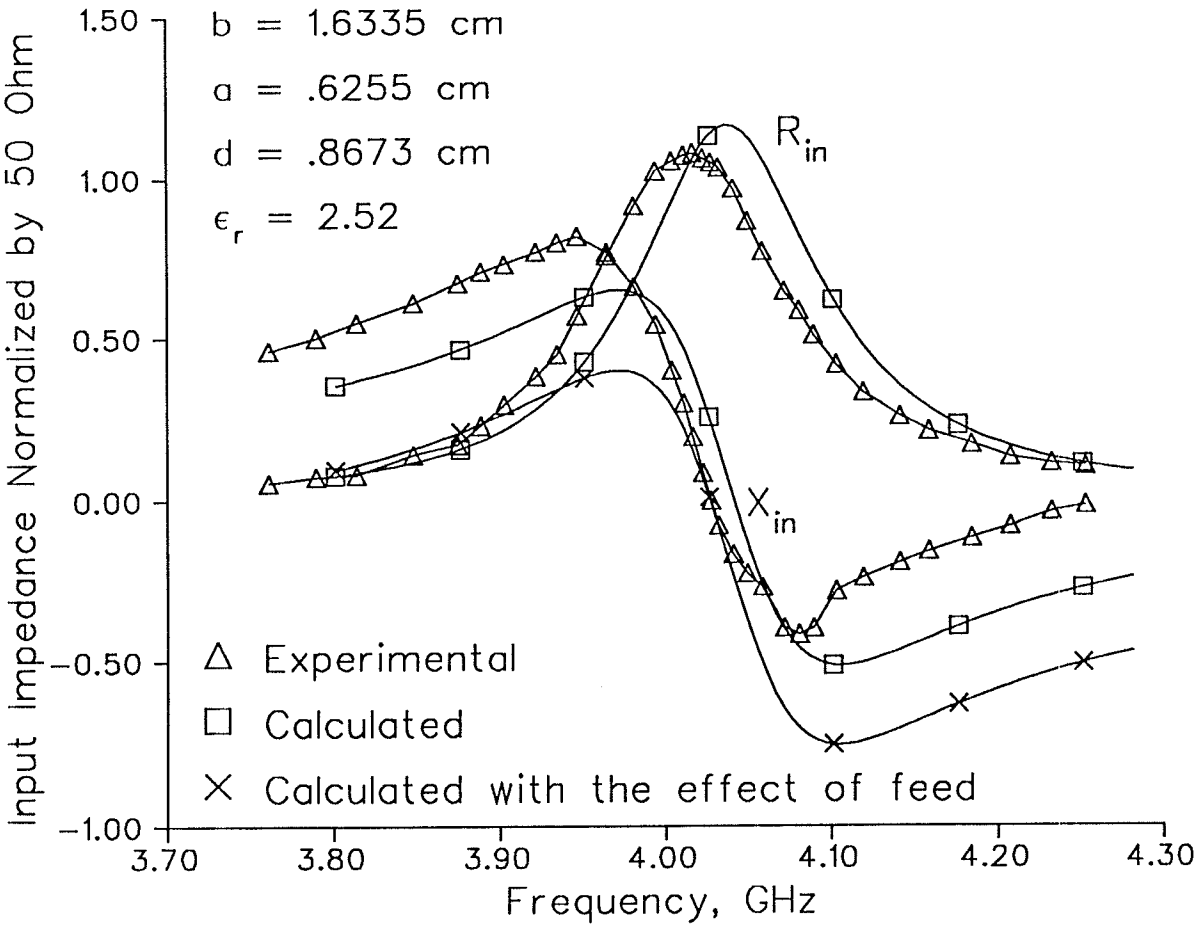

Fig.3.5: Input impedance of the TM_{11} mode for a circular patch with a central short

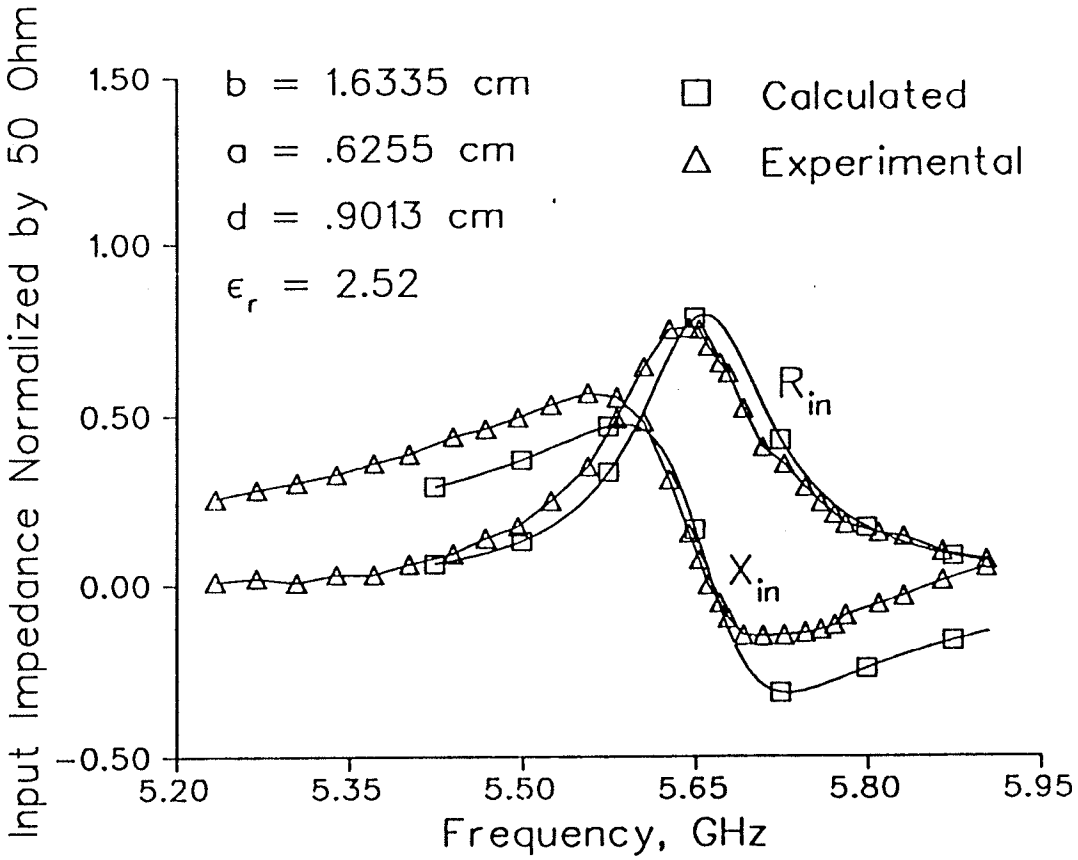

Fig.3.6: Input impedance of the TM_{21} mode for a circular patch with a central short

frequency range. The computed resonant frequency with the reactance of the feed improves

from 4.0412158 to 4.0274735 GHz, which is closer to the measured value.

Table 3.1 illustrates the comparison of the measured and calculated resonant frequencies, the input resistances at resonance, the gain and the bandwidth of the TM_{11} mode, when the inner radius a is large. Again, the difference in the resonant frequences is less than 1%. The good agreement for both large and small values of a substantiates the validity of expressions 3.25 and 3.26. These, together with eqn 3.24, indicate good approximation for the effective radius b_e and the wall susceptance b_{sn}. The calculated gain were also verified by the measurement. However, the bandwidth and the input resistance at resonance show differences of as much as 5%, when the effect of the probe is omitted. After this effect is taken into account, the calculated data are improved.

	f_r (GHz)	$R_{in}(\Omega)$	$Gain(dB)$	$BW(\%)$
measured	4.1945	55.32	10.1	2.036
calculated$^{(a)}$	4.2092	57.812	9.986	2.141
calculated$^{(b)}$	4.1953	54.241	9.978	2.112

Table 3.1. Comparison of the measured and calculated data for the circular patch with a central short ($b = 2.85\ cm$, $a = 1.91\ cm$, $h = 1.6\ mm$ and $\varepsilon_r = 2.52$), (a) without feed probe, (b) with feed probe.

Fig.3.7 shows the computed radiation characteristics of the TM_{11}, in which the cross-polarizations are calculated in the ϕ=45^0 plane, which are maximum according to the third definition of Ludwig [45]. In Figs 3.7a and 3.7b, the outer radius is kept constant at 1.6335 cm and the antenna is fed at the edge while increasing the inner radius a. One can see that both the pattern beamwidth and the peak cross-polarization decrease. That is, the shorted rod can significantly improve the far fields properties of circular patch antennas. In Figs 3.7c and 3.8d, three different pairs of b and a are selected to keep the resonant frequency at 3.7428 GHz and the antennas are excited by

a probe at the edge of the patch. Again, the directivities and cross polarizations improve when the ratio of b/a decreases. This means that, for a given resonant frequency, the rod radius increases, and so do the patch size and gain, but the cross-polarization decreases. The same phenomenon is observed in Table 3.2. Keeping the resonant frequency constant at 3.7428 GHz, the directivity increases initially as a increases until the side lobe is formed (shown in Fig.3.7c). As the side lobe level increases (a becomes large), the directivity is maintained around 10 dB level (note: the gain of ordinary circular patch antenna is about 7 dB) and then tends to drop slowly. Similar results are also observed for the bandwidth and radiation efficiency. As a increases, the input resistance at resonance decreases to around 50 Ω. This property leads to the direct matching of the antenna and feed probe at the edge of the patch, which is not the case for ordinary circular patch antennas.

b/a	a (cm)	b (cm)	$R_{in}(\Omega)$	$D(dB)$	$BW(\%)$	$effi.(\%)$
38.88	0.0383	1.4127	345.533	7.0028	0.7509	95.764
3.363	0.4856	1.6332	100.097	9.4328	1.2634	96.366
2.102	0.9918	2.0853	73.721	12.481	0.8222	95.653
1.761	1.4162	2.4945	63.553	12.2706	0.9912	96.265
1.584	1.8336	2.9039	59.225	10.6945	1.5679	97.413
1.506	2.1087	3.1752	57.610	10.2273	1.8686	97.743

Table 3.2. Ratio of b/a, radii, a and b, input resistance, directivity, bandwidth and efficiency of a circular patch with a central short at the resonant frequency of 3.7428 GHz for the TM_{11} mode with $d = b$, $\varepsilon_r = 2.52$ and h=1.585 mm

As shown in Fig.3.8, the direction of maximum radiation for the TM_{21} mode is no longer at $\theta = 0$ and shifts towards the horizon as a decreases. The outer radius is kept at 1.6335 cm and the feed is at the antenna edge. The radiation properties of high order modes for the proposed antenna are similar to those of conventional disk antennas.

Figs 3.9a and 3.9b show the bandwidth and radiation efficiency of the TM_{11} mode v.s. the substrate thickness ($\varepsilon_r = 2.52$) and dielectric permittivity (h = 1.6 mm

), respectively, where $b = 2.85$ cm and $a = 1.9$ cm and $d = b$. The bandwidth increases linearly, as the thickness of the substrate increases. It decreases rapidly as the relative permittivity increases. Also, the antenna radiation efficiency increases slowly as the thickness increases and drops by about 20 % as the relative permittivity increases from 1 to 10.

The calculated input resistance and resonant frequency v.s. the feed position d are shown in Fig.3.10 for the TM_{11} and TM_{21} modes. For both modes, as the feed moves from the inner short to the edge of the patch, the input resistance at resonance increases rapidly. On the other hand, the resonance frequency remains relatively constant. This is similar to the ordinary circular patch antennas.

More interesting results are shown in Figs 3.11 and 3.12, which illustrate the relationships between the shorting rod radius a and the resonance frequency, the input resistance at the resonance, the directivity and the bandwidth for the TM_{11} and TM_{21} modes, respectively, for b=1.6335cm. The antenna is fed at the edge of the patch. As shown in Fig.11a, both the directivity and the bandwidth of the TM_{11} mode increase steadily for a/b larger than 0.15. But, for the TM_{21} mode, as shown in Fig.3.12a, the directivity and the bandwidth increase significantly, only when a/b is larger than 0.3. In Fig.3.11a, the maximum radiation direction shifts from the ϕ=0^0 plane to the ϕ=45^0 plane, around $a/b = 0.57$. These phenomena are due to the fact that, as a increases, the patch size increases and results in the appearance of the sidelobe, and leads to the directivity going down as b/a is larger than 0.65. This means that for the dominant TM_{11} mode the parameter a can be effectively used to alter the antenna size and thus its radiation pattern, gain, bandwidth and radiation efficiency.

As shown in Figs 3.11b and 3.12b, for both TM_{11} and TM_{21} modes, as the inner radius a increases, the resonance frequency increases rapidly. The input resistance remains high and almost constant as a/b is less than about 0.4 , and then decreases rapidly as a/b becomes greater than 0.45. A very notable phenomenon illustrated in Fig.11b is that the input resistance becomes 50 Ω at a/b around 0.692 for the feed

point at the edge. This means that, by choosing a/b=0.692 one can directly use the 50 Ω microstrip transmission line to feed the antenna without the need for a matching circuit. Again, a main difference from an ordinary circular patch antenna.

The above calculated and experimental data show that the proposed antenna can have higher gain, wider bandwidth and a better impedance behavior than the conventional circular patch antenna. Its flexible electrical properties, controllable easily by a modification of the central short size, can be used readily in designing more useful antennas for different applications. In particular, the possibility of achieving a 50 Ω or other reasonable impedance level at the patch edge simplifies the feed design. This will be a useful and desirable property in array applications to integrate the antenna with its feed network.

3.6. Conclusion

The characteristics of coaxially shorted microstrip circular patch antennas were presented. The antenna was modeled as a coaxial cavity to determine its field distributions inside the cavity. The near-field and far-field properties were studied and compared with experimental data. The comparison substantiated the analytic results. The results also showed that the proposed radiation element is a useful antenna with high gain and improved bandwidth. Its geometry and flexible characteristics gave the antenna designer adequate parameters to control its electrical performance parameter to meet different design specifications.

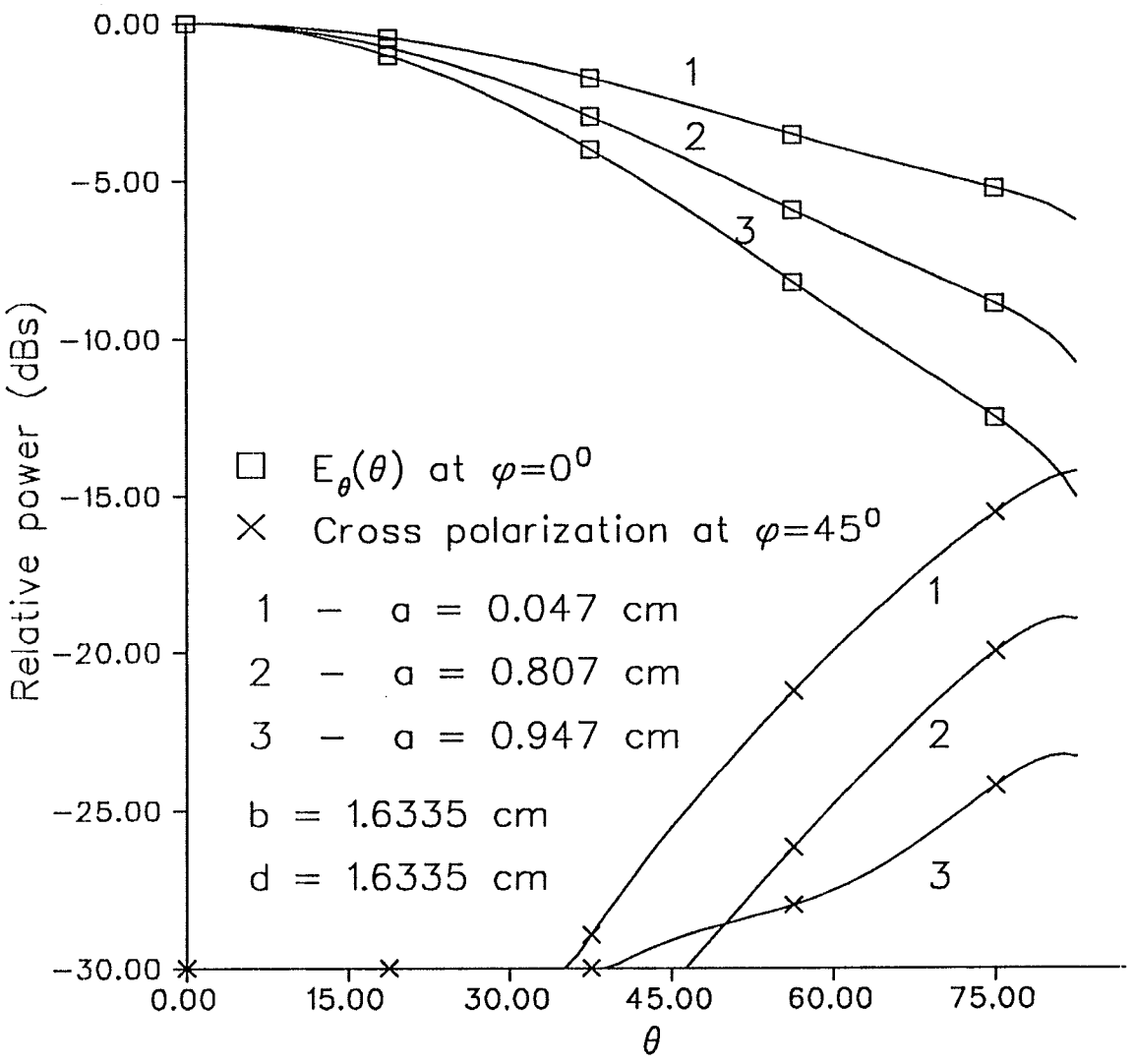

Fig.3.7a: Computed E_θ patterns for a circular patch with central shorts at resonance of the TM_{11} mode, where the outer radius, b, is constant.

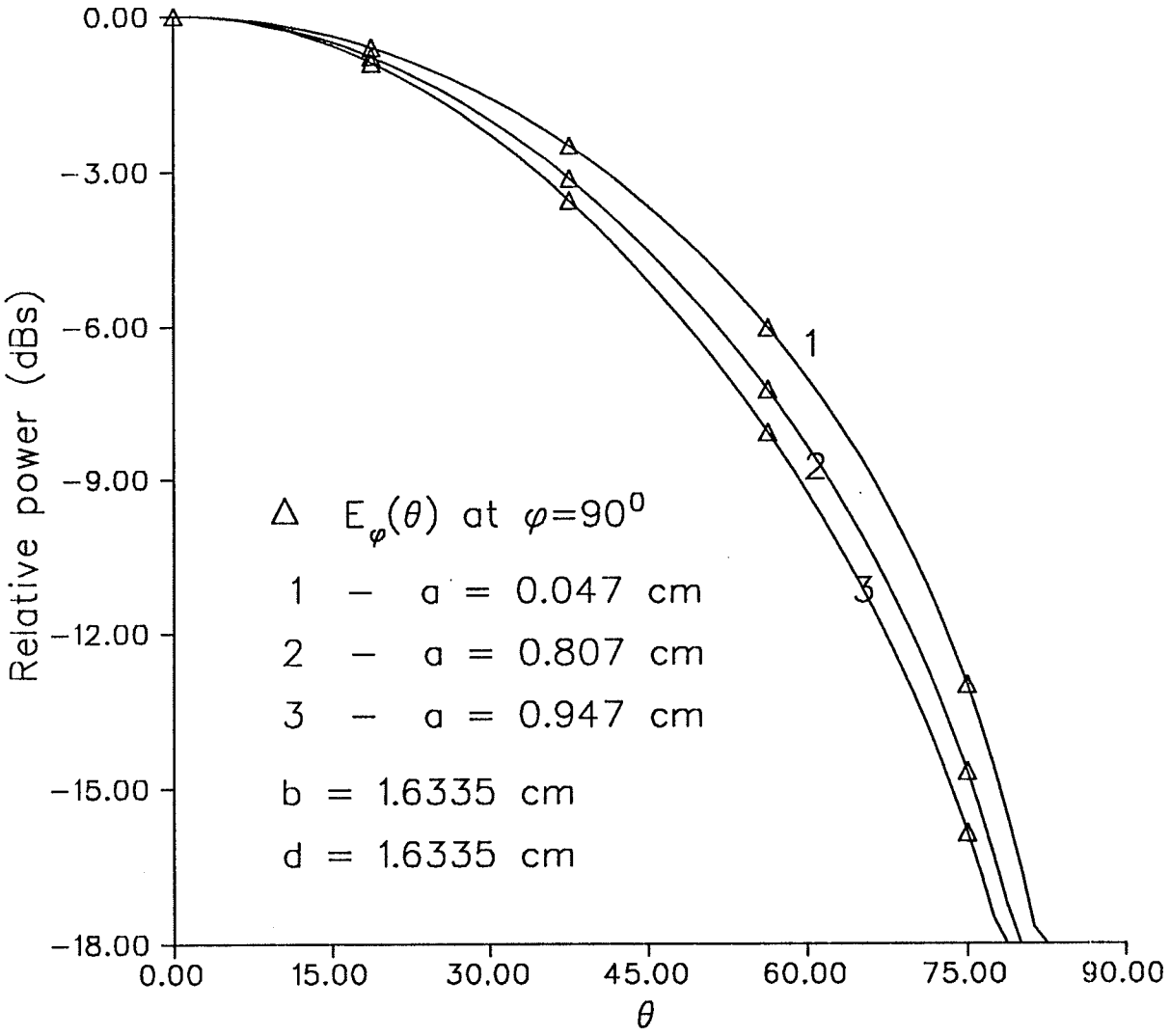

Fig.3.7b: Computed E_φ patterns for a circular patch with central shorts at resonance of the TM_{11} mode, where the outer radius, b, is constant.

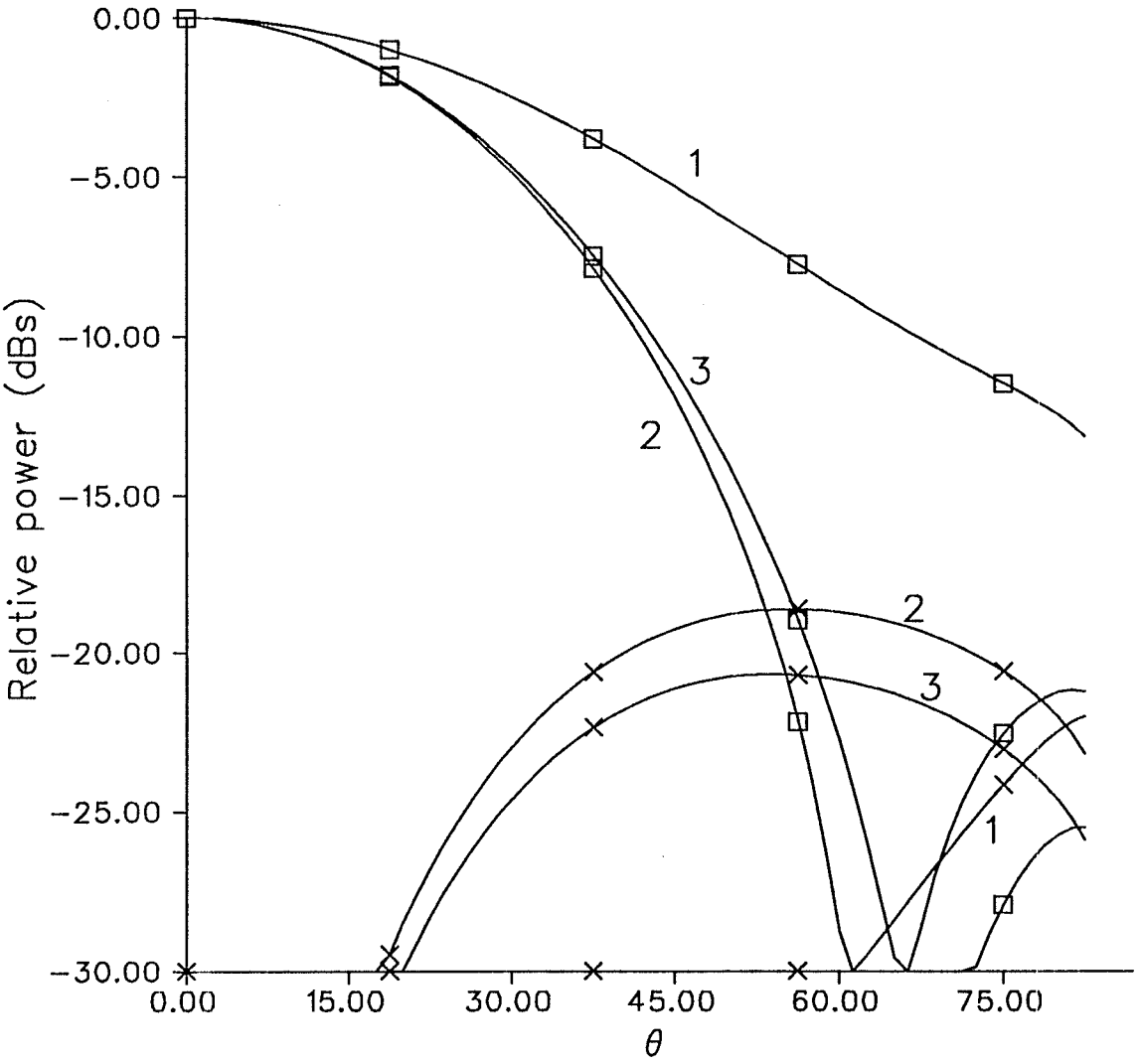

Fig.3.7c: Computed E_θ patterns of the TM_{11} mode for circular patches with a central short at the resonance frequency of 3.7428 GHz

□ $E_\theta(\theta)$ at $\varphi=0^0$, d = b

× Cross polarization at $\varphi=45^0$

1. a = 0.486 cm, b = 1.633 cm
2. a = 1.416 cm, b = 2.495 cm
3. a = 2.109 cm, b = 3.318 cm

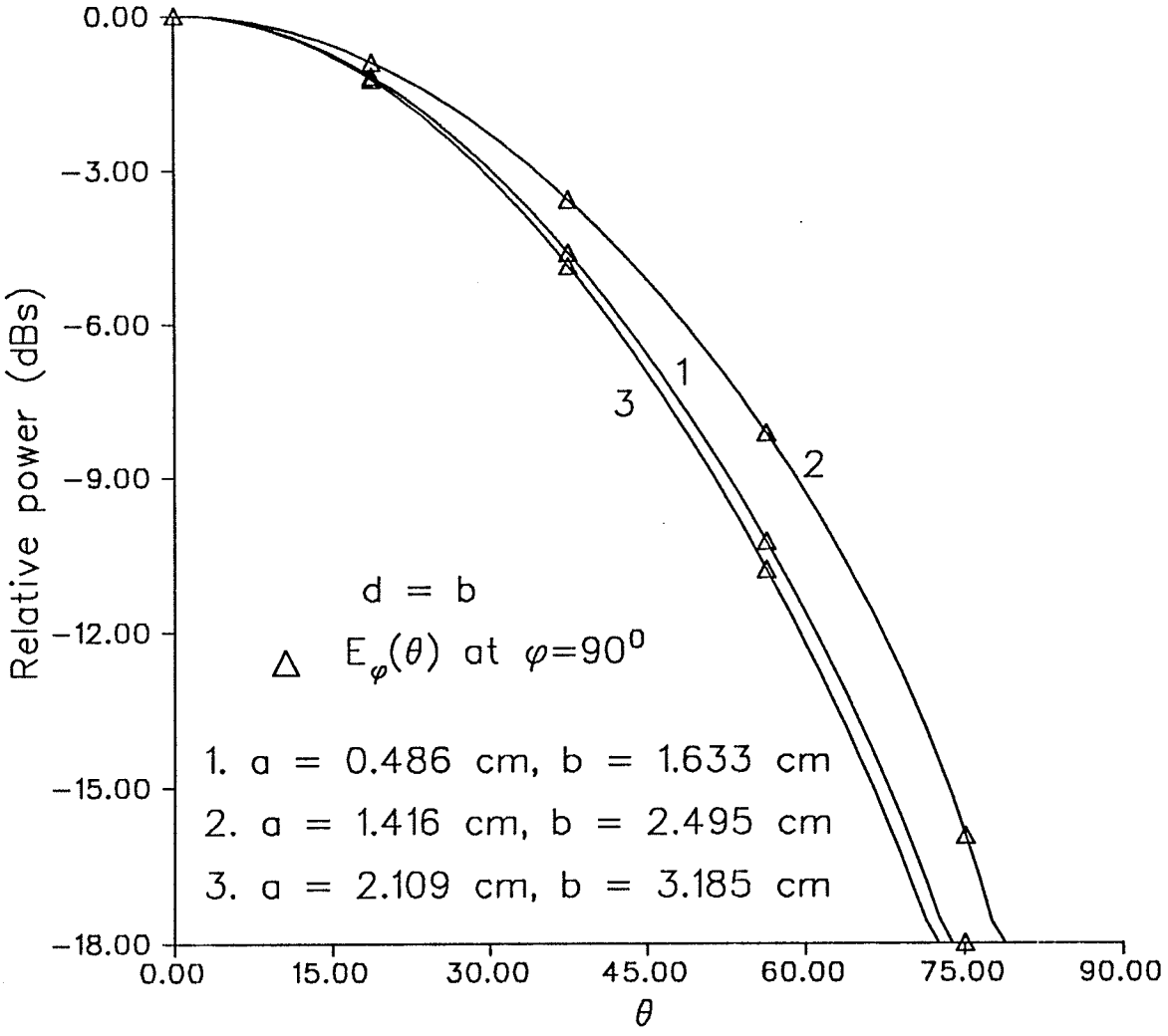

Fig.3.7d: Computed E_φ patterns of the TM_{11} mode for circular patches with a central short at the resonance frequency of 3.7428 GHz

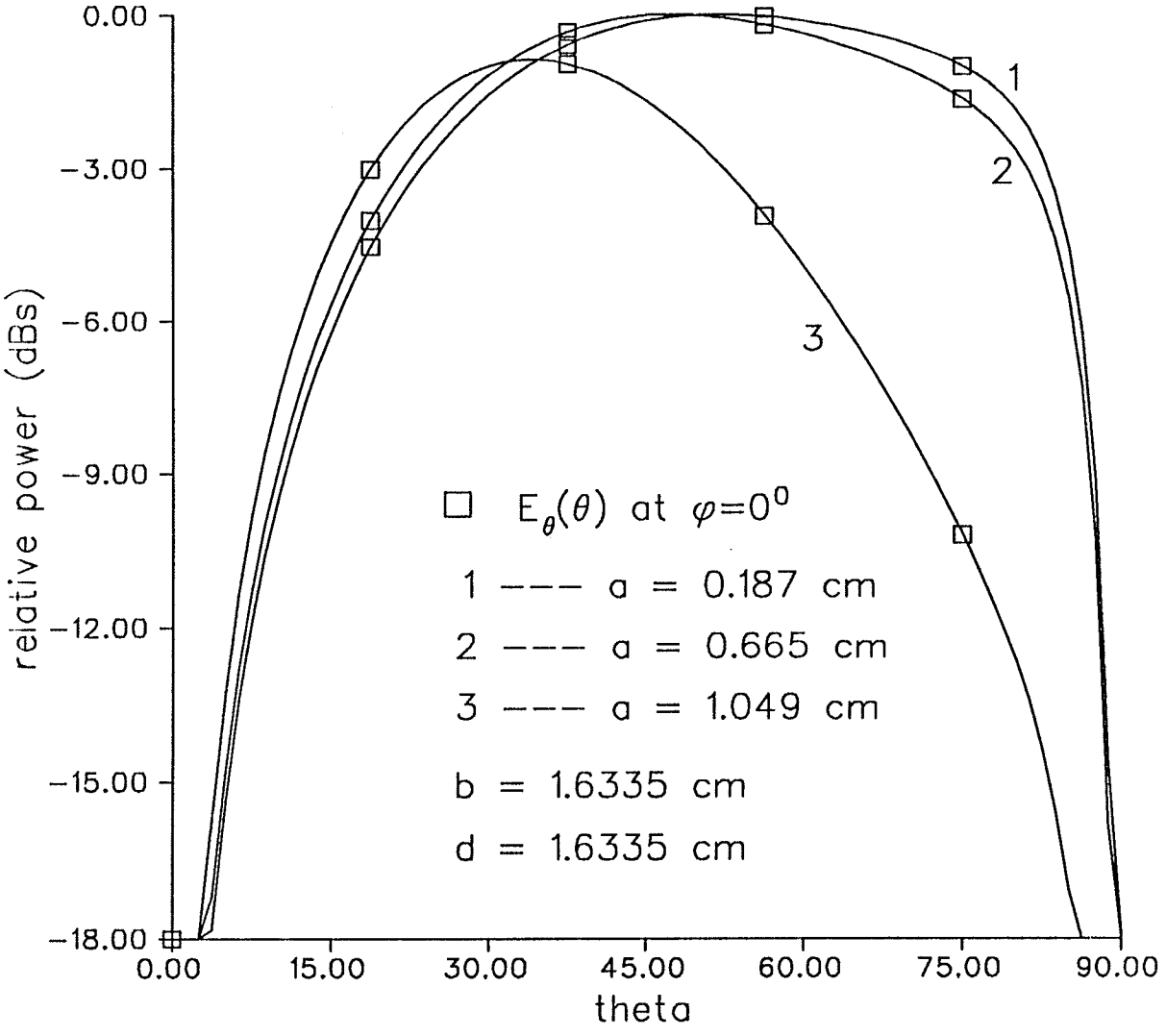

Fig.3.8a: Computed E_θ patterns for a circular patch with central shorts at resonance of the TM_{21} mode, where the outer radius, b, is constant.

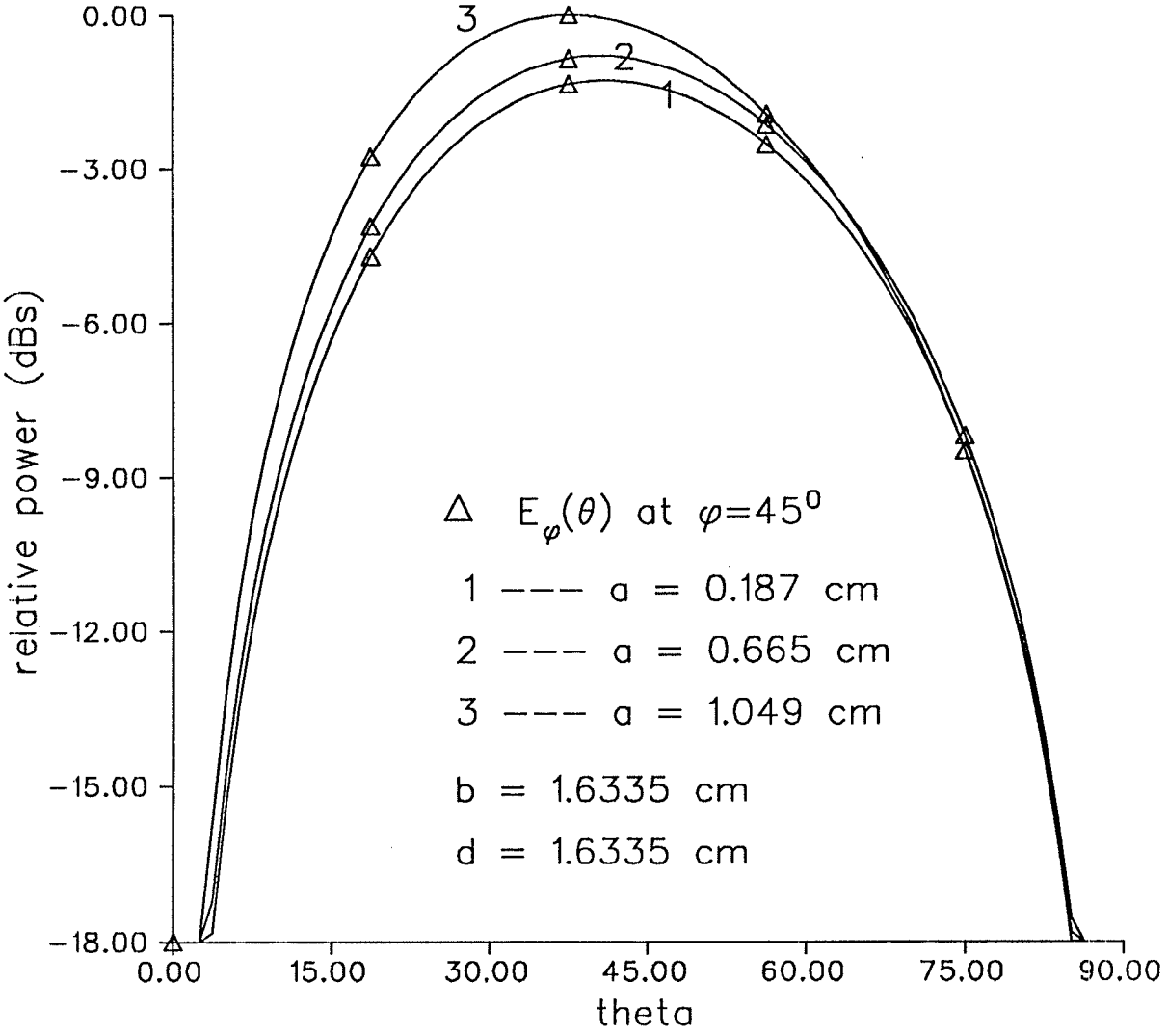

Fig.3.8b: Computed E_φ patterns for a circular patch with central shorts at resonance of the TM_{21} mode where the outer radius, b, is constant.

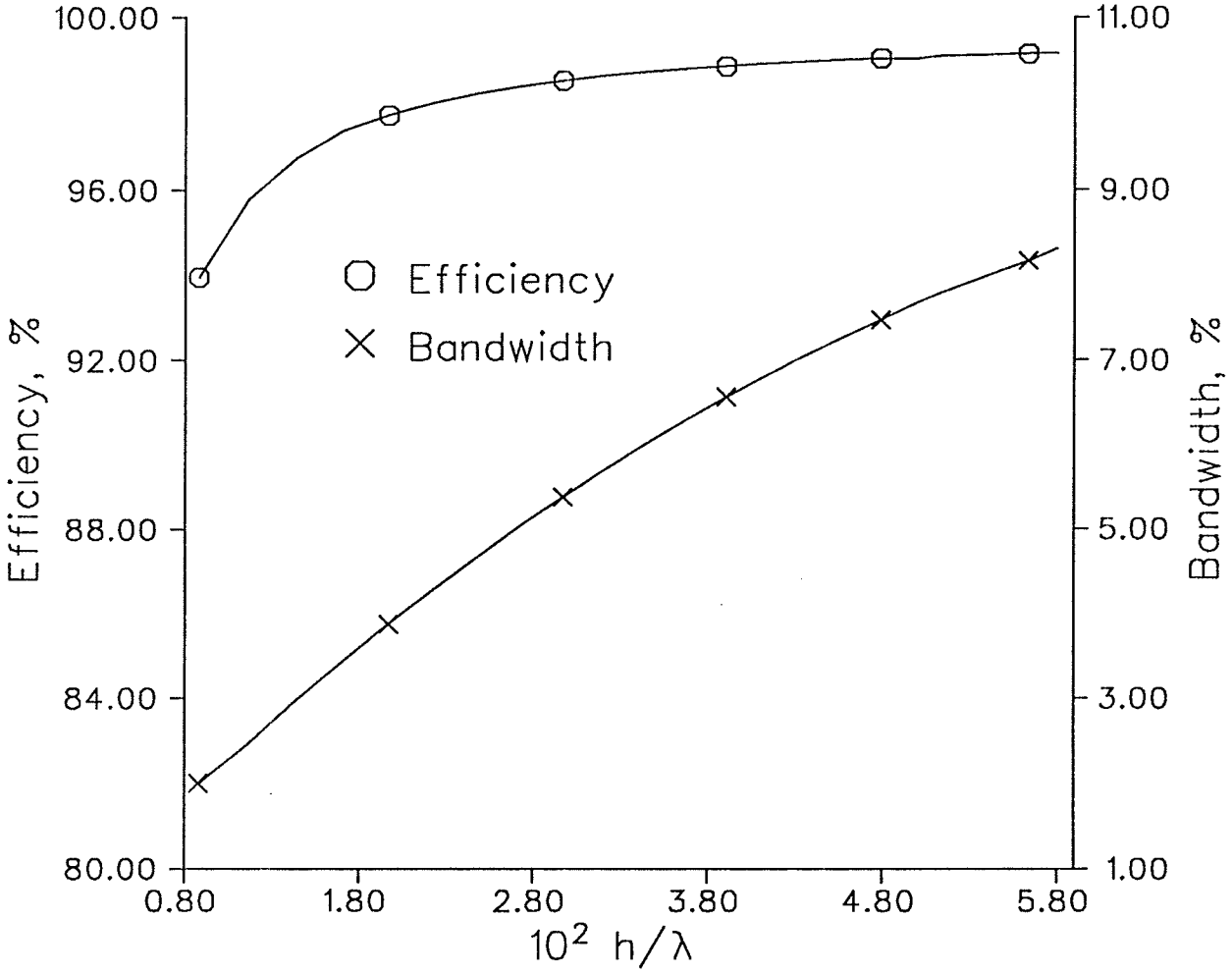

Fig.3.9a: Variation of efficiency and bandwidth with thickness, at resonance of the TM_{11} mode for a circular patch with a central short

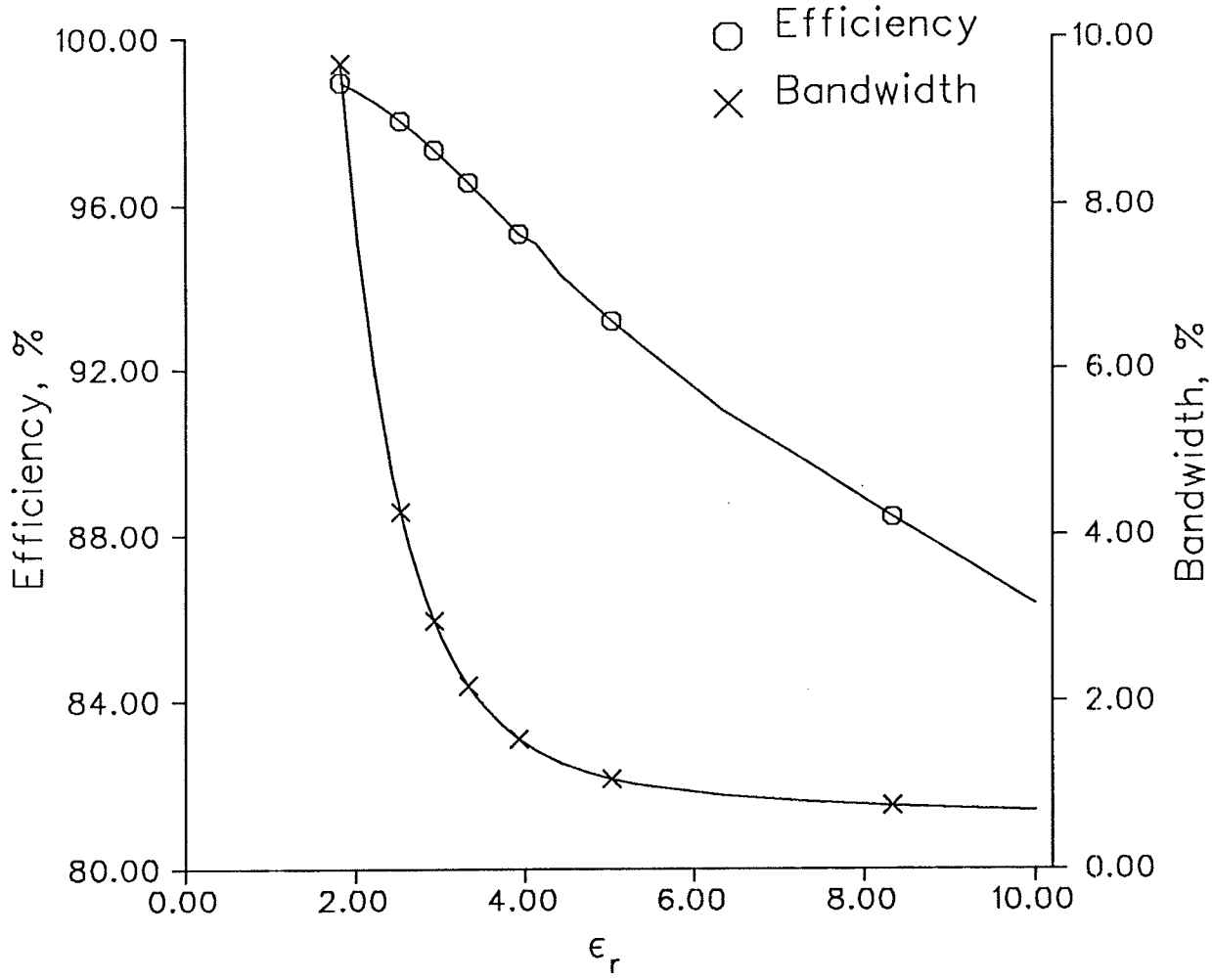

Fig.3.9b: Variation of efficiency and bandwidth with ϵ_r at resonance of the TM_{11} mode for a circular patch with a central short

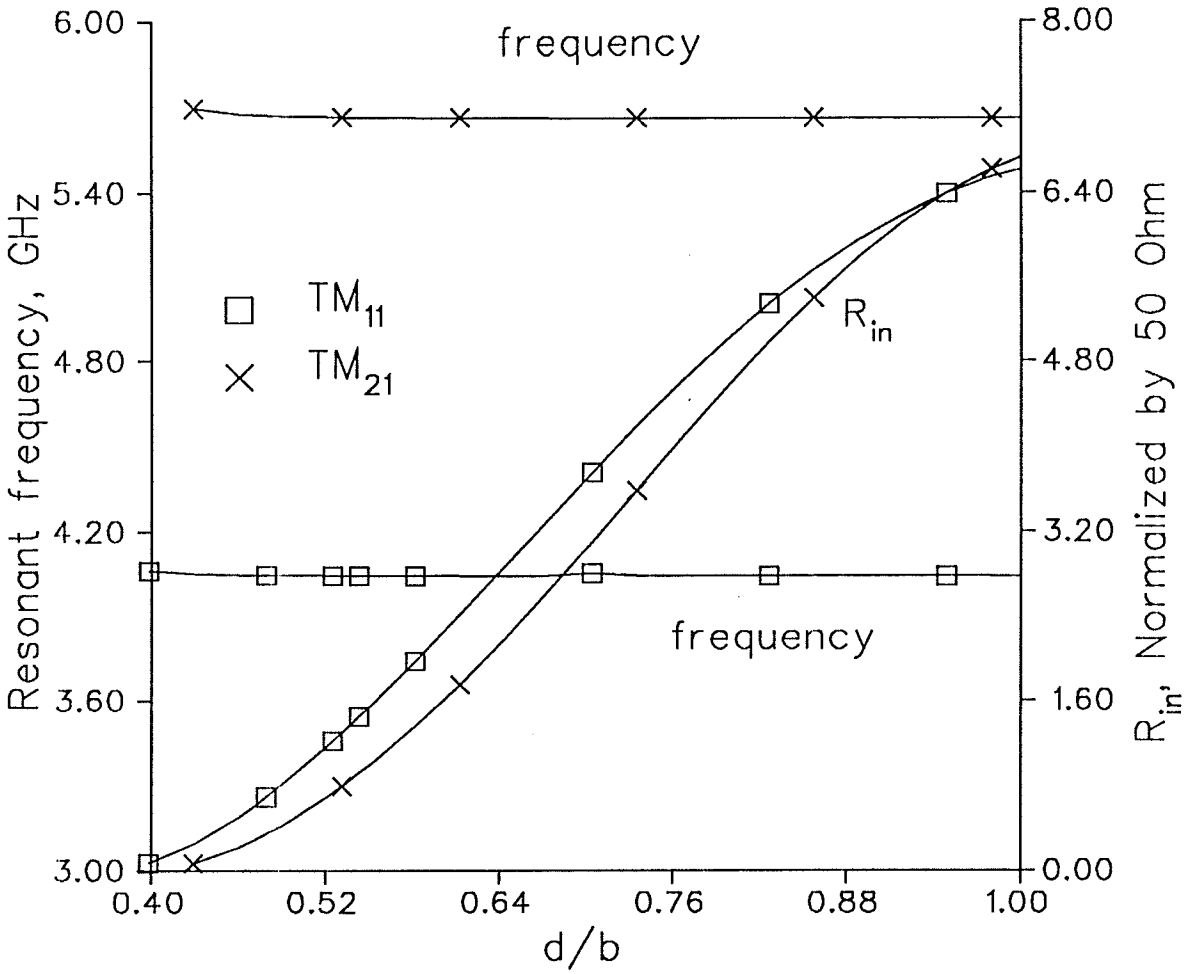

Fig.3.10: Input resistance and frequency at resonance of the TM_{11} and TM_{21} modes for a Circular patch with a central short

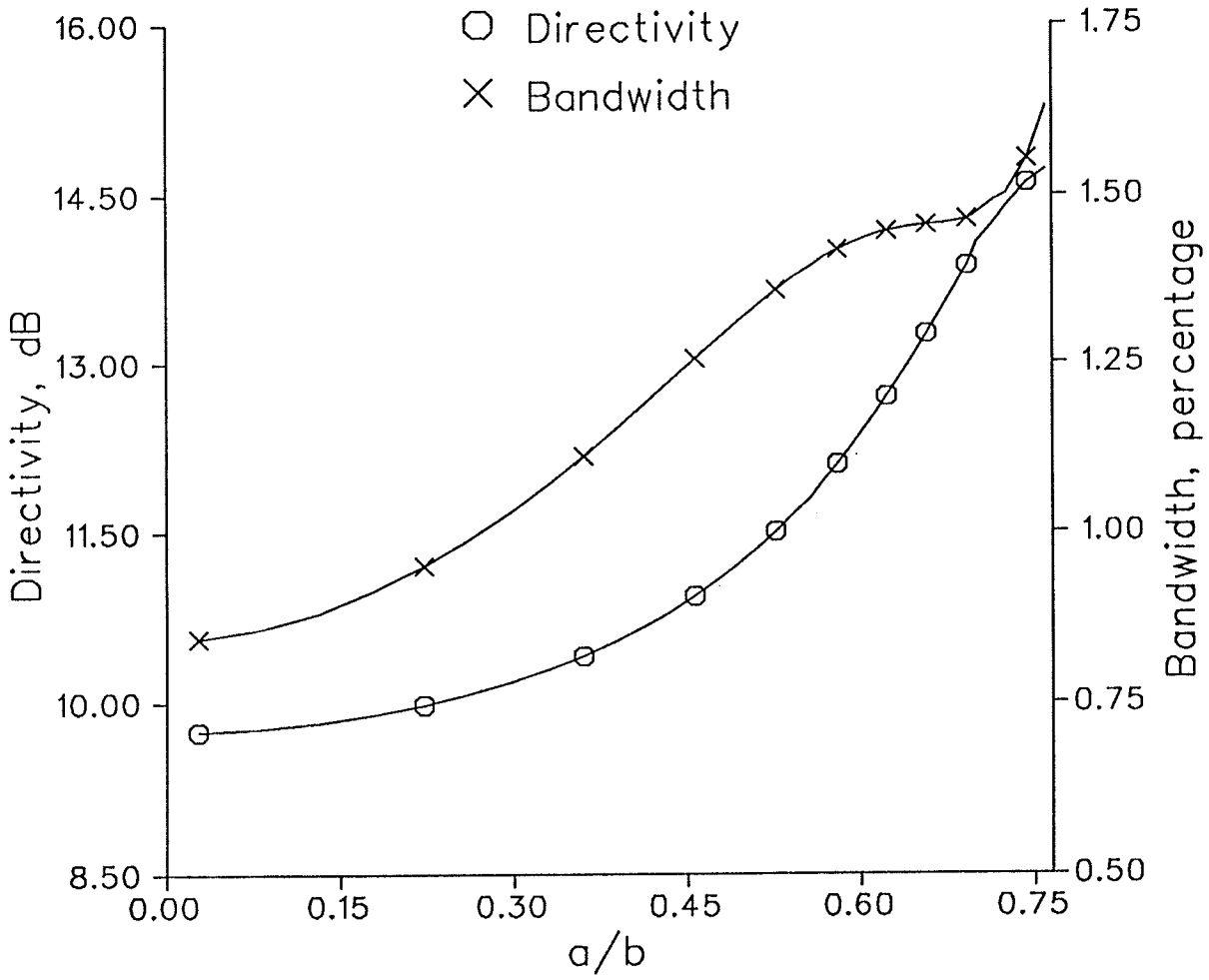

Fig.3.11a: Directivity and bandwidth at resonance of the TM_{11} mode for a circular patch with a central short

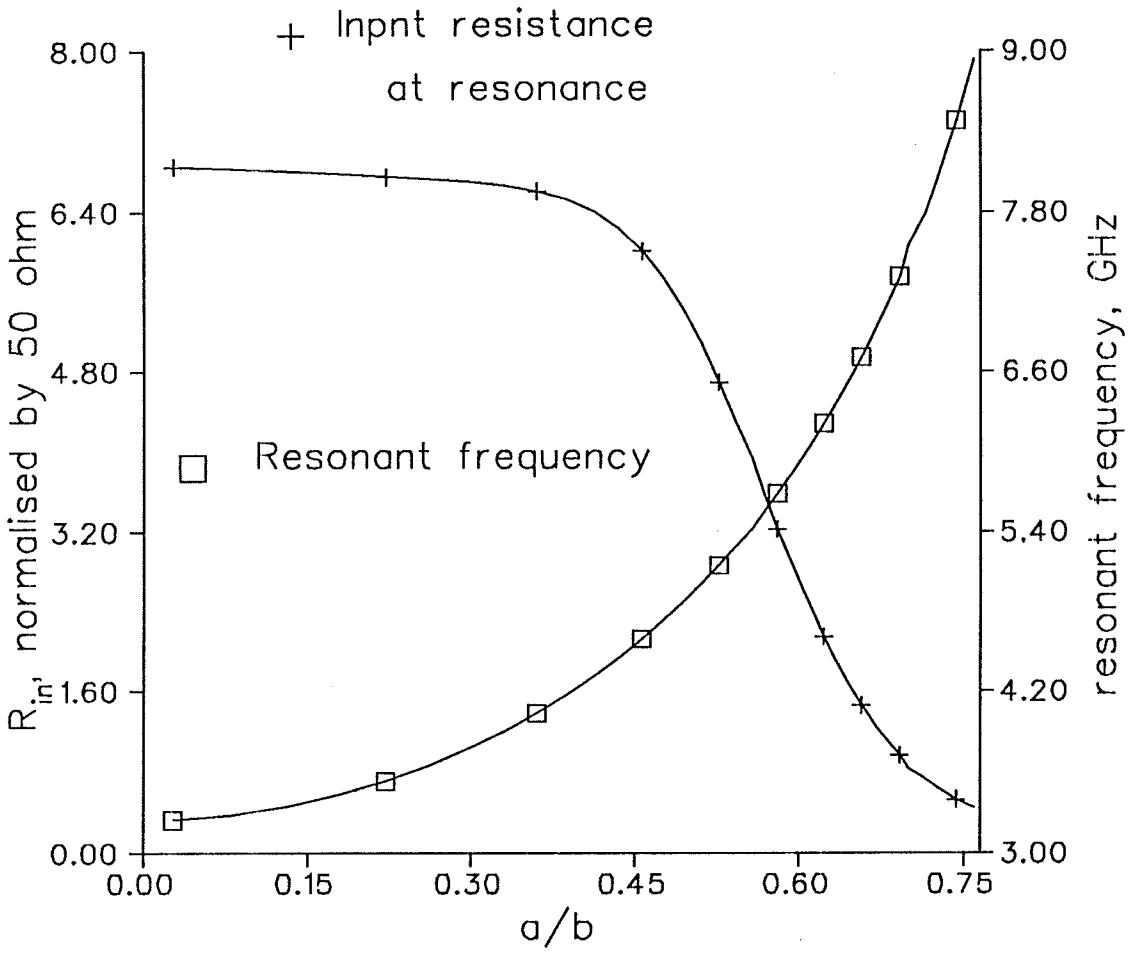

Fig.3.11b: Input resistance and Frequency at resonance of the TM_{11} mode for a circular patch with a central short

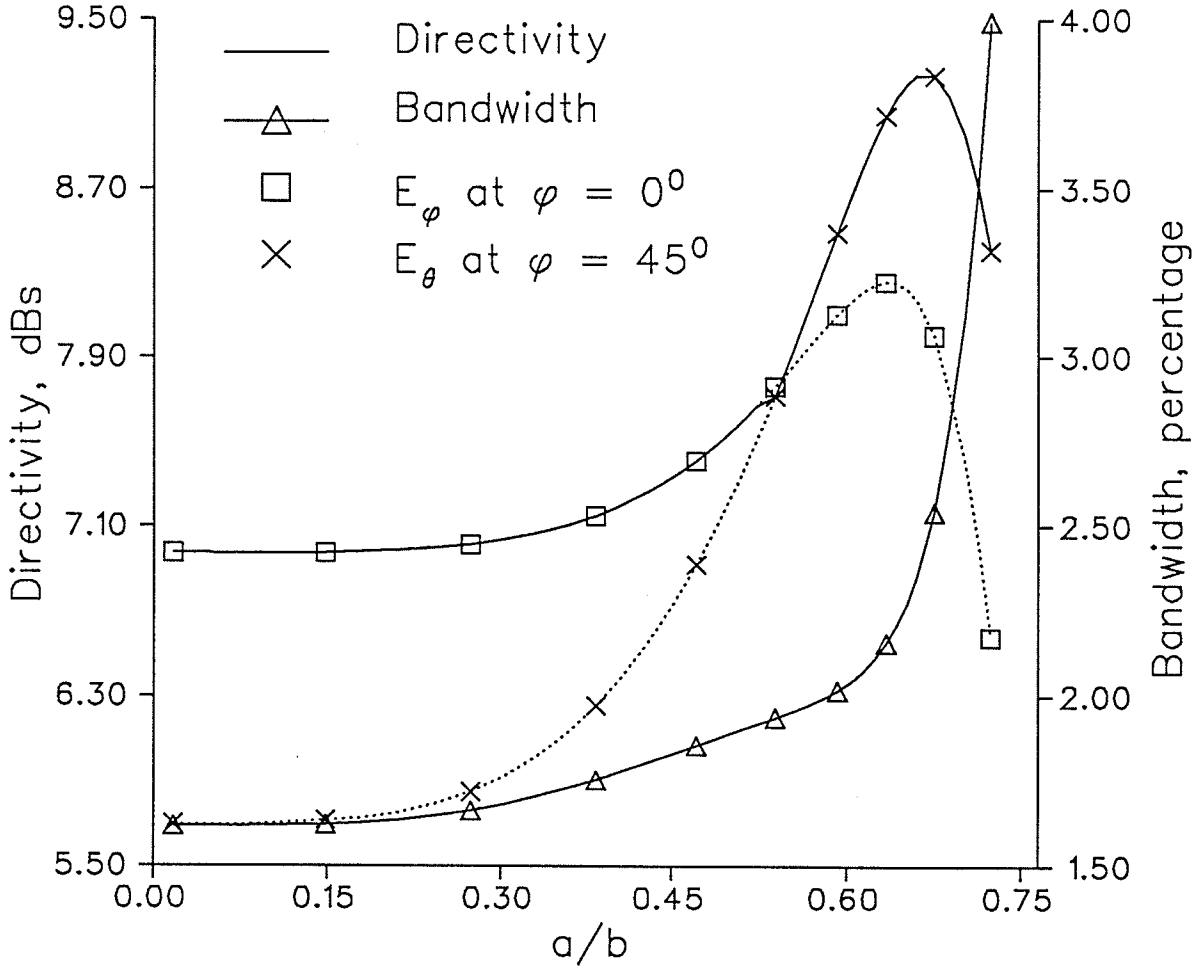

Fig.3.12a: Directivity and Bandwidt at resonance of the TM_{21} mode for a circular patch with a central short

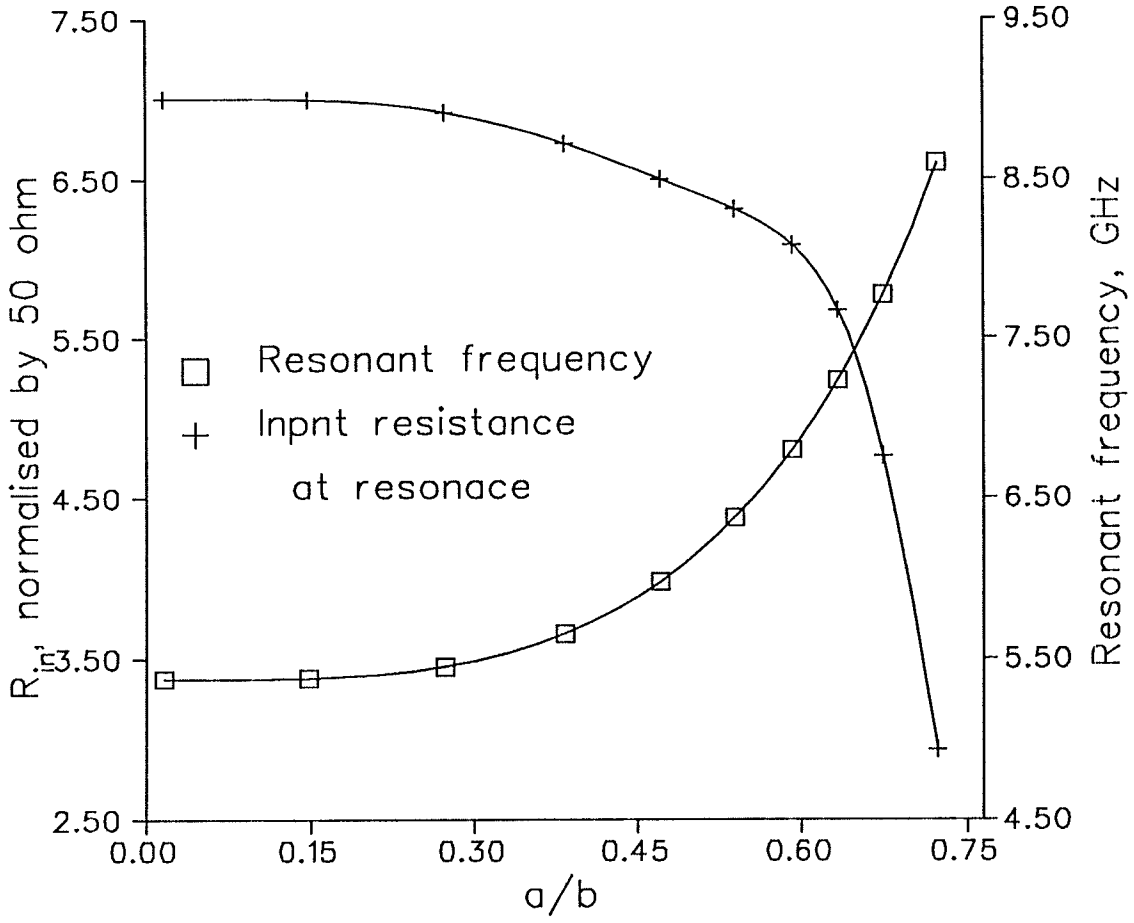

Fig.3.12b: Input resistance and frequency at resonance of the TM_{21} mode for a circular patch with a central short

Chapter 4
Characteristics of Annular Ring Patch Antennas Shorted at the Outer Periphery

4.1. Introduction

The investigation of the concentrically shorted circular microstrip antennas in the previous chapter shows that the introduction of the short in the antenna structure can change the characteristics of the circular patch antennas. Their geometrical sizes and electronic properties can be altered, to some degree, to improve the suitability of the circular patch antenna in practical applications. Since the central shorting increases the radiating aperture, the antenna gain increases. This means that as long as the antenna situations are the same, the gain of a concentrically shorted circular patch antenna is higher than that of a conventional circular patch antenna. However, in some practical applications, such as the global positioning and satellite applications [46], a low antenna gain with a broad radiation pattern would be needed. The antenna proposed in the previous chapter cannot be used in such applications.

The concentrically shorted circular patch microstrip antenna can be considered as an annular ring patch shorted at the inner ring periphery. Instead of shorting at the inner ring, an annular ring patch shorted at its outer periphery forms another type of circular patch microstrip radiating element. The radiating aperture of such an antenna, i.e., the inner periphery of the ring patch, can be smaller than that of an ordinary circular patch antenna. Consequently, its gain could be made flexibly smaller since its aperture can be made arbitrary in size. For a given resonance frequency, its directivity and gain can be quite low, when the inner ring size is reduced to a very small size. On the

other hand, when the inner ring increases to a large enough size, while maintaining the resonance frequency constant, a high gain can be obtained. Thus, more flexible radiation characteristics can be obtained by controlling the ratio of the inner to outer radii of these antennas.

The configuration of the antenna is shown in Fig.4.1. The antenna is modeled as a coaxial cavity bounded by a finite admittance wall at the periphery of the inner edge, with the electrical wall at the outer conducting cylinder and conducting plates on top and bottom. The admittance boundary condition is determined by the radiation power and the fringing field at the inner ring. As shown in Fig.4.1, the dielectric substrate only exists inside the inner ring of the annular antenna. The calculation of the radiation fields can omit the effect of the substrate but the ground plane is assumed to be infinite in extent.

The analytical results are compared with experimental data and available published results. The characteristics of annular ring patch antennas are also studied and compared with the antennas proposed in the previous and present chapters. Although the annular ring antennas are easier to fabricate, their electric performance parameters are more difficult to control. This is due to the fact that in the latter case two radiating apertures at the inner and outer edges contribute to the radiation and the dependence of the antenna characteristics on its radii is more complex. In the centrally and outer shorted circular patch antennas, only one aperture radiates and consequently their gain and radiation patterns can readily be controlled by their shorted radius.

4.2. Modal Field Expressions and Input Impedance

The geometry of the antenna is shown in Fig.4.1, in which compared with Fig.3.1 the notation a and b are interchanged and represent the outer and inner radii of the ring, respectively. Fig.4.2 illustrates the vertically cut cross sections for the ring patch

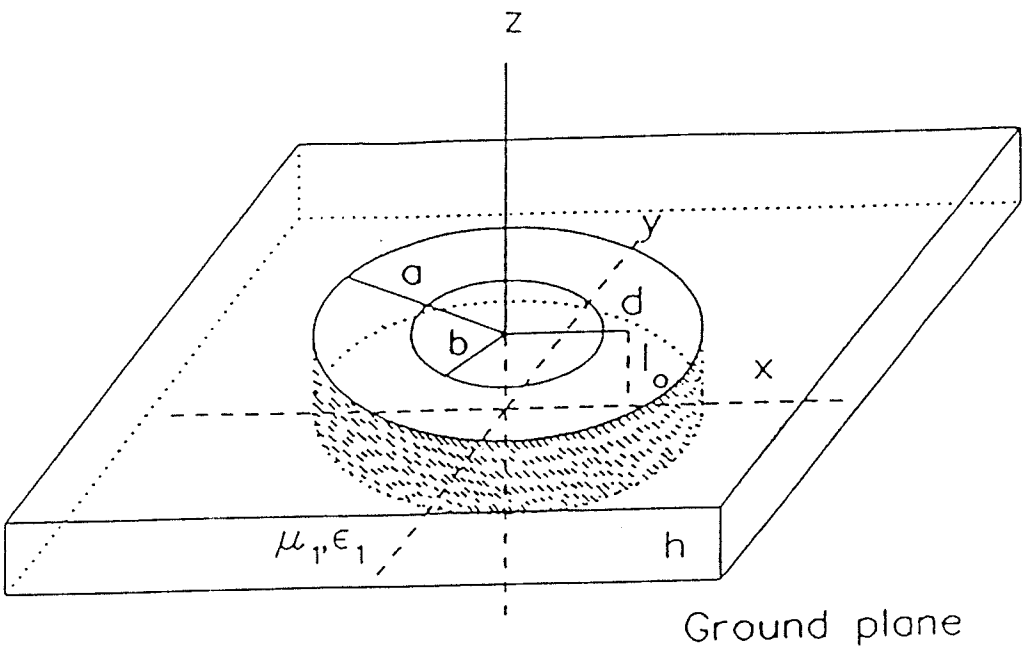

Fig.4.1: Annular ring patch shorted at the outer periphery

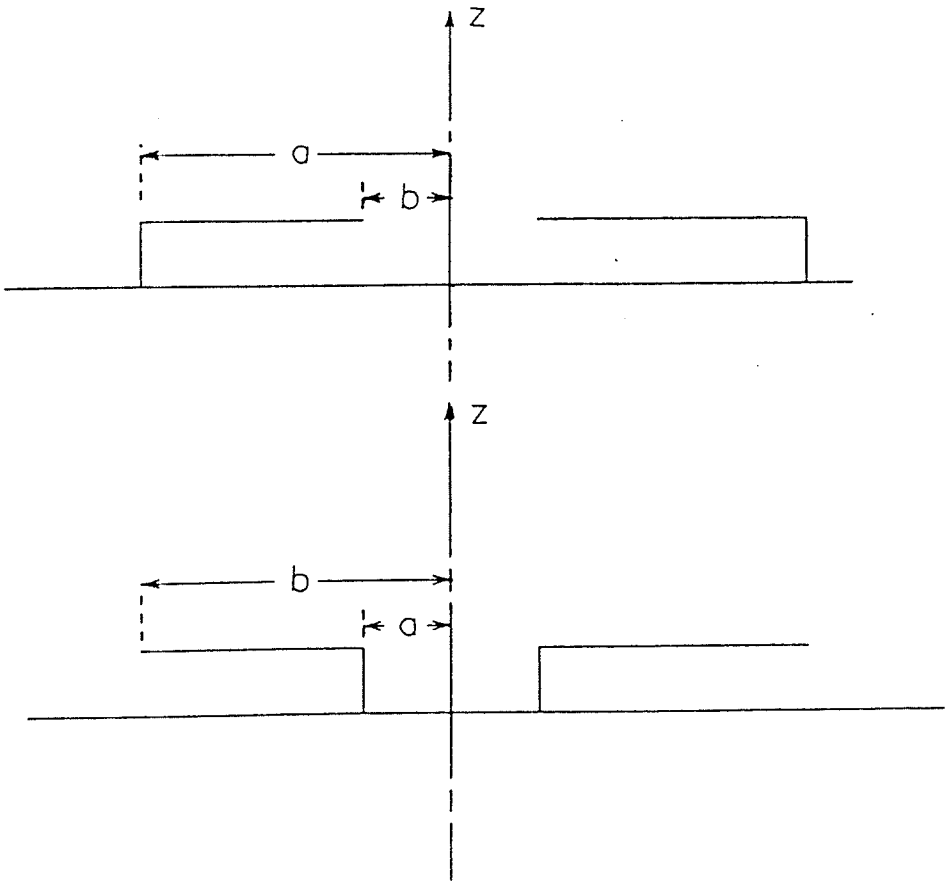

Fig.4.2: Vertically cut cross sections for the ring patch antennas shorted at the outer or inner edge

antennas shorted at inner and outer periphery, respectively. Both antennas are shorted at the position $r = a$ and have a radiating aperture at the position $r = b$.

The cavity model that is applied to this antenna is then similar to that used in the previous chapter. The same physical assumption and conditions are imposed onto the cavity model of this antenna as those in Chapter 3. Therefore, the formulations for the cavity model will be the same. The electromagnetic field excitation is due to the current source:

$$\mathbf{J} = \hat{k}\, I_0 \frac{\delta(r - d)}{r}\, \delta(\phi) \tag{4.1}$$

The existing *TM* modes within the cavity have similar expressions for both antennas and can be calculated using equations 3.2 to 3.19 and 3.28 to 3.36. However, the wall admittance at the radiating edge must be handled differently as shown below.

4.3. The Wall Admittance

The wall conductance can be calculated from the radiation power leaving the side wall [17] in the form

$$g_{sn} = \frac{P_{rad}}{\frac{1}{2}\int_s |\, E_z \,|^2 d\, s} \tag{4.2}$$

The wall susceptance can be found from the energy stored in the volume between the patch edge at b and the assumed magnetic wall at b_e, the so called effective radius. It leads to the following first order asymptotic expression,

$$b_{sn} = \frac{F'_n(\zeta)}{Z_1 F_n(\zeta)} \tag{4.3}$$

where

$$\zeta = k_1 \, b_e, \tag{4.4}$$

and

$$F_n(\zeta) = J_n(k_1 a) Y_n(\zeta) - Y_n(k_1 a) J_n(\zeta) \tag{4.5}$$

For calculating the effective radius b_e, the 0 order capacitance equivalent method used in the previous chapter is not recommended, since the radiation and the fringing no longer occur at the outer periphery, $r = a$. In the case when b is relatively small, the equivalent radius $b_c = \sqrt{a^2 - b^2}$ is closer to a than to b. This causes intolerable errors for computing the resonance frequency.

The radiation from the inner circle of the ring patch shorted at the outer periphery can be considered as the radiation from the circular slot backed by a cavity. Therefore, the annular ring antenna shorted at the outer periphery can be considered as a slot antenna. To analyze the slot antenna, the duality principle may be applied [47]. This means that the field caused by the circular slot on an infinite and thin conducting screen is equal to the field caused by its complementary conducting circular patch [47], as shown in Fig.4.3.

By the duality principle, the circular slot with a radius b is replaced by its complementary circular patch with the same radius b. The parameter Δ_b, to account for the effect of the fringing field due to the complementary circular patch, is then calculated using the following equation [48]:

$$\Delta_b = \frac{2\,h}{\pi\, b\, \varepsilon_r}\left[\ln\left(\frac{b}{2\,h}\right) + 1.41\varepsilon_r + 1.7726 + \frac{h}{b}(0.268\varepsilon_r + 1.65)\right] \tag{4.6}$$

The effective radius, p, of the circular slot on the infinite conducting screen can be assumed as

$$p = b\,(1 - \Delta_b)^{1/2} \tag{4.7}$$

The minus sign in front of Δ_b is taken to reduce the effective radius. Since the fringing field at the edge of the slot is inward, the assumed magnetic wall is moved toward the center of the slot, as shown in Fig.4.4.

The infinite screen can be considered as a circular screen with a short at radius $a = \infty$. The short at $a = \infty$ does not affect the fringing field. However, the circular slot is not located on the infinite screen. For a short at the finite radius a, the fringing field starting from $r = b$ is further stretched toward the center of the slot, as shown in Fig.4.4. This means that an extra reduction of the inner radius has to be introduced to include the effect of the shorting at $r = a$. This is done by considering a reduction related to a, as shown in Fig.4.4, and is assumed as

$$a_e = a(1-\Delta_a)^{1/2} \tag{4.8}$$

where

$$\Delta_a = \frac{2h}{\pi\varepsilon_r a}\left[\ln\left(\frac{a}{2h}\right)+1.41\varepsilon_r+1.7726+\frac{h}{a}(.268\varepsilon_r+1.65)\right] \tag{4.9}$$

The effective inner radius, b_e is then assumed as the following equation,

$$b_e = p - a + a_e \tag{4.10}$$

The approximate wall susceptance can now be obtained by substituting eqn.4.10 into eqns 4.3 to 4.5.

The effective radius b_e will be applied in the following sections to determine radiation characteristics.

4.4. Radiation Fields

As shown in Fig.4.1, the radiation occurs at the inner periphery of the ring patch and the shorting at the outer periphery truncates the dielectric substrate. The antenna itself is located at an infinite ground plane. There is no dielectric beyond the outer periphery of the ring patch. Therefore, for the radiation fields, the effect of the dielectric substrate can be omitted for this antenna.

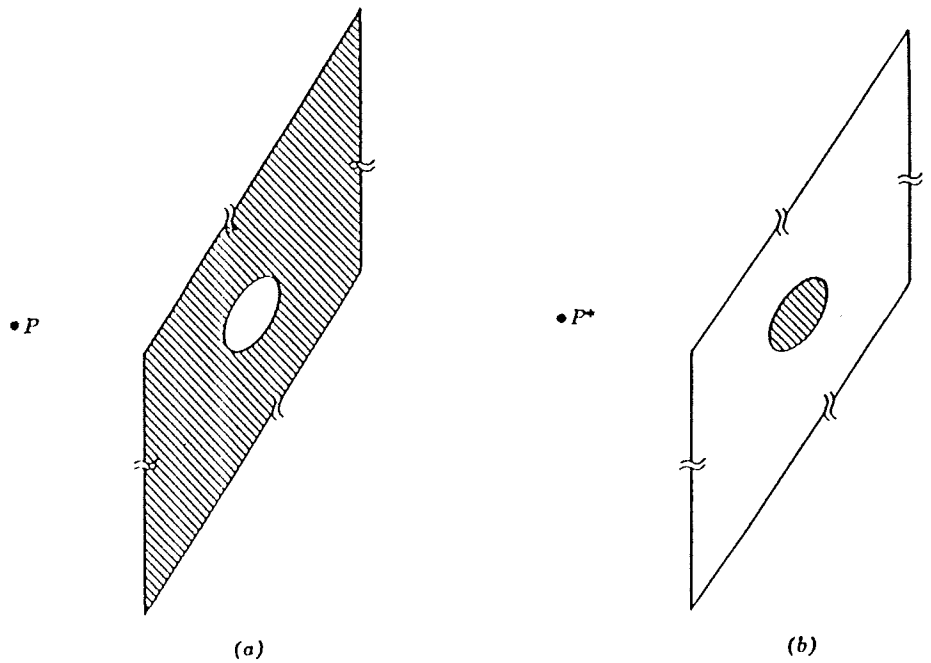

Fig.4.3: Complementary screens. (a) Infinite, thin conducting screen with apertue. (b) Complement of screen with apertue.

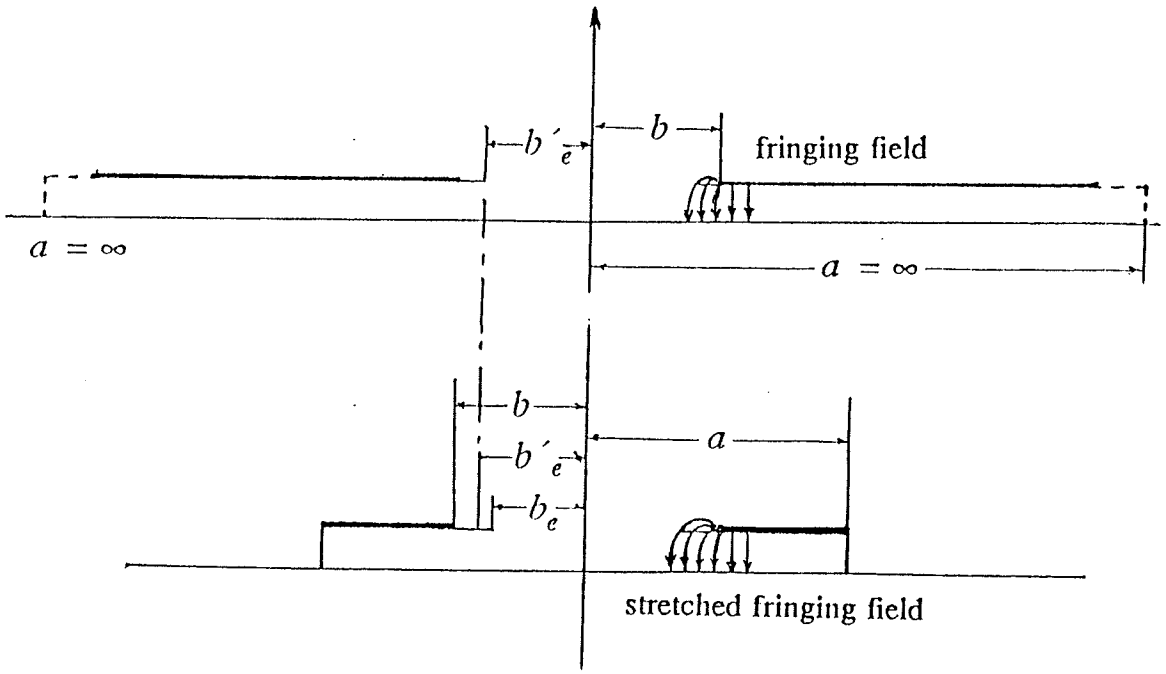

Fig.4.4: The calculation of the effective radius b_e

The far fields are calculated from the vector electric potentials

$$\mathbf{F}(r) = \frac{1}{4\pi}\frac{e^{-jk_0 r}}{r}\int_s \mathbf{M}(r)e^{jk_0|\mathbf{r}-\mathbf{r}'|}\ d\ s' \tag{4.11}$$

where $\mathbf{M}(r)$ is the surface magnetic current on the radiation aperture at $r = b_e$, S is the aperture ring with a width h.

The electric fields in the far zone can be obtained from

$$E_\theta = -j\ k_0\ F_\theta \tag{4.12}$$

$$E_\phi = -j\ k_0\ F_\phi \tag{4.13}$$

which are of the form

$$E_{\theta n} = \frac{j^{n+1}}{2}\ h\ \cos n\phi\ \ [k_1 b_e\ f_{n2}(k_1 b_e)\ J'_n(k_0 b_e \sin\theta) \tag{4.14}$$

and

$$E_{\phi n} = \frac{j^{n+1}}{2} k_1\ n\ h\ \ \frac{\sin n\phi}{k_0 \sin\theta}\ f_{n2}(k_1 b_e)\ J_n(k_0 b_e \sin\theta) \tag{4.15}$$

where f_{n2} and other parameters are as defined in Chapter 3. Note that the distance term $\frac{e^{-jk_0 r}}{r}$ is omitted from eqns 4.14 to 4.15.

The effect of the ground plane is taken into account by the image theory. The following factor [22]

$$F_i = \frac{\sin(k_0 h\cos\theta)}{k_0 h\cos\theta} \tag{4.16}$$

is multiplied to eqns 4.14 and 4.15 to complete the radiation field expressions.

4.5. Results and Discussion

At the resonance of TM_{11} to TM_{61} modes, the dependence of the outer radius b on the inner radius a is the same as those shown in Fig.3.5, where the notations b and a represent the inner and outer radii, respectively. This means that similar to the centrally shorted circular patch antenna for the TM_{11} mode the parameter b, the shorted outer radius, can be used effectively to alter the antenna size and thus its radiation pattern and gain.

Two antennas, A and B, were fabricated and tested. Their dimensions were a=4.8963cm, b=1,4533 cm (i.e., b/a=0.297) and the feed position at d=4.901cm for model A (the substrate thickness h=3.175 mm); and a=3.36cm, b=0.9991cm and d=2.817cm for model B (h=1.585mm). The permittivity of the substrate is 2.52 for both antenna models.

Fig.4.5 shows the comparison of the experimental and calculated input impedances of the TM_{11} mode for the model A, where the gauss-jacobi quadrature formula is used to calculate the stored energies. The dielectric loss tangent of the substrate is 2.2×10^{-3} and the conductivity of the patch, the inner conducting wall and the ground plane is assumed to be 1.8×10^{7} mho/m, which is a reduced conductivity to account for surface roughness.

For model A the calculated resonance frequency of the TM_{11} mode is 2.207461 GHz, and the measured one is 2.19913 GHz. The differences are less than 1 % and computed and measured input resistances show good agreement in Fig.4.5. For model B, the calculated and measured resonant frequencies are 3.153243 GHz and 3.167 GHz, respectively, which coincide well.

The computed data are also compared with the measured results in [49]. For an antenna with dimensions b/a=0.598, a=4.8963cm and h=3.175 mm, the calculated resonance frequency is 2.908977 GHz and the measured one is 2.8999 GHz. They show very good agreement. Also, the calculated gain is compared with the measured

one in [49] for this antenna. They are 5.53987 dB (computed) and 5.7 dB (measured), which are close to each other.

The above comparison for both small and large values of b/a shows that the approximation for the computation of the wall admittance in section 4.3 is good enough from the engineering point of view. For more accurate analysis, further investigation on the wall admittance may be more strictly carried out by analytical or numerical methods.

The input resistance and frequency at resonance v.s. the feed position d are shown in Fig.4.6 for the TM_{11} mode. As the feed moves from the radiating edge of the patch to the outer shorted periphery, the input resistance at resonance decreases rapidly and at some point reaches 50 Ω. On the other hand, the resonance frequency remains relatively constant. This is similar to the ordinary circular patch antennas.

In Figs 4.7- 4.9, different pairs of b and a are selected to keep the resonance frequency at 3.153649 GHz for the dominant TM_{11} mode and the antennas are excited by a probe in the inner edge of the ring patch. Fig.4.7 shows the outer radius and input impedance at resonance of the TM_{11} mode v.s. the ratio b/a. Similar to the concentrically shorted patch antenna, the input resistance at resonance decreases as the ratio of b/a increases, and at $b/a = 0.87$ it equals 50 Ω.

Fig.4.8 illustrates the gain and directivity of these antennas v.s. b/a. It shows that they vary from values much lower than those of conventional circular patch to values as high as those of the centrally shorted ones. This is one of the advantages of such antennas. The wider varying range of gain and directivity expand their uses in practical applications.

Fig.4.9 depicts the relationship between the bandwidth and efficiency at resonance v.s the ratio b/a. Both bandwidth and efficiency of such antennas are poorer than those of the conventional circular patch ones. They show that, in these respects, these antennas are more like conventional annular ring patch antennas operating at the dominant TM_{11} mode. However, their narrow bandwidth and considerably lower efficiency

make them less attractive antenna candidate for small value of b/a.

More interesting results are shown in Figs 4.10-4.12, which illustrate the computed radiation patterns of three antennas with different ratios b/a to maintain the resonance frequency at 3.153649 GHz. All these antennas are fed at the inner edge by a probe.

In these figures the pattern shapes change with the change of the ratio of b/a. Both H-plane and E-plane pattern beamwidths decrease as the ratio b/a increases. Since the beamwidth of the E-plane pattern decreases faster than that of the H-plane, by choosing suitable b/a, one can make the two patterns to coincide. Fig.4.11 shows one such case, where the patterns at two principal planes are nearly the same for $b/a = 0.6022$. This is verified by the measured patterns shown in Fig.4.13 [49], where the ratio of radii is $b/a = 0.598$. The similarity of the principal plane patterns can be used to obtain the 45^0 linear polarization and circular polarizations. The later is a desirable characteristic in the global positioning systems which transmit right hand circularly polarized signals. When b/a becomes larger, a side lobe appears in the H-plane pattern, as shown in Fig.4.12. Its high level side lobe causes the drop in the gain and the directivity as shown in Fig.4.8.

The above calculated and experimental data show that the proposed antennas can provide a wider range of gain, symmetric principal plane patterns and varying input impedance values. Their superior features, when operating at the dominant TM_{11} mode, remedy the poor performance of the conventional annular ring patch antennas operating at the TM_{11} mode.

4.6. Conventional Annular Ring Microstrip Antennas

One may ask why not to alter the inner radius of an annular ring patch structure to modify the performance parameters. It is easier to fabricate an annular ring than the

proposed antennas since the inner wall does not need to be metallized. To investigate their difference with the antennas proposed in the previous and present chapters, similar data of annular ring antennas are calculated according to [39] and presented for comparison.

Fig.4.14 shows the mode charts of TM_{n1} modes of annular ring patch antennas. For the TM_{n1} modes, the relative outer radius b/λ decreases from b_{cd}/λ to $n/2\pi$, as a/λ increases from zero to $n/2\pi$, where the subscript cd represents the limiting case of an ordinary circular disk, and for $n = 1$, $b_{cd}/\lambda = 1.841/2\pi$, etc. For a given frequency, increasing the inner radius a decreases the outer radius b, i.e, the antenna size. The inverse relationship between the radii of the ring may cause the gain to decrease. One cannot evaluate their performance parameters from the mode chart of the dominant TM_{11} mode, until more detailed results are properly obtained. As shown in Fig.4.15, for the TM_{n2} modes, b first decreases to a minimum value and then increases linearly, as a increases. The linear dependence of b on a after the minimum value may be used to alter the performance parameters.

Tables 4.1 and 4.2 illustrate the characteristics of TM_{12} and TM_{11} modes, respectively, at the resonant frequency of 3.7428 GHz. In Table 4.1, most performance parameters are similar to those shown in Table 3.2, but the antenna size is much larger than that of centrally shorted one. The other difference is of about 10% lower radiation efficiency for the annular ring at the small ratio of a/b. The second row in Table 4.1 lists the performance parameters corresponding to the minimum value of b in Fig.4.15. That is, there is a minimum antenna size for every given operation frequency.

Table 4.2 illustrates that the input resistance at the resonance is extremely high and increases rapidly as a increases. This means, the dominant TM_{11} mode of annular ring antennas can hardly be used for antenna application.

For the TM_{11} and TM_{12} modes, the corresponding relationship between the inner radius a and the resonant frequency, the input resistance, the directivity and the bandwidth are shown in Figs.4.16-4.19, where the patch size (the outer radius b) is

kept constant ($1.6335cm$) and the antenna is fed at the edge of the patch. Figs 4.20-4.21 show the radiation patterns of the annular ring with different values of a while maintaining b constant.

Fig.4.16 shows that the input impedance at resonance increases rapidly from a large value to an extreme value, in excess of 1000 Ω, as a increases. Also, the resonance frequencies decrease as a increases. Both features are different from those of the antennas proposed in the previous and present chapters. Fig.4.17 shows that while the directivity drops very slowly, the bandwidth decreases fast, as the inner radius a increases. This means that the annular ring patch structures operating at the dominant mode have much narrower bandwidths and much higher input impedance values than those of ordinary circular patch antennas. The performance parameters shown in the above two figures suggest that the dominant mode can be hardly used for practical antenna applications.

b/a	a (cm)	b (cm)	$R_{in}(\Omega)$	$D.(dB)$	$BW(\%)$	$effi.(\%)$
106.59	.0407	4.3345	70.475	8.3305	0.6421	85.292
4.726	0.8548	4.0400	80.608	11.2369	0.6590	85.292
2.885	1.5067	4.3471	56.082	11.3346	1.0157	90.605
1.893	2.9734	5.6293	23.698	10.6049	2.0028	95.278
1.510	5.0919	7.6907	16.696	12.2188	2.1659	95.633

Table 4.1. Ratio of b/a, radii a and b, input resistance, directivity, bandwidth and efficiency of annular ring antennas at the resonant frequency of 3.7428 GHz for the TM_{12} mode with $d = b$, $\varepsilon = 2.52$ and$h = 1.585mm$

For the TM_{12} mode, the resonance frequency and the input impedance have minimum and maximum values corresponding to the minimum value of b, as shown in Fig.4.18. When b is larger than this minimum value, the behavior of these features are similar to that of antennas proposed in the present and previous chapters. In Fig.4.19, the directivity and bandwidth oscillate with a.

Fig.4.20 illustrates the computed radiation pattern shapes with no significant change as a increases.

Fig.4.21 indicates that the side lobes which are close to and almost as high as the main lobe are the reason for the oscillations in Fig.4.19. Usually, high side lobes are undesirable for antenna applications and the oscillations of the directivity and bandwidth make the antenna design hard to handle. Also, as shown in Fig.4.16, the very high input impedance at resonance for both modes makes the impedance matching between the feeding system and the antenna a difficult task.

b/a	a (cm)	b (cm)	$R_{in}(\Omega)$	$D.(dB)$	$BW(\%)$	$effi.(\%)$
36.854	0.0413	1.4926	446.213	7.1430	1.1206	91.307
11.694	0.1258	1.4712	480.124	7.1335	1.0275	90.804
6.923	0.2037	1.4332	548.963	7.1157	0.9304	89.844
4.771	0.2885	1.3766	680.597	7.0912	0.8006	88.198
3.521	0.3704	1.3040	927.179	7.0643	0.5184	85.620

Table 4.2. Ratio of b/a, radii a and b, input resistance, directivity, bandwidth and efficiency of annular ring antennas at the resonant frequency of 3.7428 GHz for the TM_{11} mode with $d = b$, $\varepsilon = 2.52$ and$h = 1.585mm$

Fig.4.22 shows the radiation patterns for three pairs of b and a of TM_{12} mode at the resonant frequency of 3.7428 GHz. It shows that for larger a values the side lobe decreases and moves away from the main lobe, thus improving the antenna performance.

Although operating in higher modes with larger values of the inner radius a, annular ring patch structures may be used to alter the performance parameters and may have performance parameters comparable with those of a centrally shorted patch. The performance modification for small values of a is less significant.

4.7. Conclusion

The characteristics of annular ring patch antenna shorted at the outer periphery were presented and discussed in this chapter. The antenna was modeled as a coaxial cavity to determine the field distributions inside the cavity. The near-field and far-field properties were studied and compared with experimental data. The comparison substantiated the analytic results. The performance parameters of the conventional annular ring patch antenna were also presented. The comparison between these antennas showed that the proposed antenna remedies the poor performance of the conventional annular ring antenna operating at the dominant TM_{11} mode. The results also showed that the proposed radiating element is a useful antenna with flexible electrical properties. Its geometry and flexible characteristics can give the antenna designer ample opportunity to control its electrical performance parameter to meet different design specifications.

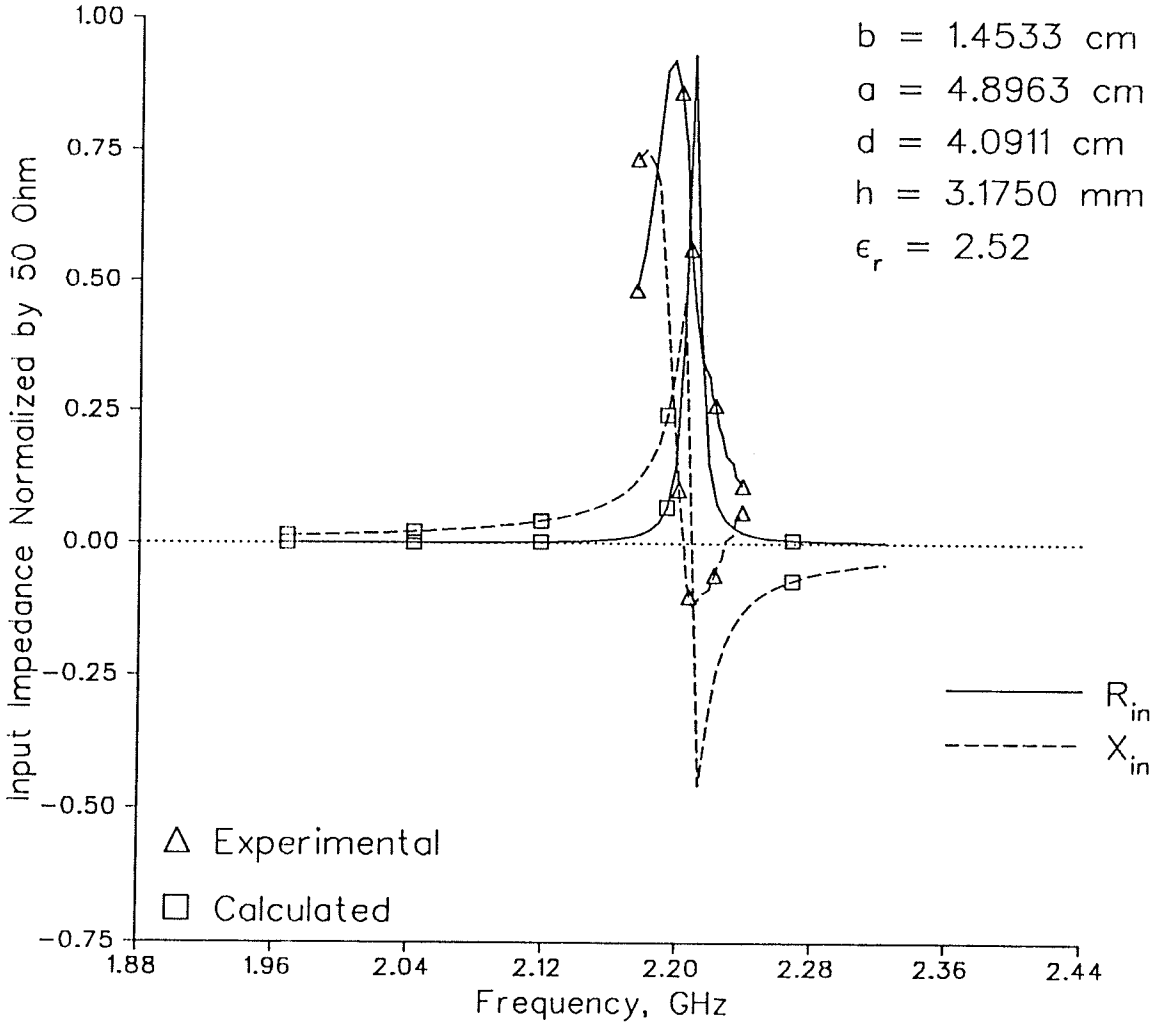

Fig.4.5: Input impedance of the TM_{11} mode for a circular patch with a short at the outside periphery

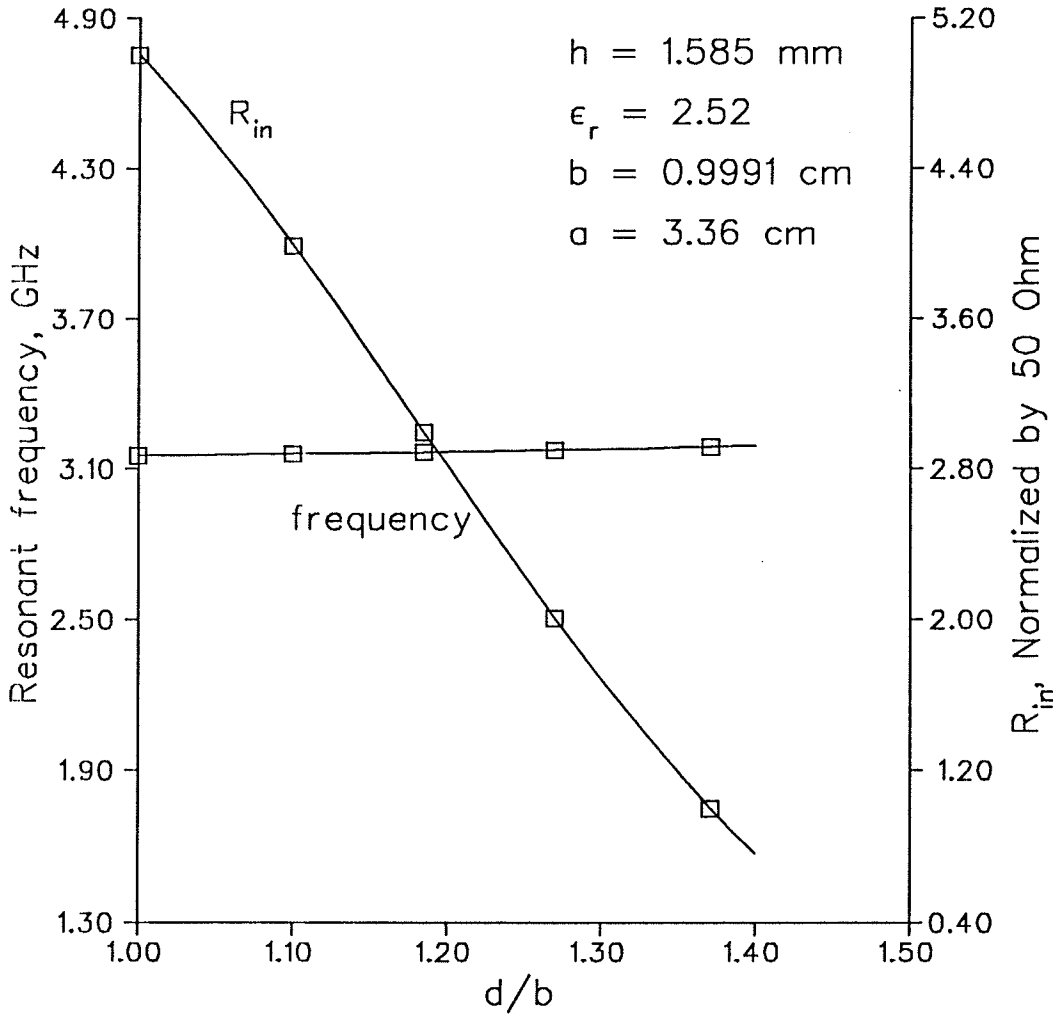

Fig.4.6: Input resistance and frequency at resonance of the TM_{11} mode for an annular ring patches shorted at the outer periphery

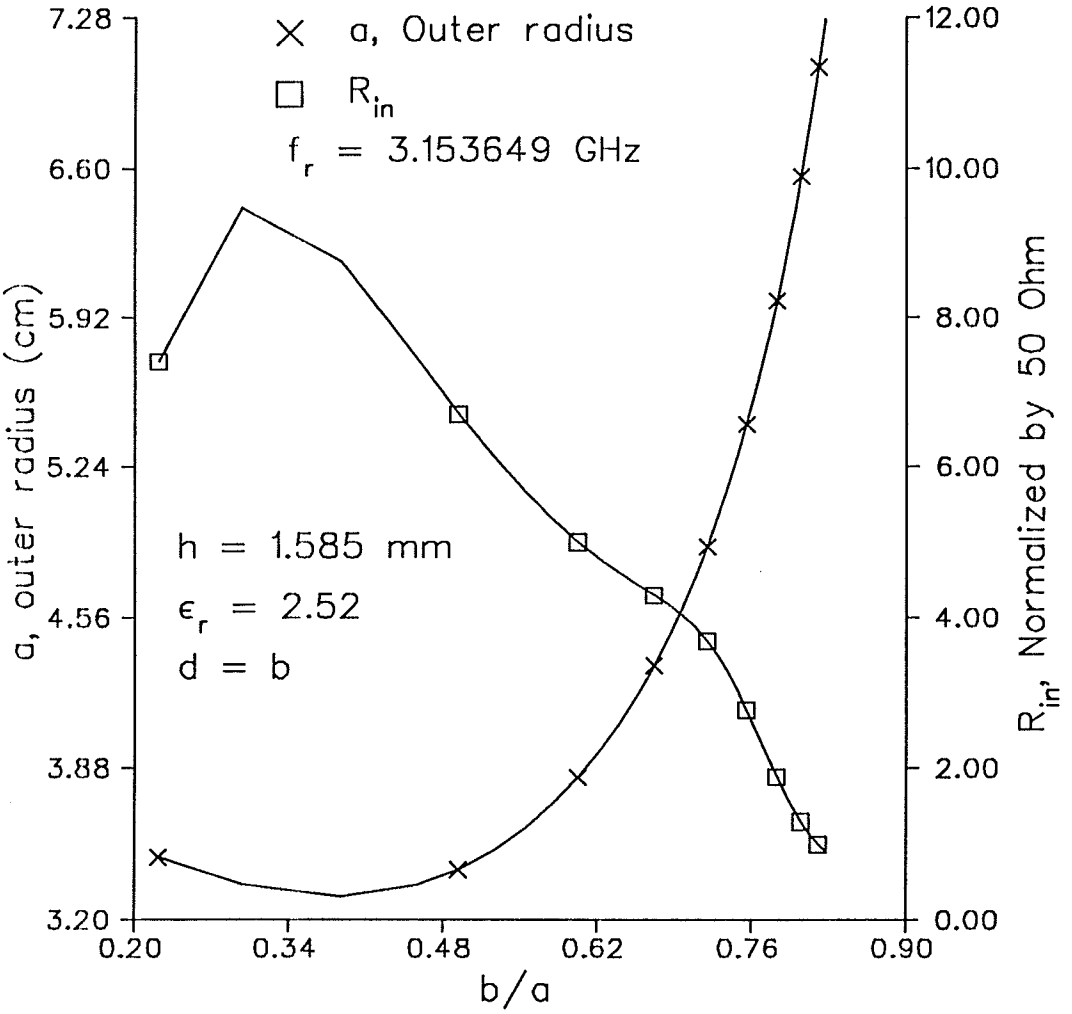

Fig.4.7: Input resistance at resonance and outer radius of the TM_{11} mode for annular ring patches shorted at the outer periphe

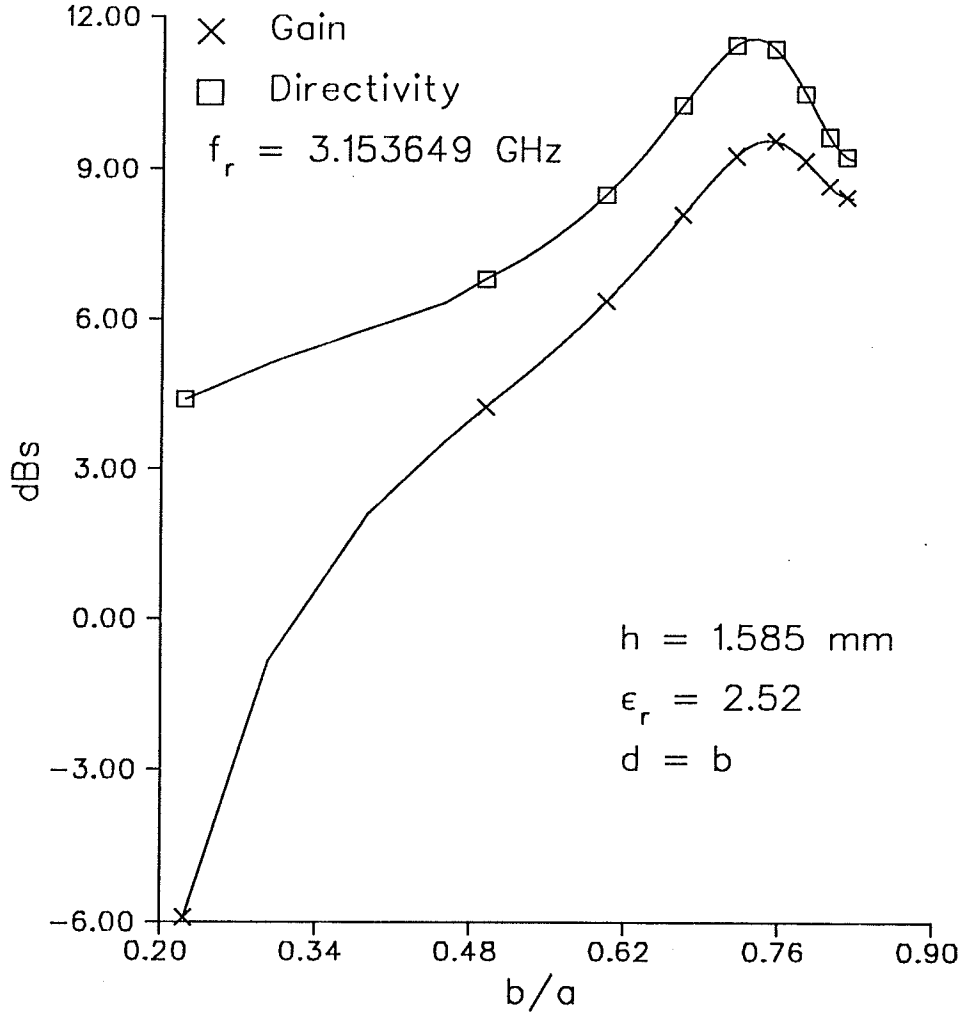

Fig.4.8: Gain and directivity at resonance of the TM_{11} mode for annular ring patches shorted at the outer periphery

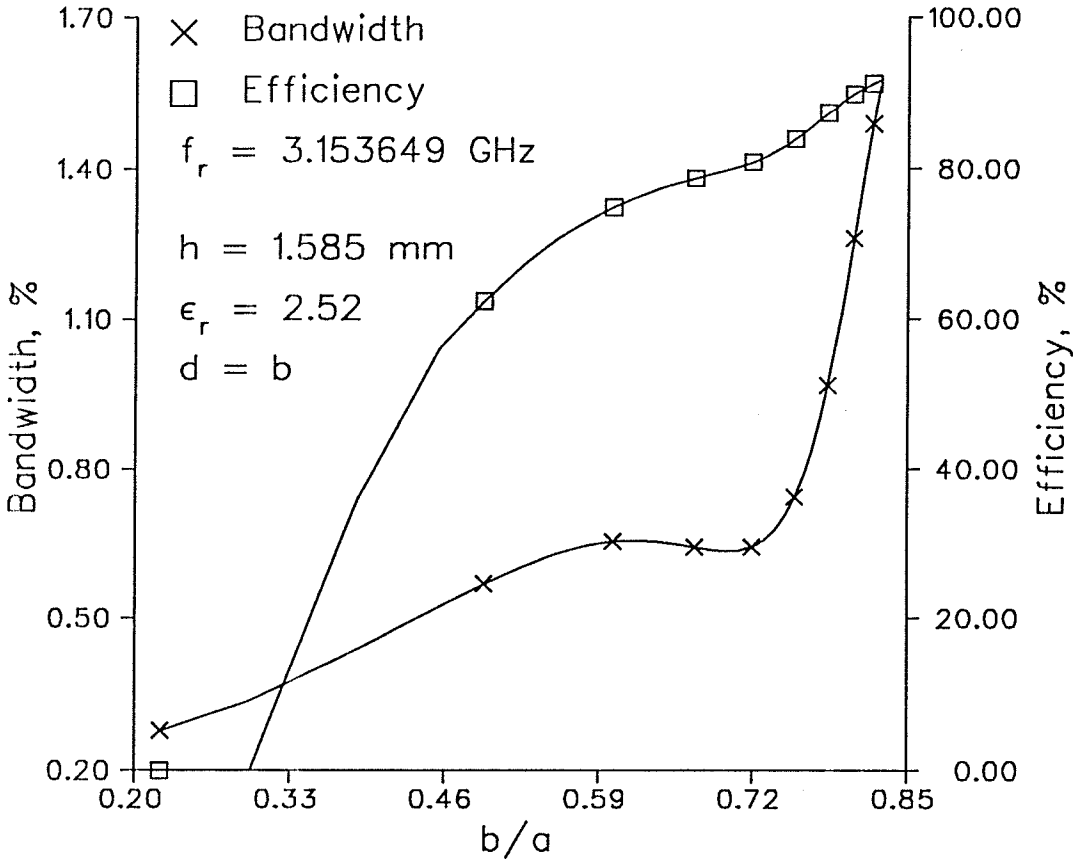

Fig.4.9: Bandwidth and efficiency at resonance of the TM_{11} mode for annular ring patches shorted at the outer periphery

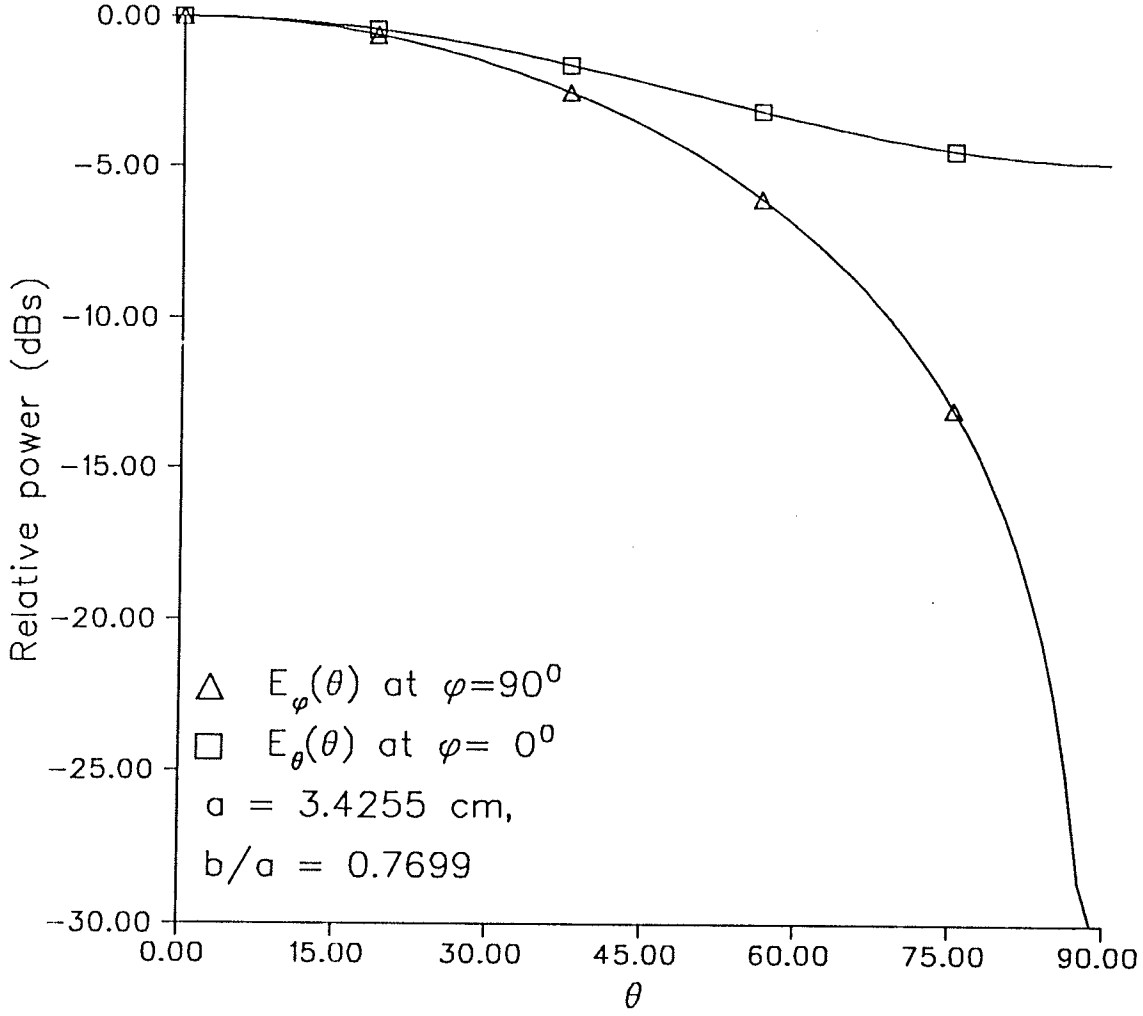

Fig.4.10: Computed radiation patterns of the TM_{11} mode for annular ring shorted at outer periphry at the resonant frequency of 3.153649 GHz

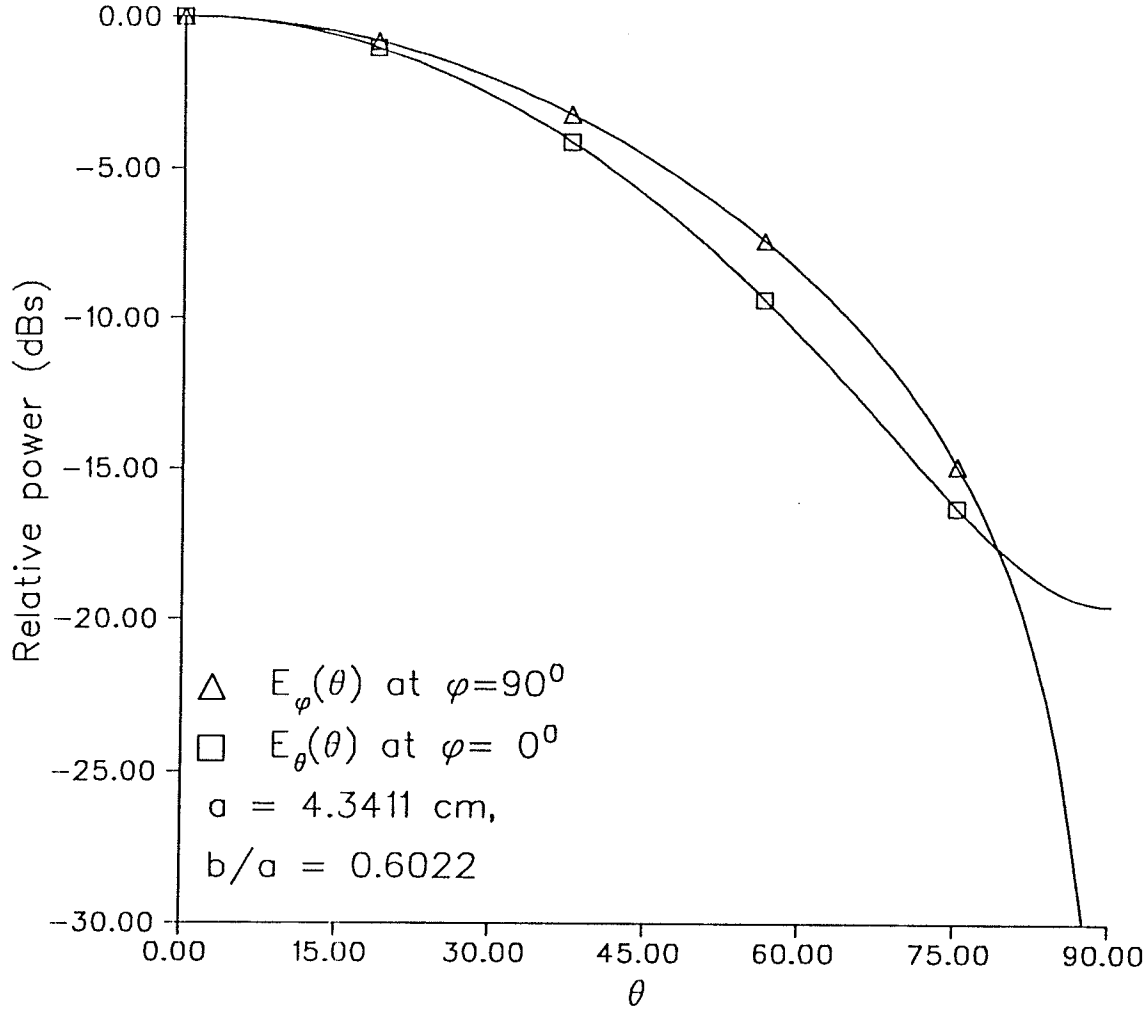

Fig.4.11: Computed radiation patterns of the TM_{11} mode for annular ring shorted at outer periphry at the resonant frequency of 3.153649 GHz

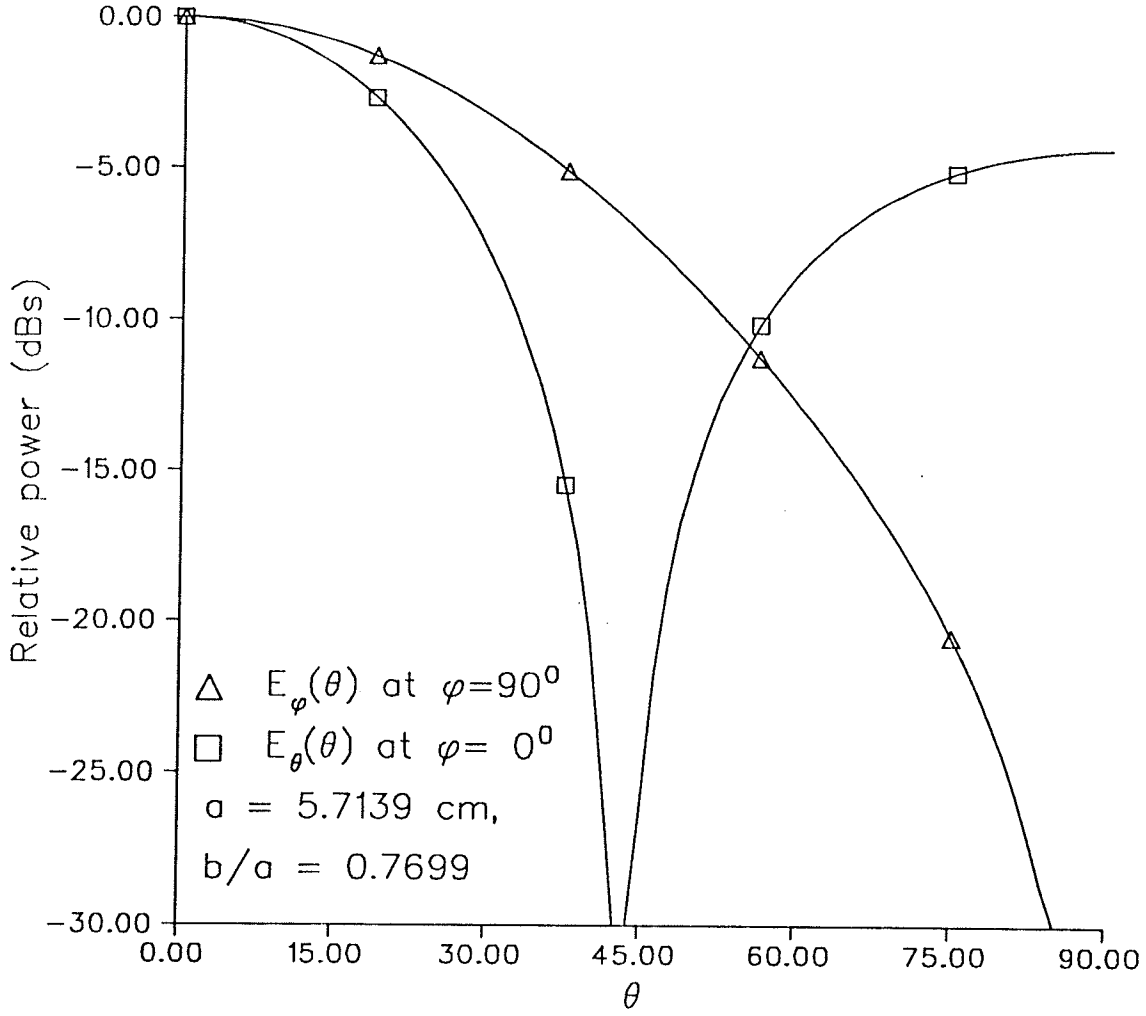

Fig.4.12: Computed radiation patterns of the TM_{11} mode for annular ring shorted at outer periphry at the resonant frequency of 3.153649 GHz

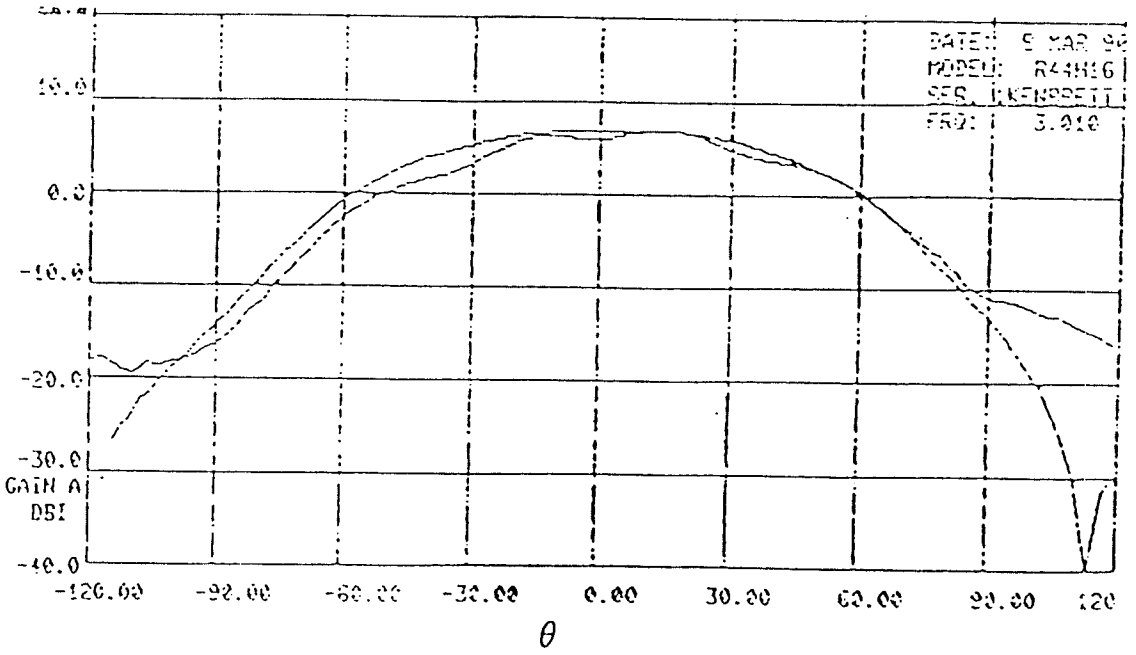

Fig.4.13: Measured radiation patterns of the TM_{11} mode for annular ring shorted at outer periphry at the resonant frequency of 3.053649 GHz

$a = 4.3411$ cm, $b/a = 0.5982$

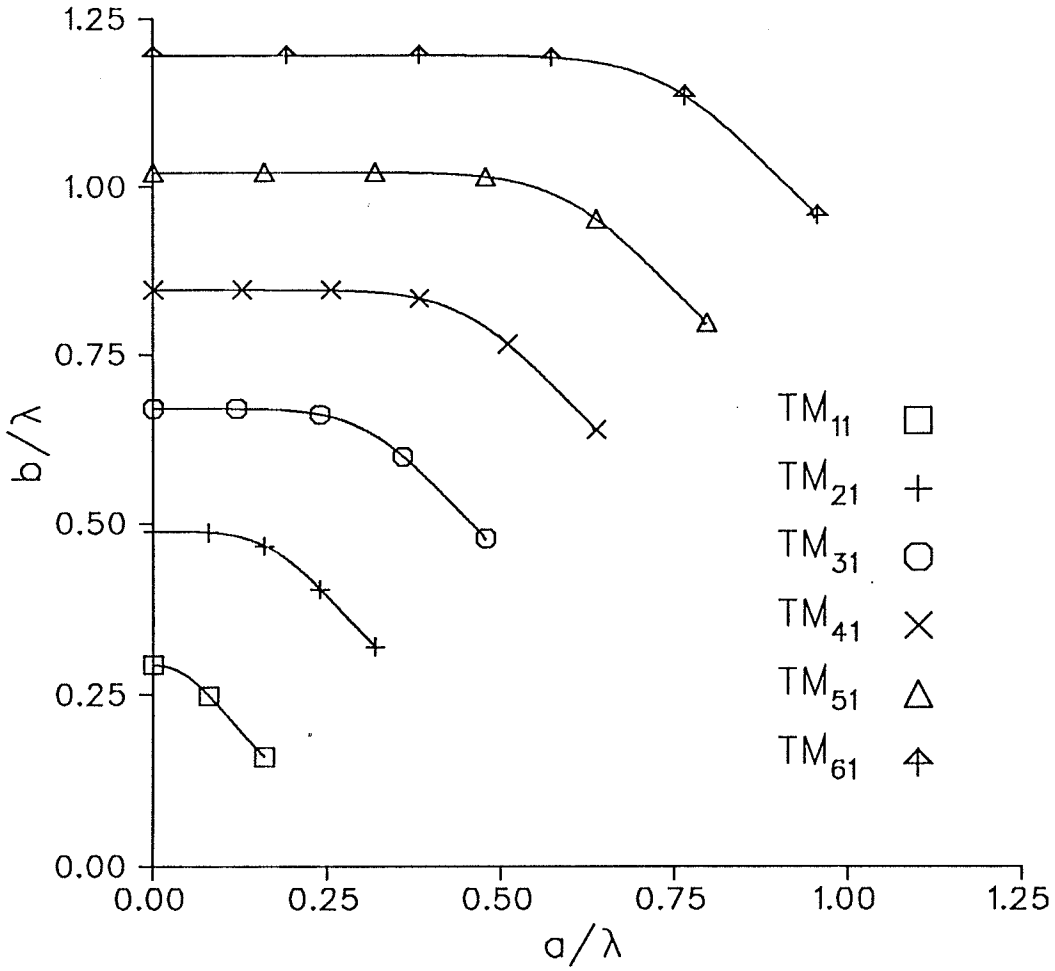

Fig.4.14: Mode chart of annular rings, relationship between the outer and inner radii b and a at resonance of TM_{n1} modes

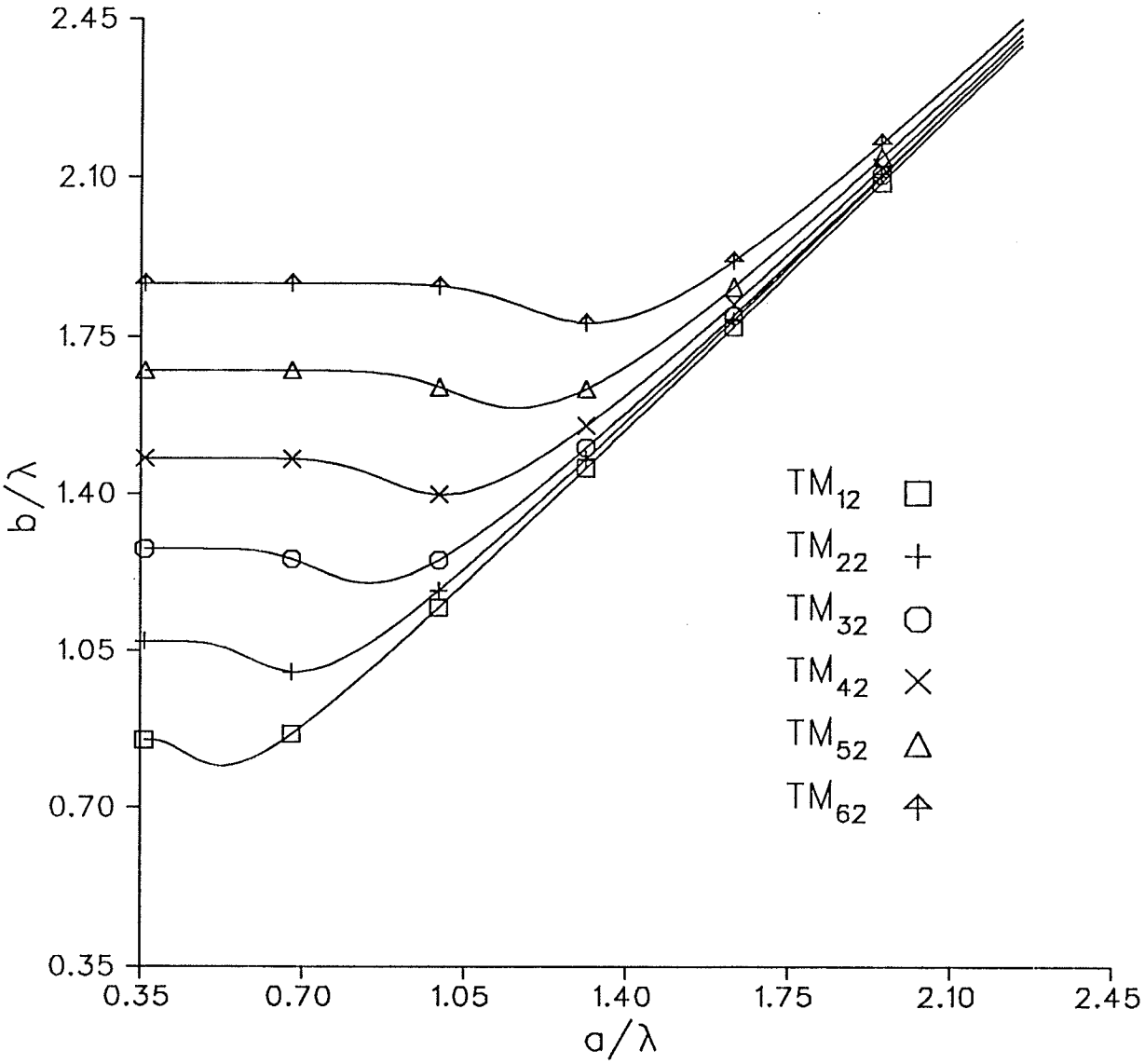

Fig.4.15: Mode chart of annular rings, relationship between the outer and inner radii b and a at resonance of TM_{n2} modes

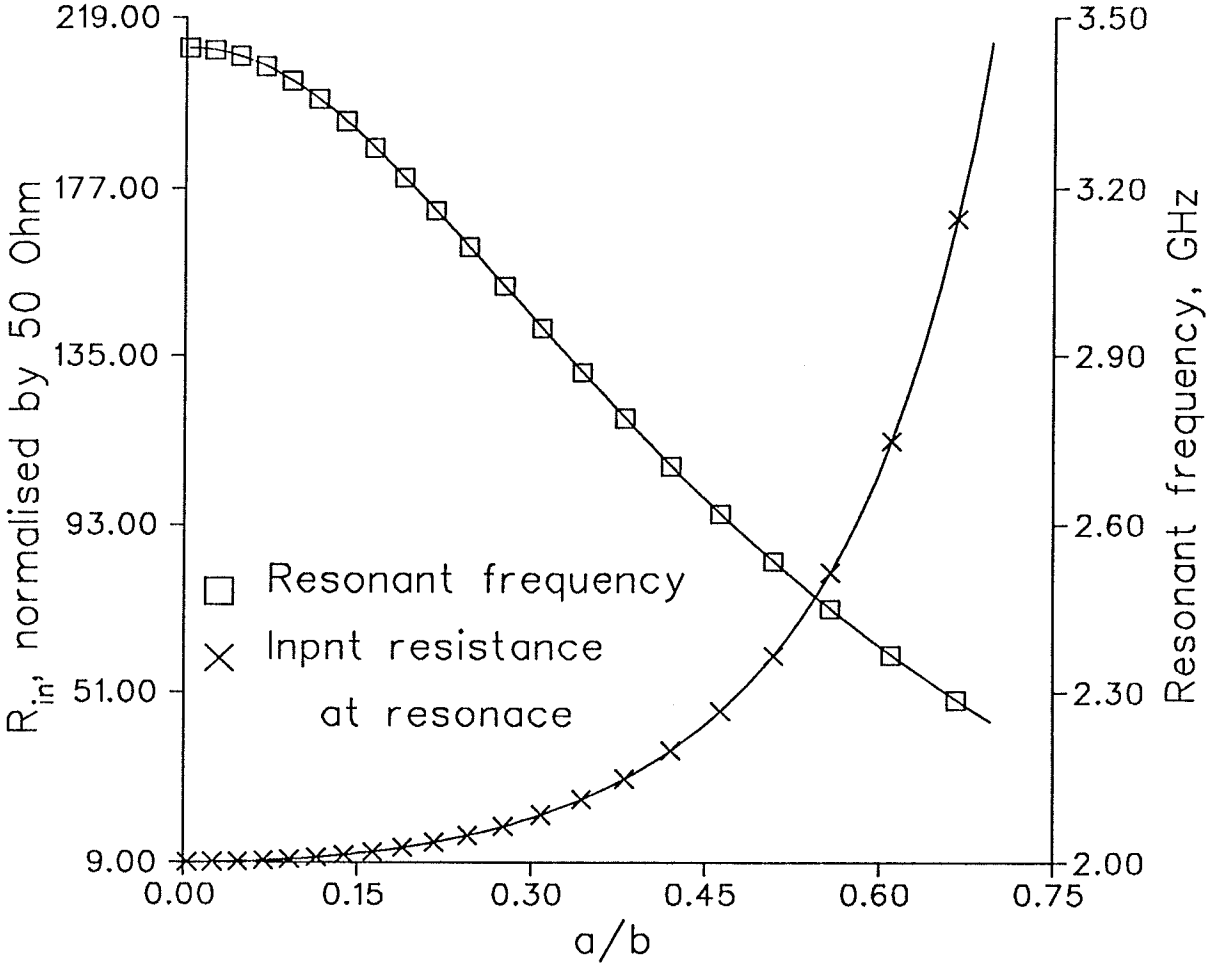

Fig.4.16: Input resistance and frequency at resonance of the TM_{11} mode for annular ring antennas

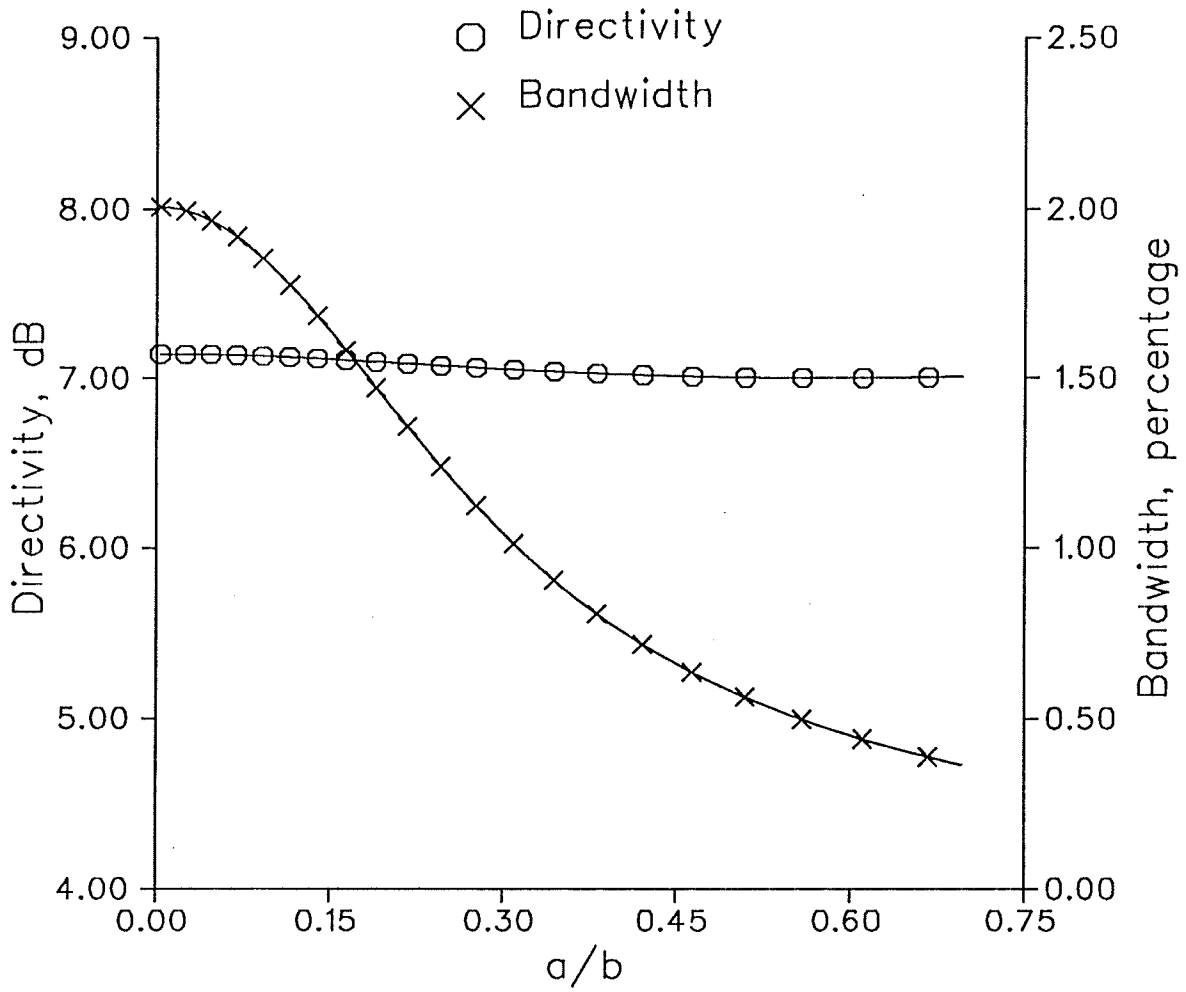

Fig.4.17: Directivity and bandwidth at resonance of the TM_{11} mode for annular ring antennas

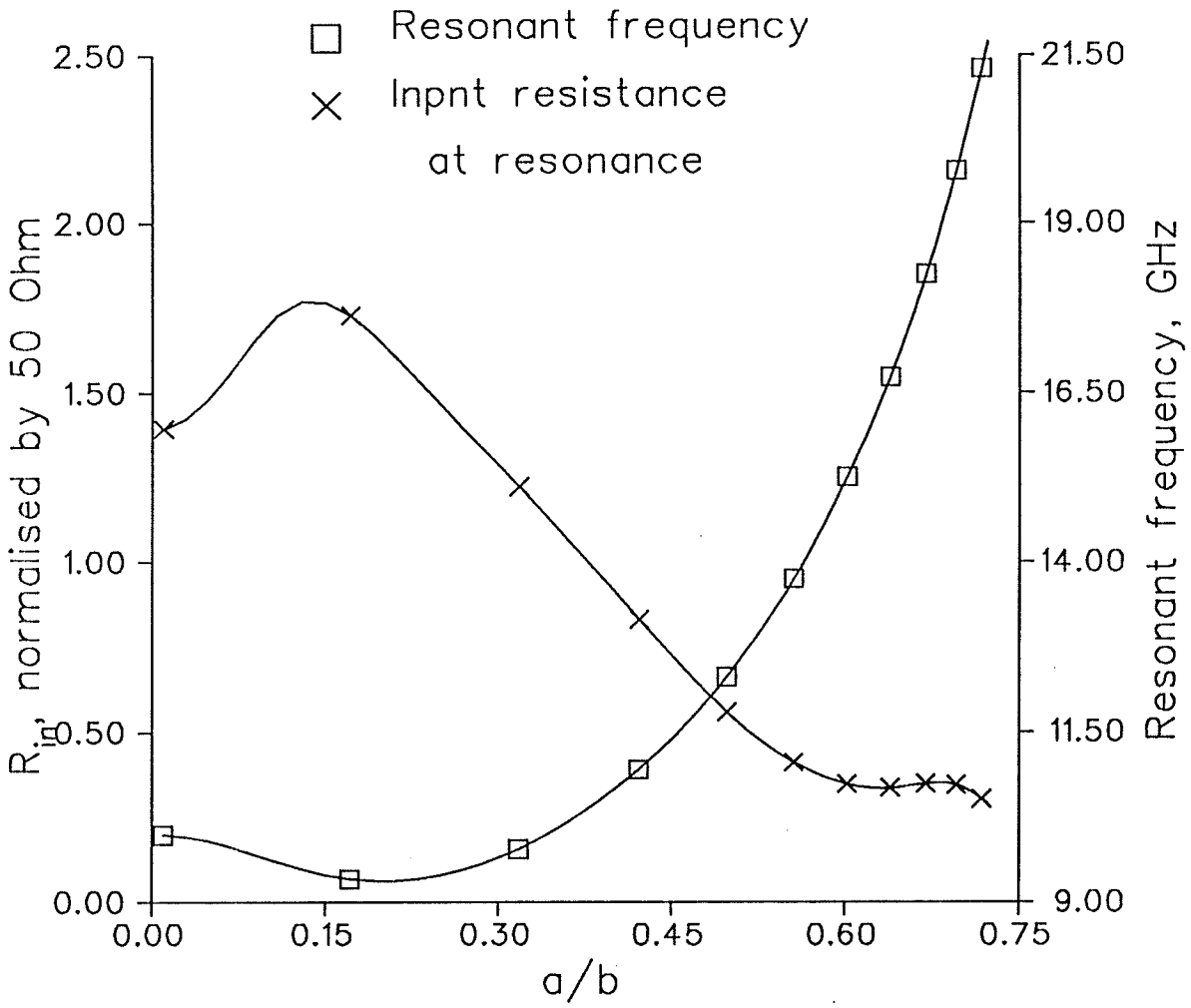

Fig.4.18: input resistance and frequency at resonance of the TM_{12} mode for annular ring antennas

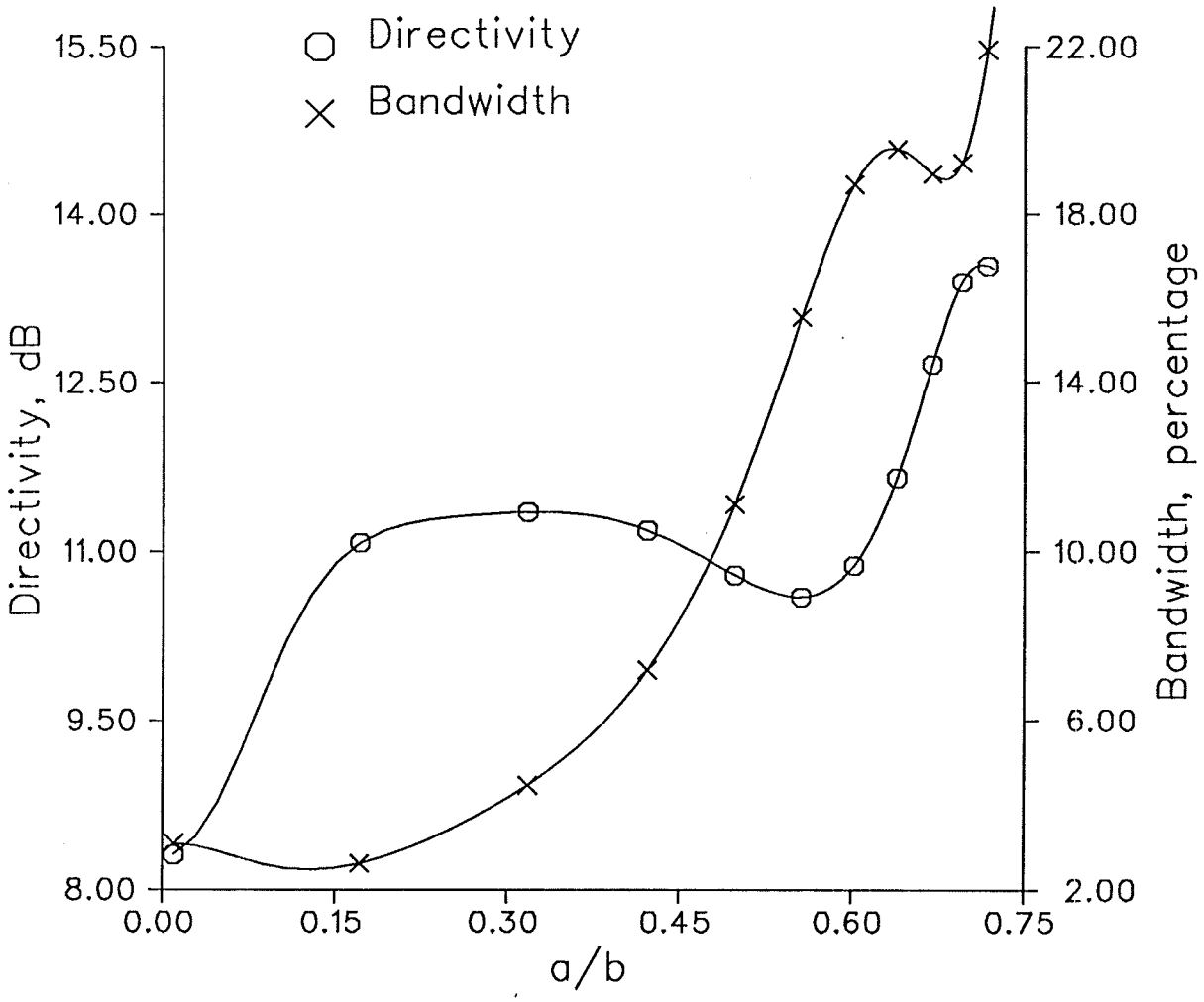

Fig.4.19: Directivity and bandwid at resonance of the TM_{12} mode for annular ring antennas

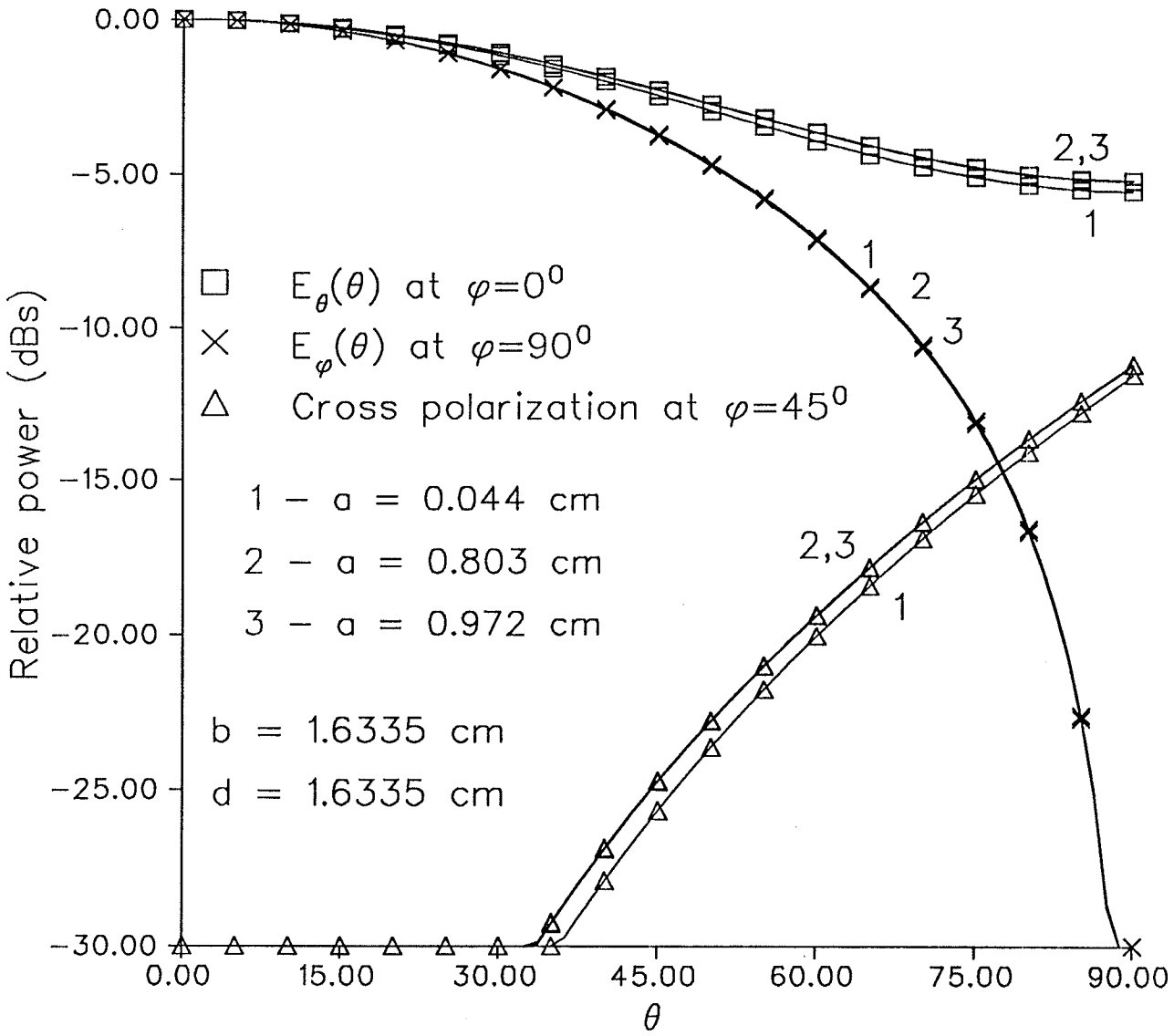

Fig.4.20: Computed radiation patterns for annular ring antennas at resonance of the TM_{11} mode

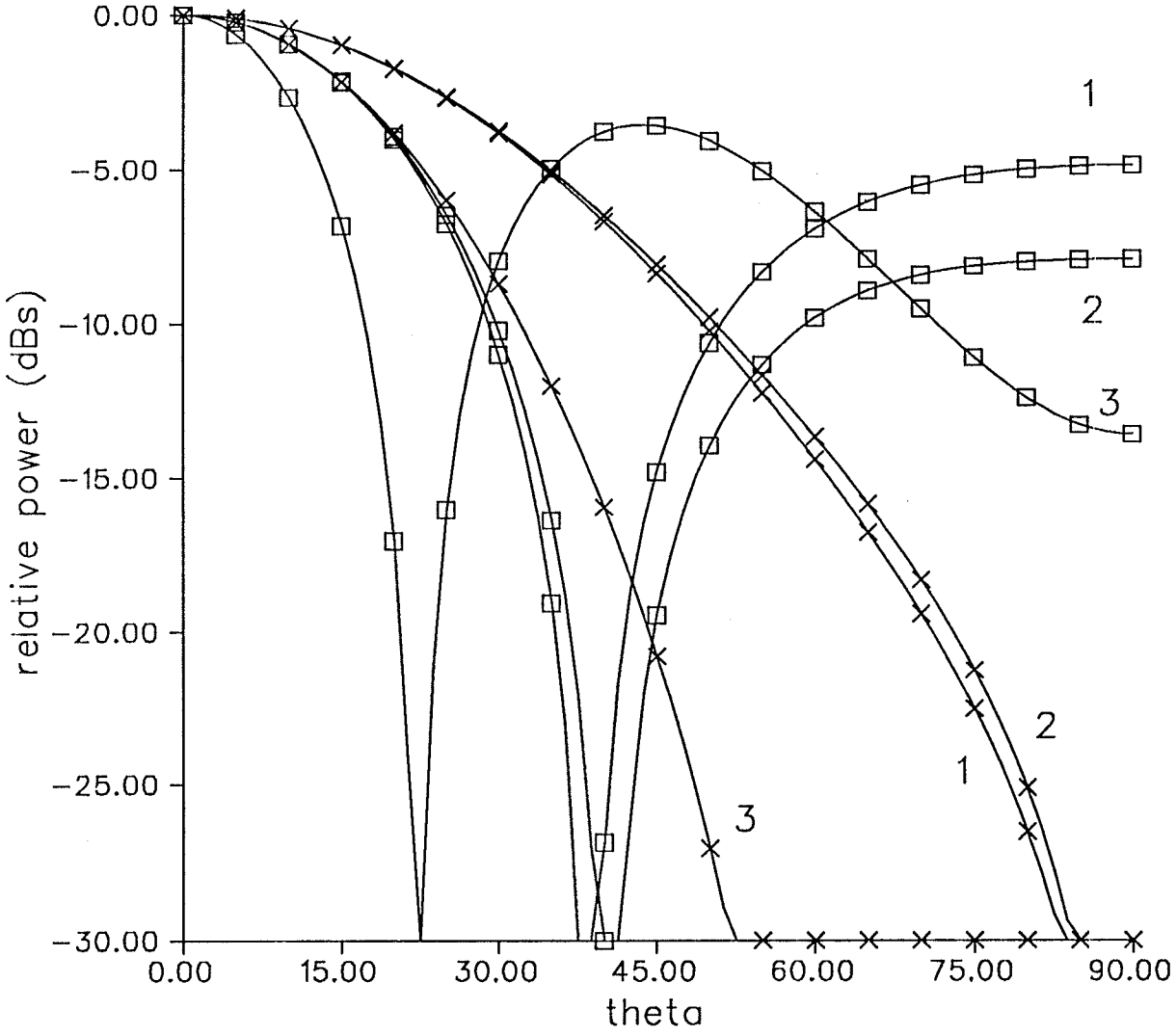

Fig.4.21: Computed radiation patterns for annular ring antennas at resonance of the TM_{12} mode

□ $E_\theta(\theta)$ at $\varphi=0^0$ b = 1.6335 cm

× $E_\varphi(\theta)$ at $\varphi=90^0$ d = 1.6335 cm

1 – a = 0.176 cm

2 – a = 0.669 cm

3 – a = 1.050 cm

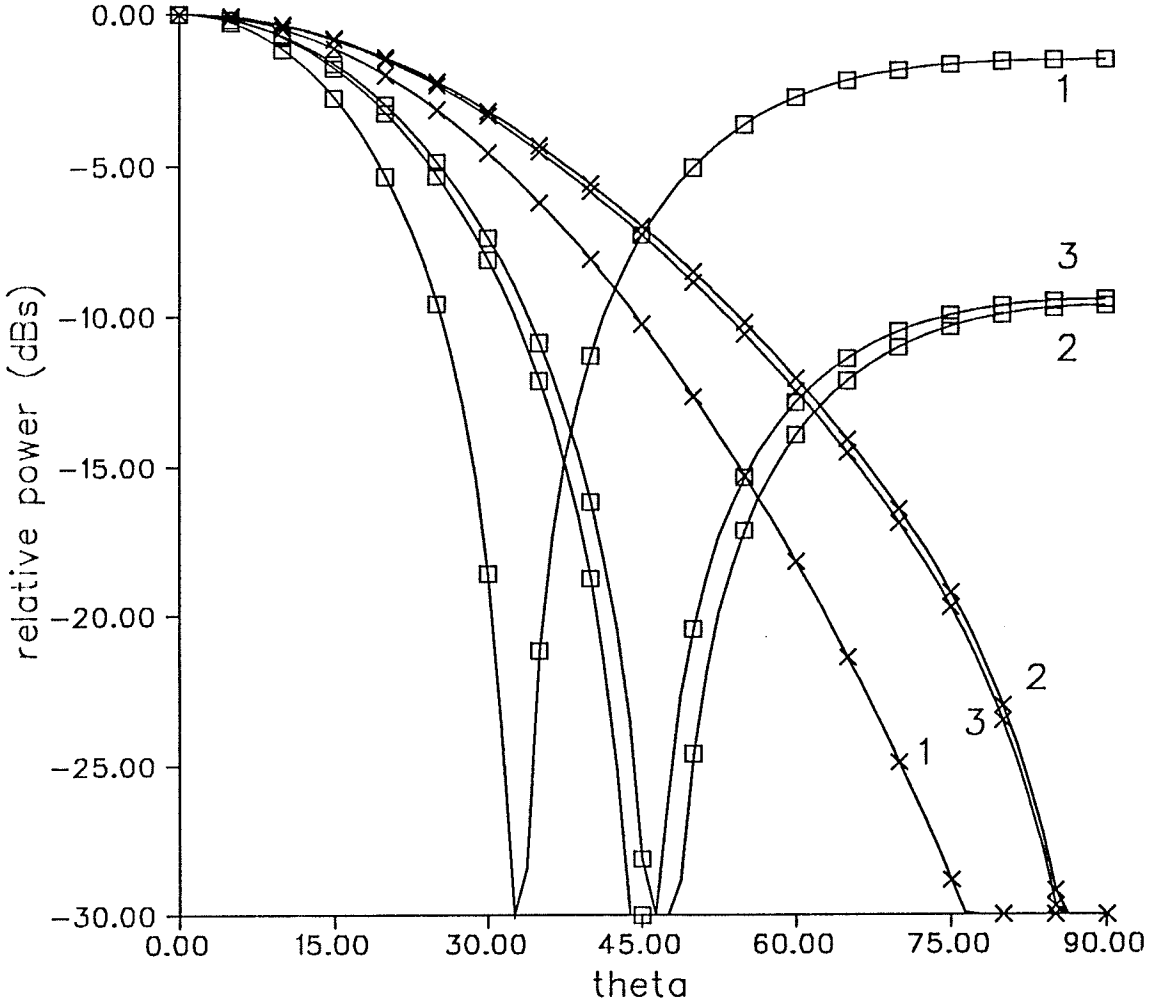

Fig.4.22: Computed radiation patterns of the TM_{12} mode for annular ring antennas at the resonant frequency of 3.7428 GHz

□ $E_\theta(\theta)$ at $\varphi=0^0$ d = b

× $E_\varphi(\theta)$ at $\varphi=90^0$

1. a = 0.040 cm, b = 4.335 cm
2. a = 0.855 cm, b = 4.040 cm
3. a = 1.507 cm, b = 4.347 cm

Chapter 5
Analysis of Biconical Microstrip Antennas

5.1. Introduction

The first practical microstrip antennas were made to conform to the fuselage of aeronautic vehicles. They were long rectangular microstrip patches wrapped around the cylindrical missile body [9] or consisted of several individual rectangular patches mounted on a cylindrical body with a large radius [10]. The analysis of these antennas was based on the fact that the printed conductors, i.e., the radiating elements, were always parallel to the grounded conducting cylinder. When the curvature of the cylinder is much larger than the thickness of the substrate (this is the case in practice), the conformally mounted microstrip antennas can be treated as planar [11]. The results showed that no radiation occurs in the forward direction, which is the vehicle direction of motion (the axis of the cylinder). However, for tracking and aiming systems, the forward looking capability is a basic requirement, and the wraparound type conformal microstrip antennas cannot be utilized for these applications. The thin and low profile antennas can be made conformal to the tip of high speed vehicles, which is usually conical in shape. They may take the shape of biconical or coaxial structures and may radiate in the forward direction. They are no longer a planar configuration and have not been studied previously.

A new type of conformal microstrip antennas is proposed in this chapter. It consists of a conducting cone with a finite cap, the radiating element, electrically driven with respect to a grounded conducting cone, which is infinite in extent. A dielectric

conical layer is infinitely filled between the two cones. When the two cones have nearly the same apex angles, the antenna is of microstrip type, and is named here as biconical microstrip antenna. A special case of biconical microstrip antenna is the conical patch microstrip antenna. That is, when the grounded cone becomes a plane (the angle of the grounded cone is 90^0 with respect to the z-axis) and the antenna geometry becomes planar configuration again. The conical patch microstrip antennas may have superior performances in bandwidth and efficiency [12]. The analysis of this new type of antennas is given in this Chapter.

The analysis begins with the study of the eigenvalues ν of the ϕ dependent spherical wave eigenfunctions in the θ direction for general biconical and coaxial structures [18]. The fields between the cones are then expanded in terms of the series of the existing cavity modes, i.e., the *TE* modes, along with the integer order m and the degree ν. The coefficients of the series are determined by a mode matching method applied at the boundaries containing the feed and the radiating cone. The wall admittance, or impedance, at the aperture links the fields inside and outside the cavity. The study of the wall admittance, or impedance, of the biconical microstrip antenna is presented in Section 4. The near-field and far-field characteristics of the antenna are determined by the obtained fields in the cavity.

5.2. Eigenvalues of Spherical Wave Eigenfunctions

The investigation of biconical and coaxial structures has a long history and originated around the middle of this century. Analytic results for a symmetric feeding or loading of transmitting or receiving antennas (source or load at the origin) have been published in numerous papers and several books [50,51]. The solutions for the zero order ($m = 0$) *TM* modes, including the special case of *TEM* mode ($\nu = 0$), were

well studied in [51]. However, no analysis of these structures with asymmetric sources or loads, which excite the high order modes, has been reported in literature. An investigation of the eigenvalues of the ϕ dependent spherical wave functions for these structures is presented in this section. It is the first step toward analyzing the biconical microstrip antennas.

The eigenvalues of the spherical wave eigenfunctions are the solutions of the characteristic equations set up to satisfy the perfectly conducting conical boundary conditions in the θ direction.

5.2.1. The ϕ Dependent Characteristic Equations

The configuration of biconical and coaxial structures are shown in Fig.5.1. These structures are considered as radial waveguides, since they are capable of supporting waves traveling along the radial direction.

Using the method of separation of variables, the solutions of the Helmholtz equations can be obtained in the spherical coordinate system. By the superposition principle, the fields can be constructed from two parts, one *TM* to r and the other *TE* to r. The magnetic and electric potentials are thus defined as:

$$A_{m\nu_i} = R_{\nu_i}(kr)\,[\,P^m_{\nu_i}(\cos\theta)\,Q^m_{\nu_i}(\cos\theta_2) - P^m_{\nu_i}(\cos\theta_2)\,Q^m_{\nu_i}(\cos\theta)\,]e^{jm\phi} \qquad (5.1)$$

$$F_{m\nu_i} = R_{\nu_i}(kr)\,[\,P^m_{\nu_i}(\cos\theta)\frac{dQ^m_{\nu_i}(\cos\theta_2)}{d\theta} - Q^m_{\nu_i}(\cos\theta)\frac{dP^m_{\nu_i}(\cos\theta_2)}{d\theta}]e^{jm\phi} \qquad (5.2)$$

for the *TM* and *TE* modes, respectively, where P and Q are the first and second kinds of associated Legendre functions, $m = 0,1,2,...$ and R_{ν_i} represents the solution of the separated radial equation which is a linear combination of the spherical Bessel functions and satisfies the boundary conditions [52].

By imposing the boundary conditions, i.e., the tangential components of the electric fields that vanish on the perfectly conducting cones ($\theta=\theta_1$ and $\theta=\theta_2$), the characteristic equations for the modes *TM* and *TE* to the radial direction become

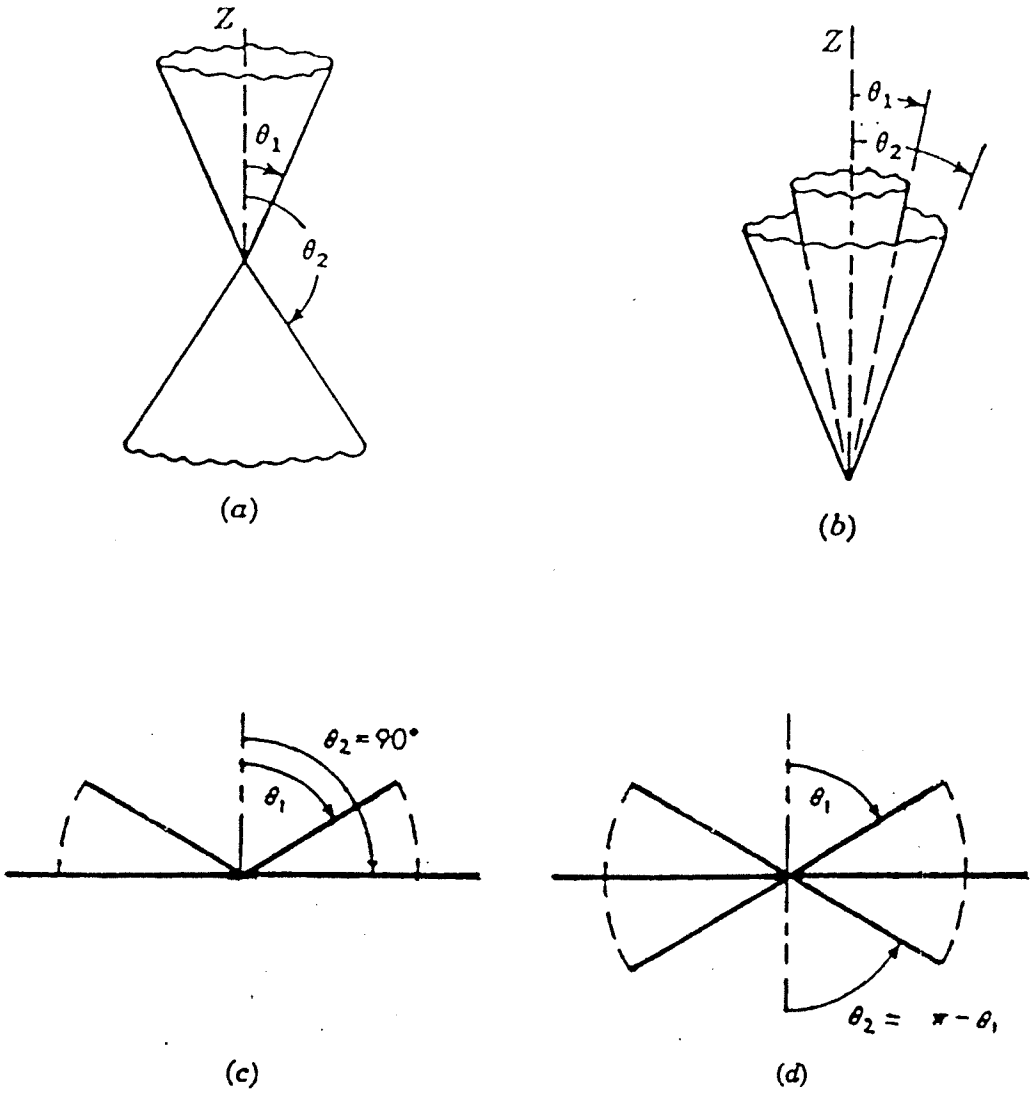

Fig.5.1 The biconical and coaxial structures

(a). Biconical

(b). Coaxial

(c). The mirror image symmetric structure ($\theta_2 = \pi - \theta_1$)

(d). The symmetric structure ($\theta_2 = 90^0$)

$$P_\nu^m(\cos\theta_1)Q_\nu^m(\cos\theta_2)-P_\nu^m(\cos\theta_2)Q_\nu^m(\cos\theta_1)=0 \tag{5.3}$$

and

$$\left[\frac{dP_\nu^m(\cos\theta)}{d\theta}\right]_{\theta=\theta_1}\left[\frac{dQ_\nu^m(\cos\theta)}{d\theta}\right]_{\theta=\theta_2}-\left[\frac{dP_\nu^m(\cos\theta)}{d\theta}\right]_{\theta=\theta_2}\left[\frac{dQ_\nu^m(\cos\theta)}{d\theta}\right]_{\theta=\theta_1}=0 \tag{5.4}$$

respectively [51].

5.2.2. Computation of the Eigenvalues ν

The solutions for equations 5.3 and 5.4 are obtained by computing accurately the integer order associated Legendre functions and their derivatives with positive real argument and degree, using the following trigonometric summations [53]

$$P_\nu^\mu(\cos\theta)=\pi^{-\frac{1}{2}}2^{\mu+1}(\sin\theta)^\mu\frac{\Gamma(\mu+\nu+1)}{\Gamma(\nu+\frac{3}{2})}\sum_{k=0}^{\infty}\frac{(\mu+1)_k(\nu+\mu+1)_k}{K!(\nu+\frac{3}{2})_k}\sin[(\nu+\mu+2k+1)\theta] \tag{5.5}$$

and

$$Q_\nu^\mu(\cos\theta)=\pi^{\frac{1}{2}}2^{\mu}(\sin\theta)^\mu\frac{\Gamma(\mu+\nu+1)}{\Gamma(\nu+\frac{3}{2})}\sum_{k=0}^{\infty}\frac{(\mu+1)_k(\nu+\mu+1)_k}{K!(\nu+\frac{3}{2})_k}\cos[(\nu+\mu+2k+1)\theta] \tag{5.6}$$

where $0<\theta<\pi$ and μ and ν are real.

Since the real trigonometric functions oscillate between -1 and 1 as the argument increases to infinity, the summation converges if and only if μ is less than 1/2. For this reason, initially, the associated Legendre functions of negative order $-m$ are calculated and then using the identities [54]

$$P_\nu^m(x)=(-1)^m\frac{\Gamma(\nu+1+m)}{\Gamma(\nu+1-m)}P_\nu^{-m}(x) \tag{5.7}$$

$$Q_\nu^m(x)=(-1)^m\frac{\Gamma(\nu+1+m)}{\Gamma(\nu+1-m)}Q_\nu^{-m}(x) \tag{5.8}$$

the associated Legendre functions of positive order are calculated.

Based on eqns 5.5-5.8, a numerical subroutine is developed for the calculation of associated Legendre functions and their derivatives of real argument with real degree and order. By calling the subroutine ZREAL from IMSL (International Mathematical and Statistics Library), the Muller's method is used to solve eqns 5.3 and 5.4. Their roots, that is, the degree ν's, that lead the characteristic equations 5.3 and 5.4 to become zero, are the eigenvalues of the corresponding eigenfunctions.

Since no mathematical and physical approximations are made, the eigenvalues found here are accurate, as long as the values of the associated Legendre functions and their derivatives are adequately accurate. Unfortunately, no analytical and numerical data on associated Legendre functions with real degree are found in published literature. We have compared our calculated data for special cases, such as $\theta=\pi/2$ (argument $x=\cos\theta=0$), with those calculated from existing exact and analytic expressions for different values of m and ν . They show good agreement. For $m=1$, their agreement is within eight significant figures and as m increases, the agreement improves to 12 significant figures.

5.2.3. Results and Discussion

For the *TM* modes, it is evident that all integer values of ν 's less than m satisfy eqn.5.3, since both P_n^m and Q_n^m vanish when $n<m$ [53]. Numerical calculations show neither fractional roots nor integer roots equal to or larger than m for eqn.5.3. Thus, all solutions for the nonzero order TM modes are trivial and the *TM* modes other than the zero order modes do not propagate in the structure.

For the *TE* modes, eigenvalues are shown in Table 5.1 and Figs 5.2-5.4. A numerical search indicates that for each integer value of m, there is a unique nontrivial root of eqn.5.4. Again, the integer eigenvalues less than m are trivial solutions. Table 5.1 depicts that for a mirror image symmetric biconical structure shown in Fig.5.1c, with $\Delta\theta=6^0$, a finite number of eigenvalues exists, of which only the fractional ones (less than m and larger than $m-1/2$) are nontrivial solutions. Fig.5.2 illustrates that

eigenvalues change slowly and approach the order m, as θ_1 approaches zero. They are almost constant for $80^0<\theta_1<90^0$. This means that for very narrow angle mirror image symmetric biconical structures, the field inside the structure is almost independent of θ. The eigenvalues shown above are valid for the symmetric biconical antennas ($\theta_2=\pi-\theta_1$).

m \ ν_i \ i	1	2	3	4
1	.61967	0	0	0
2	1.5651	1	0	0
3	2.5468	2	1	0
4	3.5384	3	2	1

Table 5.1: Eigenvalues ν for *TE* modes with $\Delta\theta=6^0$ and $\theta_2=90^0$

Figs 5.3 and 4 show that for the asymmetric geometry with a constant narrow angle between the cones ($\Delta\theta=6^0$), the nontrivial eigenvalues of the *TE* modes change rapidly. In Fig.5.3, they decrease from infinity to a value between $m-1/2$ and m as θ_2 increases from 0 to $\pi/2$. Fig.5.4 shows that they increase from the above indicated value to infinity as θ_2 increases from $\pi/2$ to π.

5.3. Modal Field Expressions

The geometry of the biconical microstrip antenna is shown in Fig.5.5. Since it is of microstrip type, the angle between the two conducting cones, $\Delta\theta$, is very small, such that $b\Delta\theta\ll\lambda$, i.e, $k_1 b\Delta\theta\ll 1$, where $k_1=\omega\sqrt{\mu\varepsilon_1}$, ω being the angular frequency. The antenna can be modeled as a biconical cavity. It consists of an admittance wall at the spherical sector, $r = b$ and $\theta_1\leq\theta\leq\theta_2$, and electric walls at two conducting cones,

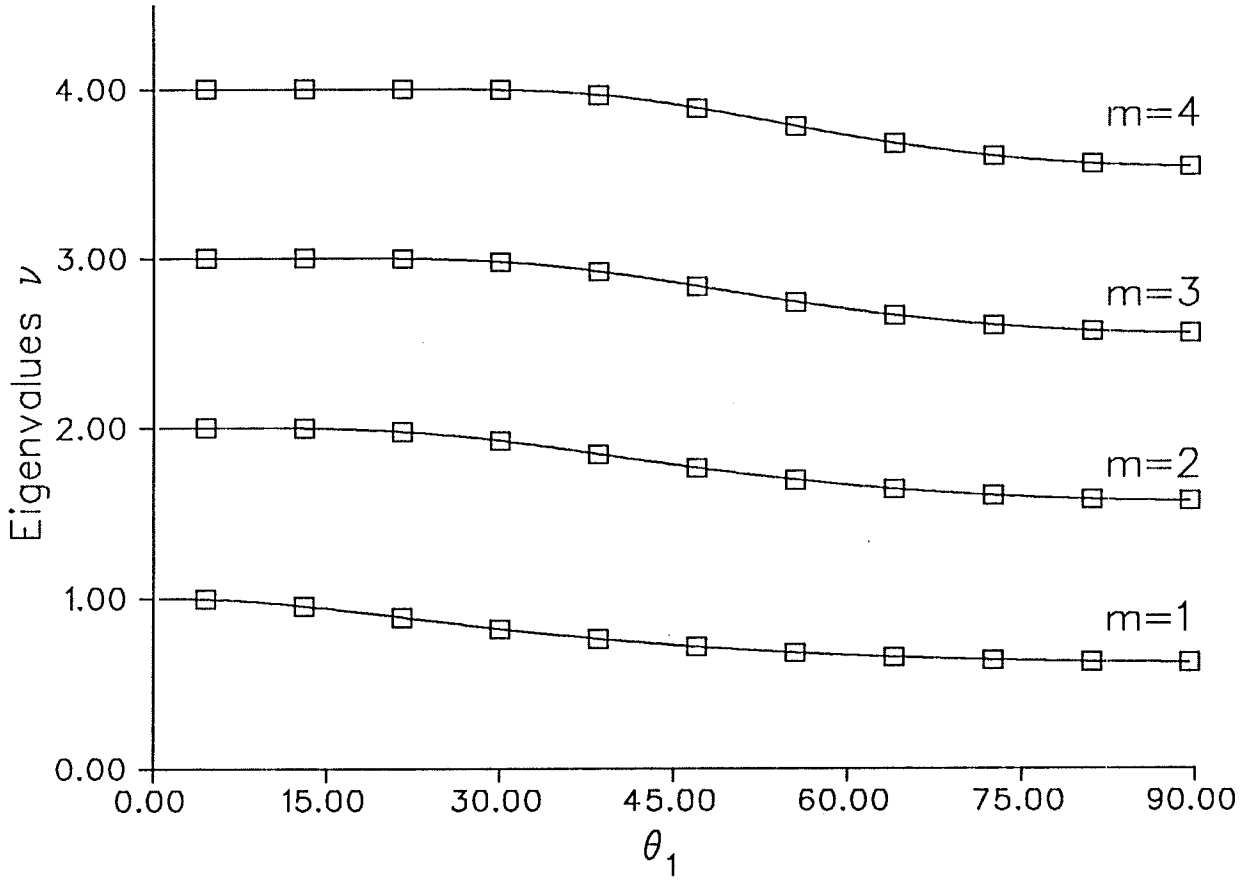

Fig.5.2: Eigenvalues v.s. θ_1 for the symmetric and mirror image symmetric biconical structures of Fig.5.1c

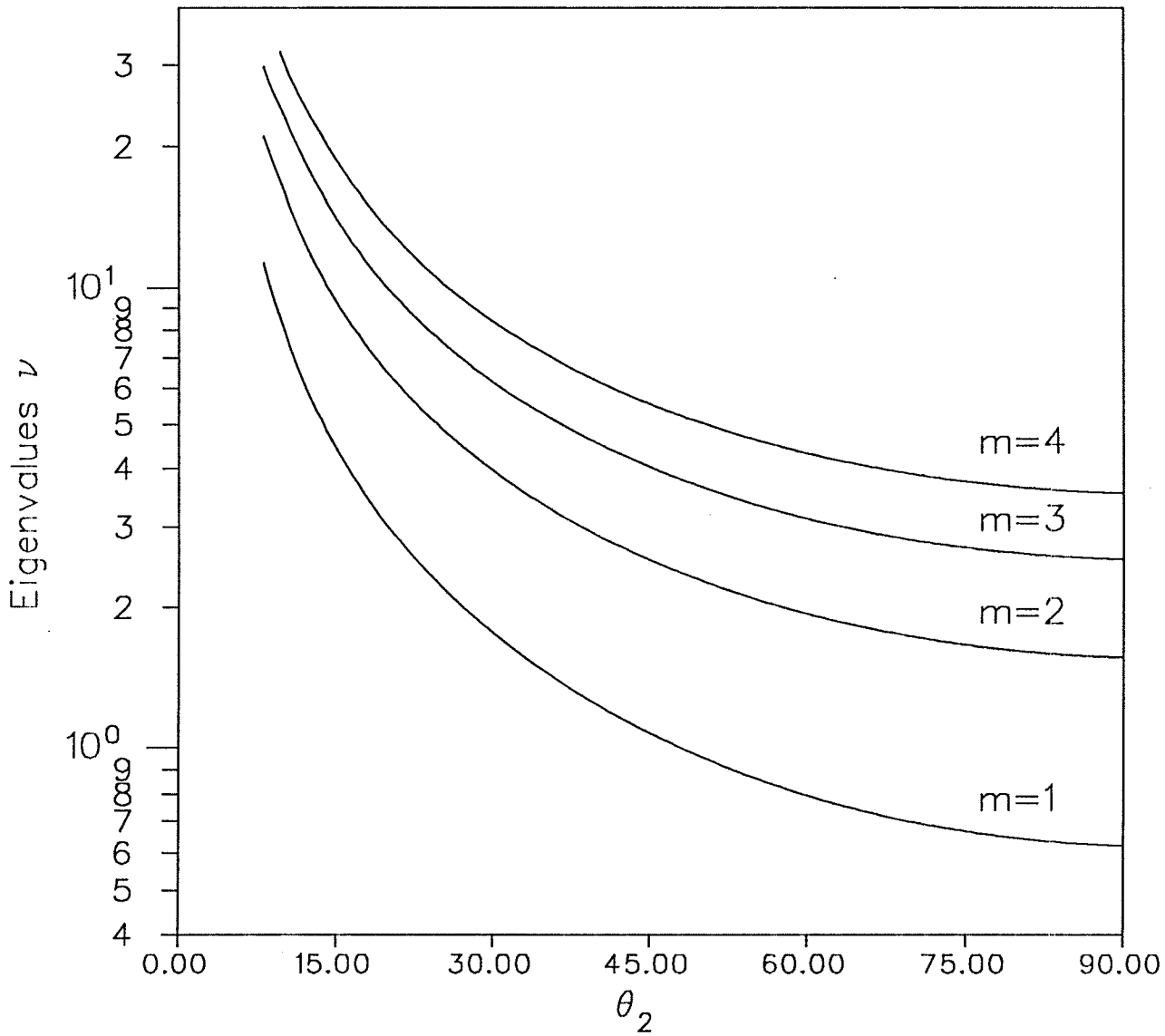

Fig.5.3: eigenvalues v.s. θ_2, where $\Delta\theta = 6^0$ for geometry of Fig.5.1b, $\theta_2 < 90^0$

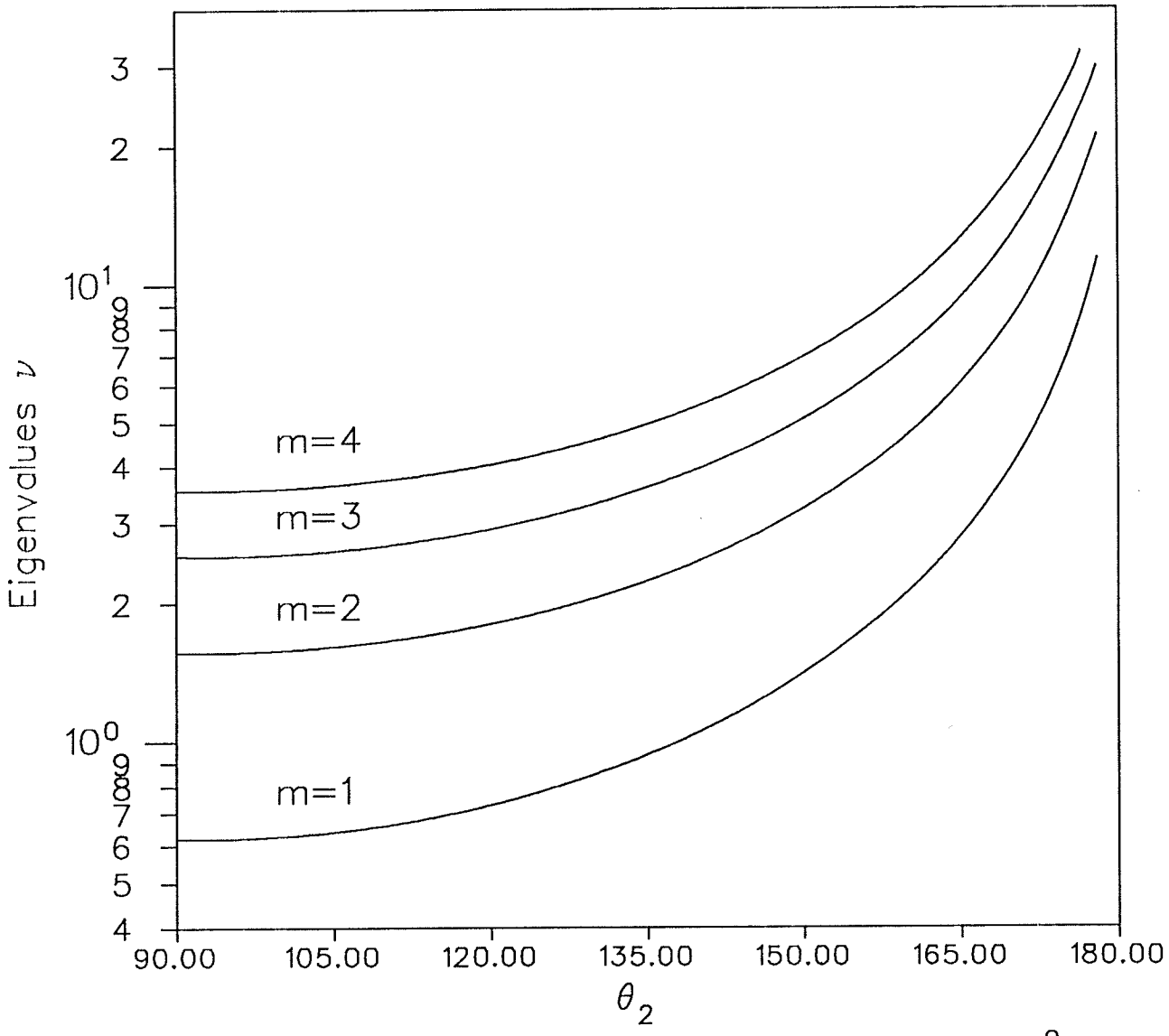

Fig.5.4: eigenvalues v.s. θ_2, where $\Delta\theta = 6^0$ for geometry of Fig.5.1b, $\theta_2 > 90^0$

$\theta = \theta_1$ and θ_2. The electromagnetic field excitation is due to a current I_0 along the θ direction and through the center conductor of a coaxial cable at $r = d$. The current source can therefore be expressed as

$$\mathbf{J} = \hat{\mathbf{u}}_\theta \, I_0 \, \frac{\delta(r - d)}{r^2 \sin\theta} \, \delta(\phi) \tag{5.9}$$

According to the results shown in the previous section, only the modes *TE* to the radial direction can be excited within the cavity. None of the *TM* modes is excited. Thus, only the electric potential F_r (given by eqn.5.2) exists and the magnetic potential A_r vanishes.

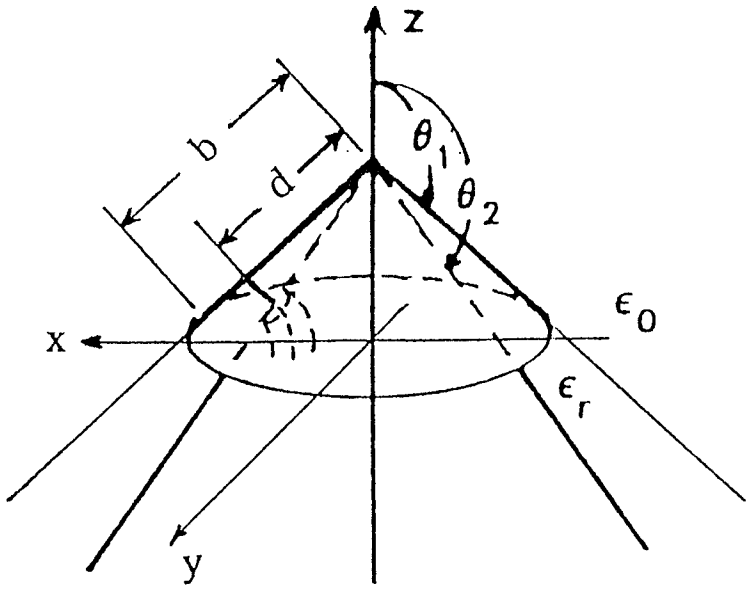

Fig.5.5: The geometry of the biconical microstrip antenna

In terms of [50]

$$\mathbf{F} = \hat{\mathbf{u}}_r \, F_r \, , \tag{5.10}$$

the electromagnetic fields inside the cavity are expanded as the following equations

$$E_\theta = \sum_{m=0}^{\infty} \sum_{i=1}^{\infty} \sum_{p=1}^{\infty} \frac{-jm}{r \sin\theta} R_{m\nu_i}(k_{1p} r) \, T_{\nu_i}^m(\cos\theta) \, e^{jm\phi} \tag{5.11}$$

$$E_\phi = \sum_{m=0}^{\infty}\sum_{i=1}^{\infty}\sum_{p=1}^{\infty}\frac{1}{r}R_{m\nu_i}(k_{1p}r)\,\frac{dT_{\nu_i}^m(\cos\theta)}{d\theta}\,e^{jm\phi} \tag{5.12}$$

$$H_r = \sum_{m=0}^{\infty}\sum_{i=1}^{\infty}\sum_{p=1}^{\infty}\frac{\nu_i(\nu_i+1)}{j\omega\mu\, r^2}R_{m\nu_i}(k_{1p}r)\,T_{\nu_i}^m(\cos\theta)\,e^{jm\phi} \tag{5.13}$$

$$H_\theta = \sum_{m=0}^{\infty}\sum_{i=1}^{\infty}\sum_{p=1}^{\infty}\frac{k_{1p}}{j\omega\mu\, r}R'_{m\nu_i}(k_{1p}r)\,\frac{dT_{\nu_i}^m(\cos\theta)}{d\theta}\,e^{jm\phi} \tag{5.14}$$

$$H_\phi = \sum_{m=0}^{\infty}\sum_{i=1}^{\infty}\sum_{p=1}^{\infty}\frac{mk_{1p}}{\omega\mu\, r\,\sin\theta}R'_{m\nu_i}(k_{1p}r)\,T_{\nu_i}^m(\cos\theta)\,e^{jm\phi} \tag{5.15}$$

where $T_{\nu_i}^m$ is the θ dependence function given in eqn.5.2,

$$R_{m\nu_i} = R_{1m\nu_i} = A_{m\nu_i}\tilde{J}_{\nu_i}(k_{1p}r) \qquad 0<r<d \tag{5.16}$$

$$R_{m\nu_i} = R_{2m\nu_i} = C_{m\nu_i}\tilde{J}_{\nu_i}(k_{1p}r)+D_{m\nu_i}\tilde{Y}_{\nu_i}(k_{1p}r) \qquad d<r<b \tag{5.17}$$

and $\tilde{J}_{\nu_i}(k_{1p}r) = k_{1p}r\; j_{\nu_i}(k_{1p})$ and $\tilde{Y}_{\nu_i}(k_{1p}r) = k_{1p}\; y_{\nu_i}(k_{1p}r)$ are the first and second kinds spherical Bessel functions, and the prime denotes the derivatives with respect to the argument. $A_{m\nu_i}$, $C_{m\nu_i}$ and $D_{m\nu_i}$ are complex constants to be determined. The time factor $e^{j\omega t}$ is assumed and suppressed throughout the analysis.

The following boundary conditions are imposed

$$H_{\phi m} = -y_{sm}E_{\theta m} \qquad (at\;\; r = b) \tag{5.18}$$

$$E_{\theta m1} = E_{\theta m2} \quad or \quad H_{rm1} = H_{rm2} \qquad (at\;\; r = d) \tag{5.19}$$

$$H_{\phi m1} - H_{\phi m2} = I_0\,\frac{\delta(r-d)}{d^2\sin\theta}\,\delta(\phi) \qquad (at\;\; r = d) \tag{5.20}$$

where $y_{sn}=g_{sn}+jb_{sn}$ is the wall admittance. There is an additional boundary condition at the spherical surface of the assumed cavity with a magnetic wall at $r=b_e$

$$H_\phi = 0 \qquad (at\;\; r = b_e) \tag{5.21}$$

For a cavity with a magnetic wall at $r = b_e$ and electric walls at $\theta = \theta_1$ and θ_2, the characteristic equation can be derived from eqn.5.21 and is given by

$$\tilde{J}'_{\nu_i}(k_1 b_e) = 0 \tag{5.22}$$

The resonant mode chart of the cavity can be obtained from eqn.5.22. By solving eqns 5.18 to 5.20, the coefficients in eqns 5.16 and 5.17 are obtained as follows.

$$A_{m\nu_i} = \frac{Z_1 I_0}{2\pi d\ (1+\delta_m)} \frac{z_{m\nu_i 2}\,\tilde{Y}_{\nu_i}(k_{1p} d) - z_{m\nu_i 1}\tilde{J}_{\nu_i}(k_1 d)]}{z_{m\nu_i 2}} \tag{5.23}$$

$$C_{m\nu_i} = \frac{Z_1 I_0}{2\pi d\ (1+\delta_m)} \frac{z_{m\nu_i 1}\,\tilde{J}_{\nu_i}(k_{1p} d)}{z_{m\nu_i 2}} \tag{5.24}$$

$$D_{m\nu_i} = -\frac{Z_1 I_0}{2\pi d\ (1+\delta_m)} \tilde{J}_{\nu_i}(k_{1p} d) \tag{5.25}$$

where $\delta_m = 1$ for $m = 0$, $\delta_m = 0$ for $m > 0$, $Z_1 = \sqrt{\mu_1/\varepsilon_1}$ and

$$z_{m\nu_i 1} = \tilde{Y}'_{\nu_i}(k_{1p} b) + j\ y_{sm} Z_1\ \tilde{Y}_{\nu_i}(k_{1p} b) \tag{5.26}$$

$$z_{m\nu_i 2} = \tilde{J}'_{\nu_i}(k_{1p} b) + j\ y_{sm} Z_1\ \tilde{J}_{\nu_i}(k_{1p} b) \tag{5.27}$$

In the above derivation, the Wronskian of the spherical Bessel functions was used.

In eqns 5.26 and 5.27, the wall admittance should be determined and will be studied in the following section.

In this study, only the cases where $m>0$ are of interest. The summation with respect to the i in eqns 5.11 to 5.15 will be omitted and the subscript i of ν_i will be replaced by m in the following text, because there is a unique value of ν corresponding to each value of m larger than zero.

5.4. Wall Admittance of Biconical Microstrip Antennas

As depicted in the previous section, the fields inside the cavity are excited by the current along the center conductor of the coaxial cable and have been given by eqns

5.11 to 5.15. The wall admittance of the biconical microstrip antenna is involved in the constants $A_{m\nu_m}$, $C_{m\nu_m}$, and $D_{m\nu_m}$ and should be determined to complete the field expressions. The study of the wall admittance, or impedance, of the biconical microstrip antenna is presented in this section.

The wall admittance can be defined as [55]

$$y_{s\,m\mu_n} = g_{s\,m\mu_n} + jb_{s\,m\mu_n} = \frac{P_r + j2\,\omega\,(W_m - W_e)}{\frac{1}{2}\int_{S_a} \mathbf{E}_c\ \mathbf{E}_c^*\ d\,s} \tag{5.28}$$

where S_a is the aperture surface at $r = b$ and $\theta_1 \le \theta \le \theta_2$; $\mathbf{E}_c$ and $\mathbf{E}_c^*$ are the electric field and its conjugate inside the cavity at $r = b$; P_r, W_m and W_e are the radiation power and reactively stored energies in the region outside the cavity. Thus, the fields inside and outside the cavity are linked by the wall admittance or, sometimes, the wall impedance.

The fields outside the cavity are excited by the fields at the aperture of the cavity, i.e., at the spherical sector $r = b$ and $\theta_1 \le \theta \le \theta_2$. Since the antenna is of microstrip type, i.e., $k_1 b\,\Delta\theta \ll 1$, the aperture electric and magnetic fields may be converted to magnetic and electric current loops at $r = b$ and $\theta_c = (\theta_1 + \theta_2)/2$. By the equivalence principle, the fields outside the cavity are uniquely determined by these loops. The space defined by $\theta < \theta_2$ where the current loops lie is divided into regions I ($r < b$) and II ($r \ge b$) as shown in Fig.5.6.

For convenience, the electric potential F_r (given by eqn.5.2) in the region $d < r < b$ inside the cavity can be written in terms of the spherical Hankel function for $m > 0$

$$\left[F_r(r,\theta,\phi)\right]_{m\nu_m} = \sum_{p=0}^{\infty} B_{mp}\ \tilde{H}_{\nu_m}^{(1)}(k_{1p}\,r)\ T_{\nu_m}^{m}(\cos\theta)\ \ e^{jm\phi} \tag{5.29}$$

where $\tilde{H}_{\nu}^{(1)}(k_{mp}\,r) = k_{mp}\,r h_{\nu}^{(1)}(k_{mp}\,r)$ is the first kind spherical Hankel function, and B_{mp} is a complex constant related to the constants C_{mp} and D_{mp} and can be easily obtained

from eqns 5.24 and 5.25. The electric and magnetic current loops J_ϕ and M_ϕ can be obtained as

$$J_\phi = H_{c\theta}(k_1 b)\delta(\theta-\theta_c) \tag{5.30}$$

and

$$M_\phi = -E_{c\theta}(k_1 b)\delta(\theta-\theta_c) \tag{5.31}$$

where $H_{c\theta}$ and $E_{c\theta}$ are given by eqns 5.11 and 5.14. The outside fields of *TE* and *TM* modes are induced by J_ϕ and M_ϕ, respectively.

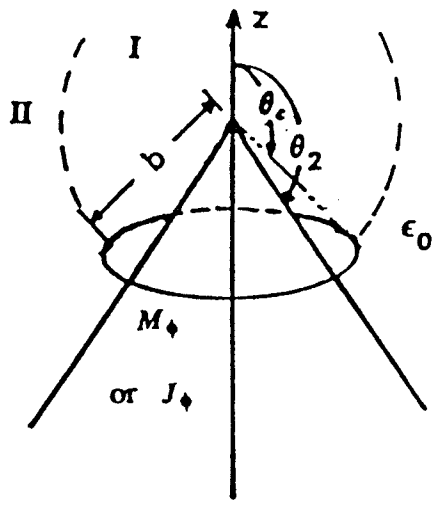

Fig.5.6: The current loops and fields outside the cavity.

Since the biconical structure is of microstrip type, the very narrow aperture at the edge of the spherical sector may be considered as a magnetic spherical wall, similar to most first order approximations for the microstrip type antennas. For verification, the numerical values of the electromagnetic fields at the cavity aperture expressed by eqns 5.11 to 5.14, are plotted in Fig.5.7. It shows that E_θ, the θ component of the electric field, is largest of the four aperture fields. Its value is at least hundred times of the values of other three components for $90^0 \le \theta_2 < 165^0$. Thus, the fields *TM* to r, induced

by M_ϕ, make the most contribution to the fields outside the cavity. Other equivalent currents on the aperture of the cavity are J_θ and M_θ converted by the cavity fields H_ϕ and E_ϕ, respectively. The *TE* and *TM* modes outside the cavity are also induced by these current sources. The contribution to the *TM* modes from E_ϕ is insignificant since E_ϕ is much less than E_θ, as shown in Fig.5.7. H_ϕ can also be neglected as an aperture current source of the *TE* modes. The reson is that as stated by eqn.5.18, H_ϕ is the product of E_θ and the wall admittance, and the wall admittance is much smaller than unity, since the antenna structure is of microstrip type. The very small value of the equivalent current source J_θ converted by the H_ϕ causes that the coefficients a_{mu_n} and b_{mu_n} in the following expressions for the electric fields of *TE* modes in the interior and exterior regions I and II

$$\begin{bmatrix} E_\theta^I \\ E_\theta^{II} \end{bmatrix}_{mu_n} = \begin{matrix} a_{mu_n}\tilde{J}_{u_n}(k_0 r) \\ b_{mu_n}\tilde{H}_{u_n}^{(2)}(k_0 r) \end{matrix} \quad \frac{jm}{r\sin\theta} P_{u_n}^m(\cos\theta)e^{jm\phi}$$

$$\begin{bmatrix} E_\phi^I \\ E_\phi^{II} \end{bmatrix}_{mu_n} = \begin{matrix} a_{mu_n}\tilde{J}_{u_n}(k_0 r) \\ b_{mu_n}\tilde{H}_{u_n}^{(2)}(k_0 r) \end{matrix} \quad \frac{1}{r} \frac{dP_{u_n}^m(\cos\theta)}{d\theta} e^{jm\phi}$$

are much less than the coefficients c_{μ_n} and d_{μ_n} (will study in detail later). Therefore, only the *TM* modes are considered and only M_ϕ is taken as their source for the first order approximation in the following analysis.

For the *TM* modes, the fields in both interior region I ($r \le b$) and exterior region II ($r > b$) are obtained as follows [53].

$$\begin{bmatrix} E_r^I \\ E_r^{II} \end{bmatrix}_{m\mu_n} = \begin{matrix} c_{m\mu_n}\tilde{J}_{\mu_n}(k_0 r) \\ d_{m\mu_n}\tilde{H}_{\mu_n}^{(2)}(k_0 r) \end{matrix} \quad \frac{1}{r^2} \frac{\mu_n(\mu_n+1)}{j\omega\varepsilon} P_{\mu_n}^m(\cos\theta)e^{jm\phi} \qquad (5.32)$$

$$\begin{bmatrix} E_\theta^I \\ E_\theta^{II} \end{bmatrix}_{m\mu_n} = - \begin{matrix} c_{m\mu_n}\tilde{J}'_{\mu_n}(k_0 r) \\ d_{m\mu_n}\tilde{H}'^{(2)}_{\mu_n}(k_0 r) \end{matrix} \quad \frac{j\eta_0}{r} \frac{dP_{\mu_n}^m(\cos\theta)}{d\theta} e^{jm\phi} \qquad (5.33)$$

$$\begin{bmatrix} E_\phi^I \\ E_\phi^{II} \end{bmatrix}_{m\mu_n} = \begin{matrix} c_{m\mu_n}\tilde{J}'_{\mu_n}(k_0 r) \\ d_{m\mu_n}\tilde{H}'^{(2)}_{\mu_n}(k_0 r) \end{matrix} \quad \frac{m\eta_0}{r\sin\theta} P_{\mu_n}^m(\cos\theta)e^{jm\phi} \qquad (5.34)$$

$$\begin{bmatrix} H_\theta^I \\ H_\theta^{II} \end{bmatrix}_{m\mu_n} = \begin{matrix} c_{m\mu_n}\tilde{J}_{\mu_n}(k_0 r) \\ d_{m\mu_n}\tilde{H}^{(2)}_{\mu_n}(k_0 r) \end{matrix} \quad \frac{jm}{r\sin\theta} P^m_{\mu_n}(\cos\theta) e^{jm\phi} \tag{5.35}$$

$$\begin{bmatrix} H_\phi^I \\ H_\phi^{II} \end{bmatrix}_{m\mu_n} = - \begin{matrix} c_{m\mu_n}\tilde{J}_{\mu_n}(k_0 r) \\ d_{m\mu_n}\tilde{H}^{(2)}_{\mu_n}(k_0 r) \end{matrix} \quad \frac{1}{r} \frac{dP^m_{\mu_n}(\cos\theta)}{d\theta} e^{jm\phi} \tag{5.36}$$

where $\eta_0=\sqrt{\mu_0/\varepsilon_0}$ and μ_n are the roots of

$$P^m_\mu(\cos\theta_2) = 0 \tag{5.37}$$

to satisfy the tangential electric fields vanishing at $\theta = \theta_2$. The mode chart, the relationship between μ_n and θ_2, is shown in Fig.5.8 for $n = 1$ to 3 when $m = 1$.

For $m > 0$, E_θ at $r = b$ must be discontinuous by an amount equal to the surface current density M_ϕ [52], i.e.,

$$E^{II}_\theta - E^I_\theta = M_\phi \tag{5.38}$$

Applying the Wronskian of the spherical Bessel functions and the orthogonality relationship of the associated Legendre functions to eqn.5.38, we obtain

$$d_{m\mu_n} = -j \frac{m}{\eta_0} \frac{\tilde{J}_{\mu_n}(k_0 b)}{N^m_{\mu_n}} \left[\frac{dP^m_{\mu_n}(\cos\theta)}{d\theta}\right]_{\theta=\theta_c} \sum_{p=0}^{\infty} B_{mp} \tilde{H}^{(1)}_{\nu_m}(k_{mp} b)\, T^m_{\nu_m}(\cos\theta_c) \tag{5.39}$$

and

$$c_{m\mu_n} = \frac{\tilde{H}^{(2)}_{\mu_n}(k_0 b)}{\tilde{J}_{\mu_n}(k_0 b)} d_{m\mu_n} \tag{5.40}$$

where

$$N^m_{\mu_n} = \frac{\mu_n(\mu_n+1)}{2\mu_n+1} \left[\sin\theta \frac{\partial P^m_\mu(\cos\theta)}{\partial\theta} \frac{\partial P^m_\mu(\cos\theta)}{\partial\mu}\right]_{\theta=\theta_2,\mu=\mu_n} \tag{5.41}$$

is the normalization factor of the orthogonal associated Legendre functions.

The far fields (at the region $\theta>\theta_2$ and $r \gg b$), for the *TM* modes, can be obtained as

$$E_{\theta m\mu_n} = -j^{\mu_n+1} d_{m\mu_n} \eta_0 \frac{e^{-jk_0 r}}{r} \frac{dP^m_{\mu_n}(\cos\theta)}{d\theta} e^{jm\phi} \tag{5.42}$$

and

$$E_{\phi m\mu_n} = j^{\mu_n} m \; d_{m\mu_n} \eta_0 \frac{e^{-jk_0 r}}{r} \frac{P^m_{\mu_n}(\cos\theta)}{\sin\theta} e^{jm\phi} \tag{5.43}$$

The radiation power and the stored energies per cycle can be obtained by the following integrations

$$P_r = \frac{1}{2\eta_0} \int_{S_\infty} \mathbf{E}_r \cdot \mathbf{E}_r^* \, ds \tag{5.44}$$

where S_∞ is a spherical sector at $r = \infty$, $\theta \le \theta_2$ and $0 \le \phi \le 2\pi$.

$$W_e = \frac{\varepsilon}{4} \left[\int_{V^I} \mathbf{E}^I \cdot \mathbf{E}^{I*} \, dv + \int_{V^{II}} \mathbf{E}^{II} \cdot \mathbf{E}^{II*} \, dv \right] \tag{5.45}$$

$$W_m = \frac{\mu}{4} \left[\int_{V^I} \mathbf{H}^I \cdot \mathbf{H}^{I*} \, dv + \int_{V^{II}} \mathbf{H}^{II} \cdot \mathbf{H}^{II*} \, dv \right] \tag{5.46}$$

Using the Wronskian of the spherical Bessel functions, the orthogonality relationship of the associated Legendre functions and the radiation conditions at infinity, the real part of the wall admittance is obtained in a closed form as

$$g_{s\, m\mu_n} = [-m^2 \frac{[\frac{dP^m_{\mu_n}\cos(\theta)}{d\theta} T^m_{\nu_m}(\cos\theta)]^2_{\theta=\theta_c}}{N^m_{\mu_n} \quad N^m_{\nu}}] \; \tilde{J}_{\mu_n}(k_0 b) \; \tilde{J}_{\mu_n}(k_0 b) \tag{5.47}$$

and the imaginary part is

$$b_{s\, m\mu_n} = [\, m^2 \frac{[\frac{dP^m_{\mu_n}\cos(\theta)}{d\theta} T^m_{\nu_m}(\cos\theta)]^2_{\theta=\theta_c}}{N^m_{\mu_n} \quad N^m_{\nu_m}}] \; \tilde{J}_{\mu_n}(k_0 b) \; \tilde{Y}_{\mu_n}(k_0 b) \tag{5.48}$$

where

$$N^m_{\nu_m} = \frac{\nu_m(\nu_m+1)}{2\nu_m+1}[\sin\theta\, T^m_\nu(\cos\theta)\, \frac{\partial^2 T^m_\nu(\cos\theta)}{\partial\theta\, \partial\nu}]^{\theta_2}_{\theta_1,\nu=\nu_m} \tag{5.49}$$

Some calculated values of $g_{s\,m\mu_n}$ and $b_{s\,m\mu_n}$ are shown in Figs 5.9-5.14 for some selected geometries. In Figs 5.11-5.14, $g_{s\,m\mu_n}$ and $b_m\ \mu_n$ are plotted against the relative length of the cone cap b/λ for $\theta_2 = 90^0, 120^0, 135^0$ and 150^0. For all selected values of θ_2, when n, the order of the radiation mode, increases, both $g_{s\,m\mu_n}$ and $b_{s\,m\mu_n}$ decrease. But, $g_{s\,m\mu_n}$ decreases much faster than $b_{s\,m\mu_n}$. The convergences of $g_{s\,m\mu_n}$ and $b_m\ \mu_n$ are shown in Figs 5.11a-5.14a for the above cases. From these figures, one can see that $g_{s\,m\mu_n}$ is converged very fast. The summation of the first two or three terms is almost the same as that of the first nine terms. Therefore, for the calculating of $g_{s\,m\mu_n}$, only three terms are needed. But, the convergence of $b_{s\,m\mu_n}$ is slow, and becomes serious, as θ_2, the cone angle, increases. For computing $b_{s\,m\mu_n}$, therefore, at least seven terms are needed.

5.5. Input Impedance, Bandwidth and Radiation Patterns

The input impedance is calculated from an equivalent parallel resonant network as shown in Fig.3.2, which is the network model over a narrowband for the isolated TM_{11} mode. The resistive and reactive parts are determined by the radiation power, dielectric and conductor losses and the stored energies [41]. It is given by

$$Z_{in} = \frac{\frac{1}{2}VV^*}{P_t+2j\,\omega(W_e-W_m)} \tag{5.50}$$

where V is the voltage crossing the patch and ground plane at $r = d$ calculated from

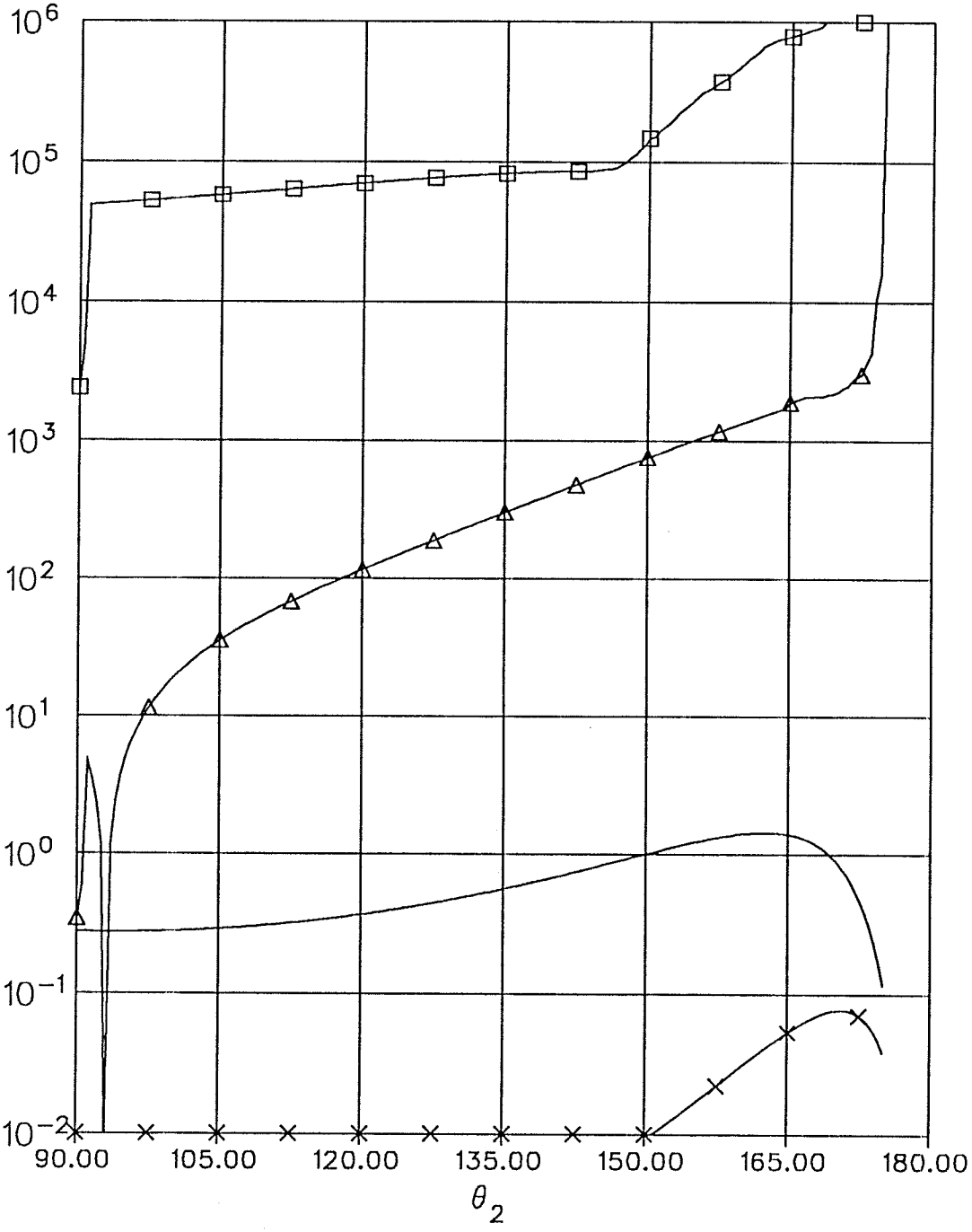

Fig.5. 7: EM fields at the cavity aperture at r = b, where $\Delta\theta = 6^0$ and m = 1

E_θ , H_θ , b = 3.0354 cm

E_φ , H_φ , ε_r = 2.52

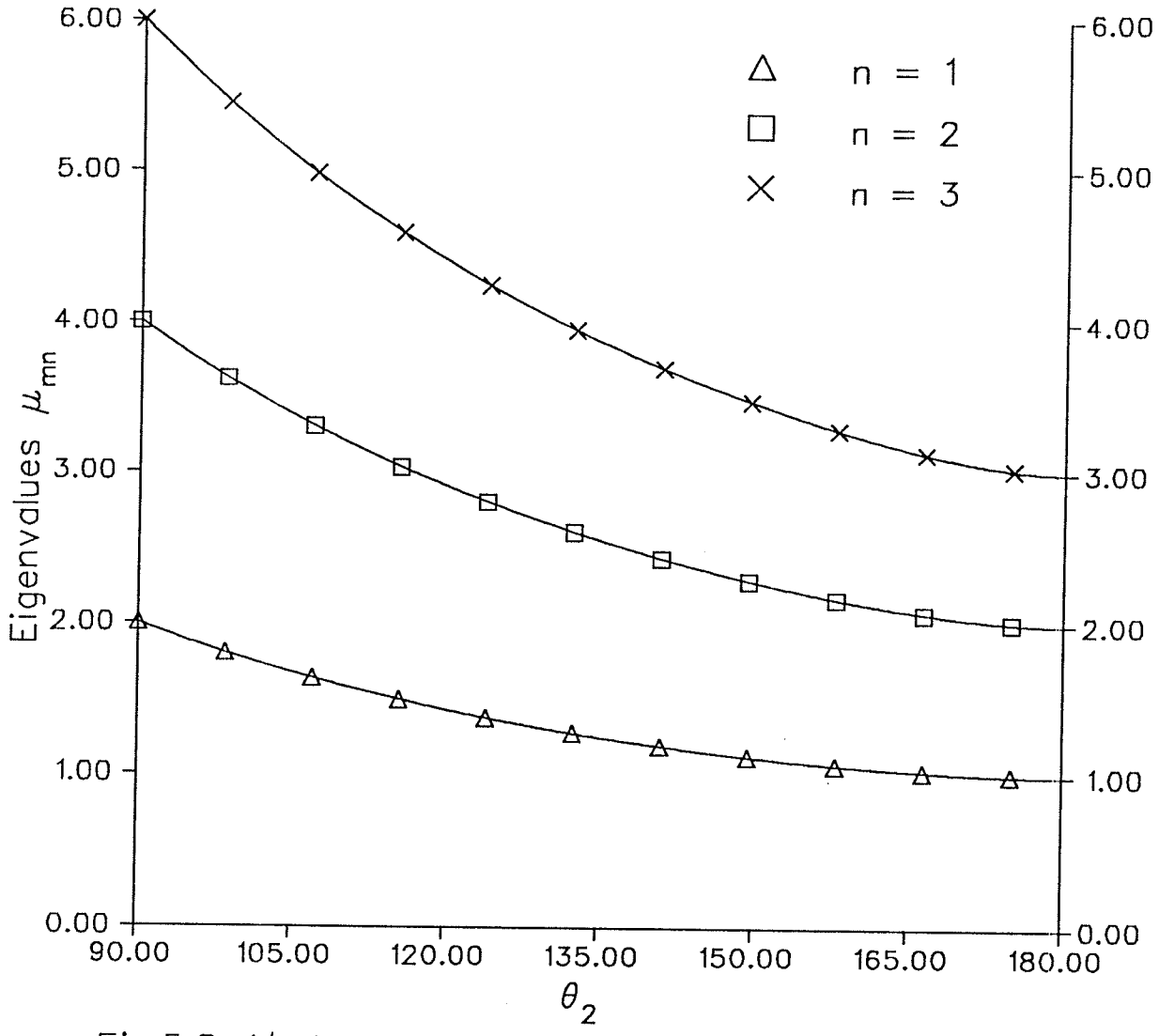

Fig.5.8: Mode chart, the relationship between μ_{mn} and θ_2 of Fig.5.6, where m = 1.

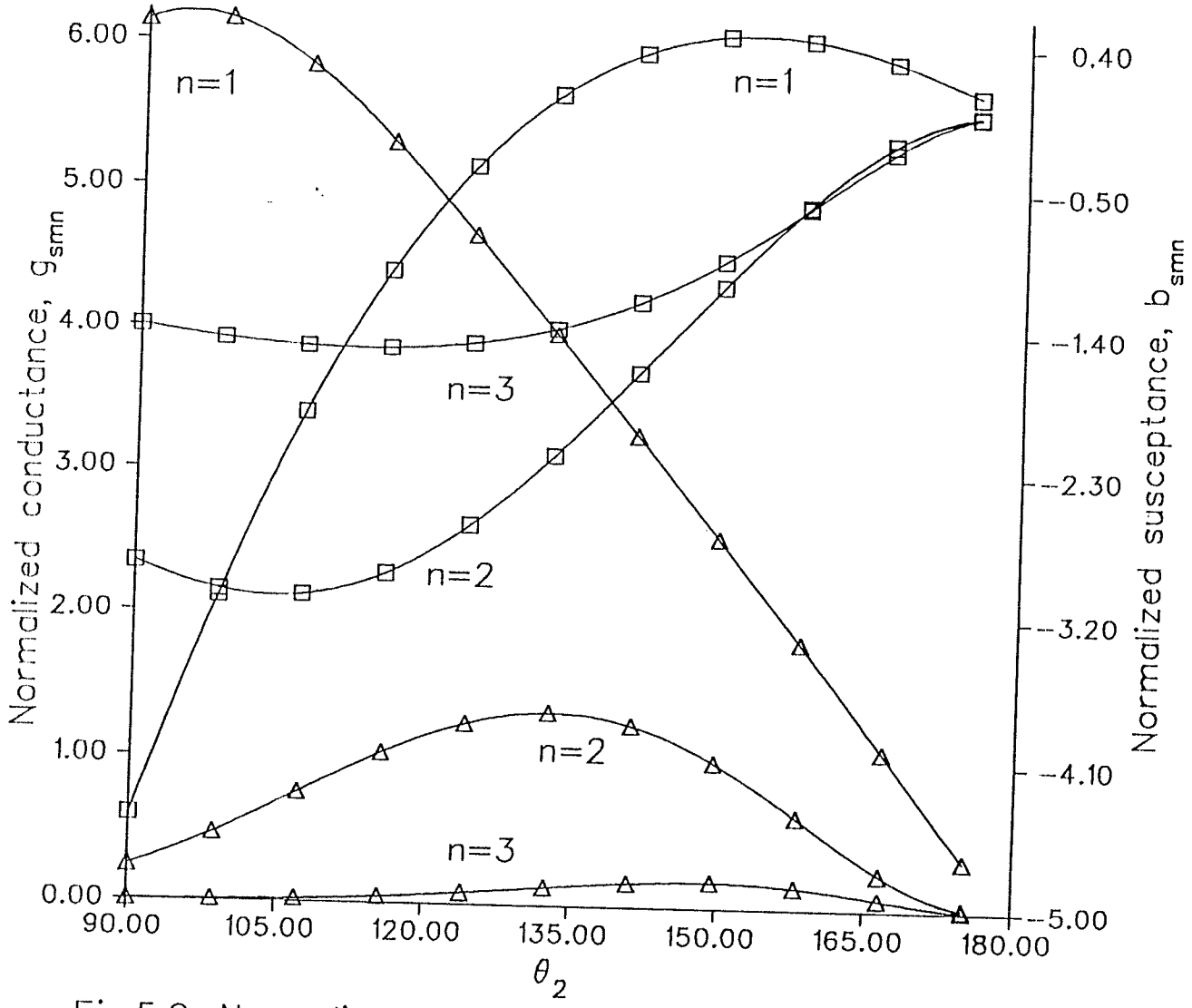

Fig.5.9: Normalized wall conductances and susceptances for $k_0 b = \pi$, m = 1 and $\Delta\theta = 6^0$

△ Conductance

□ Susceptance

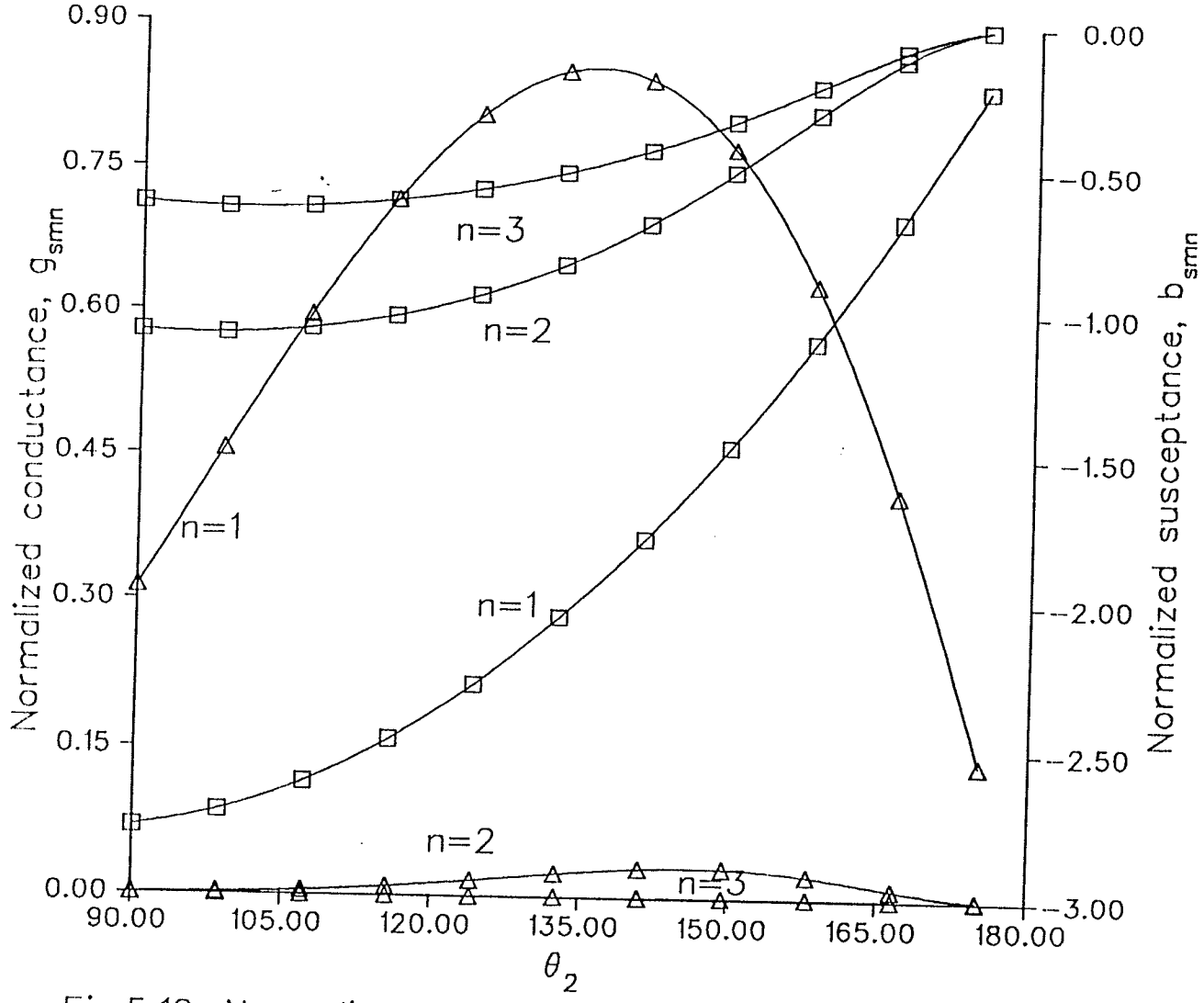

Fig.5.10: Normalized wall conductances an susceptances for $k_0 b = \pi/2$, m =1 and $\Delta\theta = 6^0$

△ conductance

□ susceptance

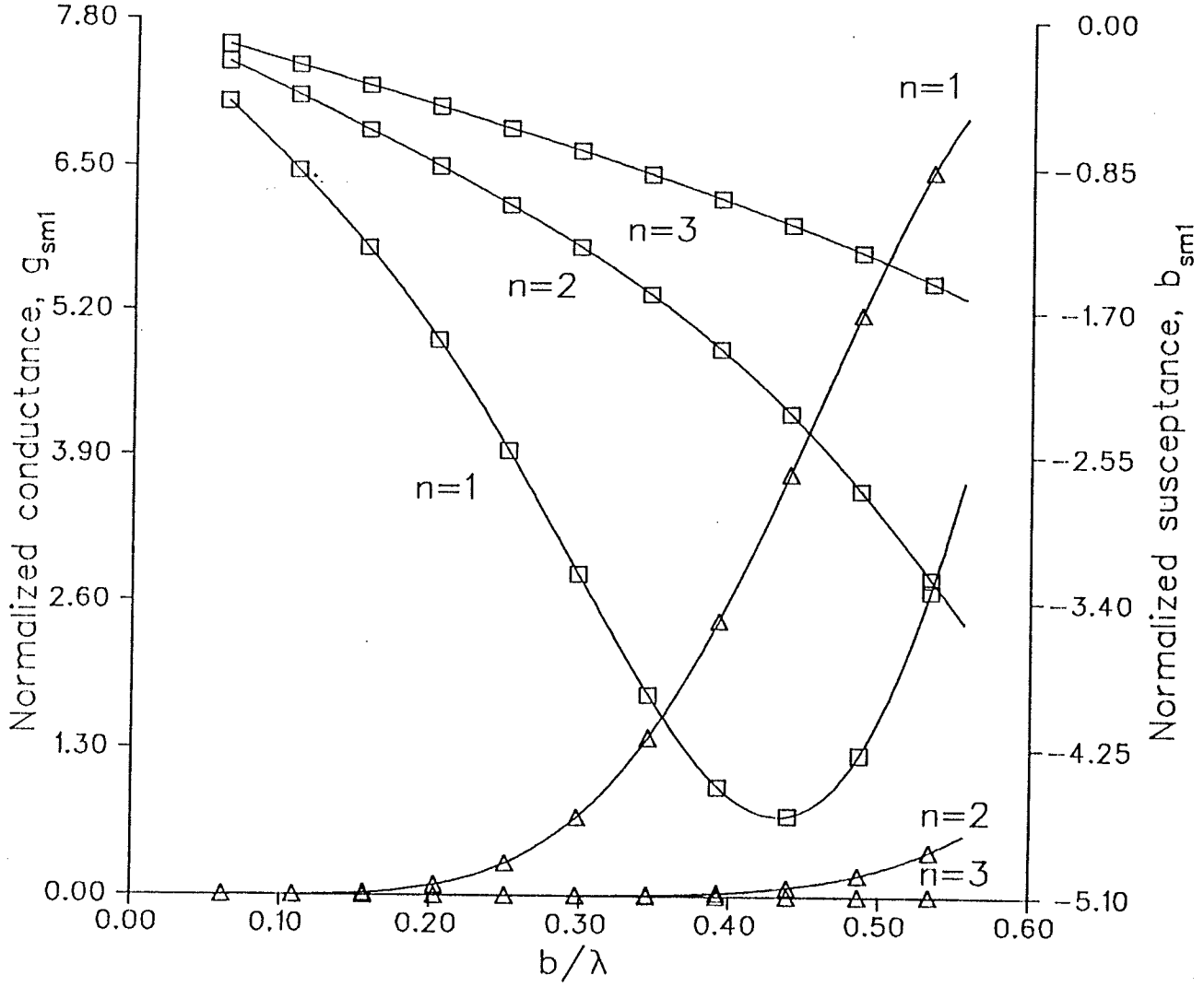

Fig.5.11: Normalized wall conductances and susceptances for $\theta_2 = 90^0$, m = 1 and $\Delta\theta = 6^0$

△ conductance

□ susceptance

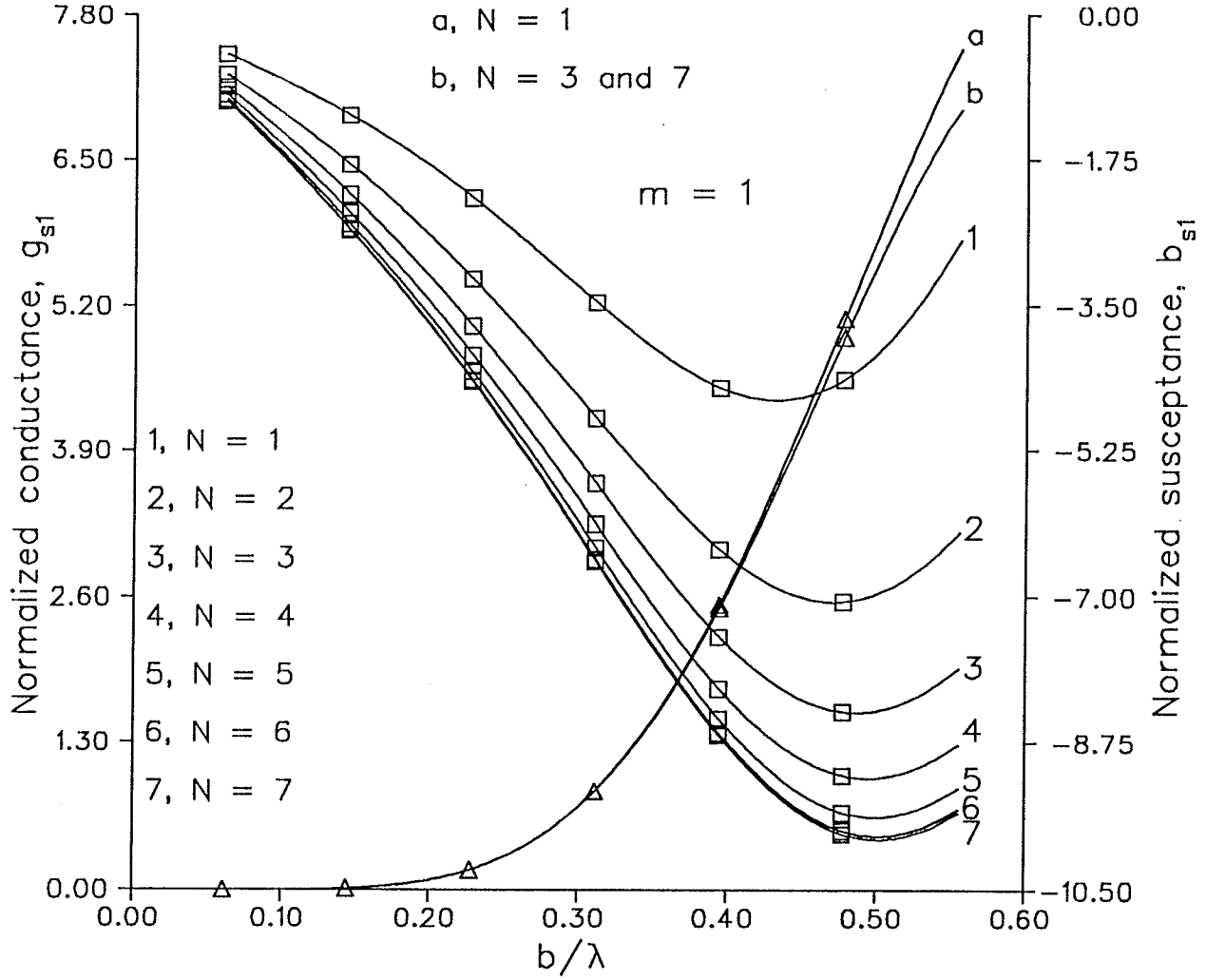

Fig.5.11a: Convergence of the wall conductance and susceptance for $\theta_2 = 90^0$, N is the total number terms selected and $\Delta\theta = 6^0$

△ Normalized conductance

□ Normalized susceptance

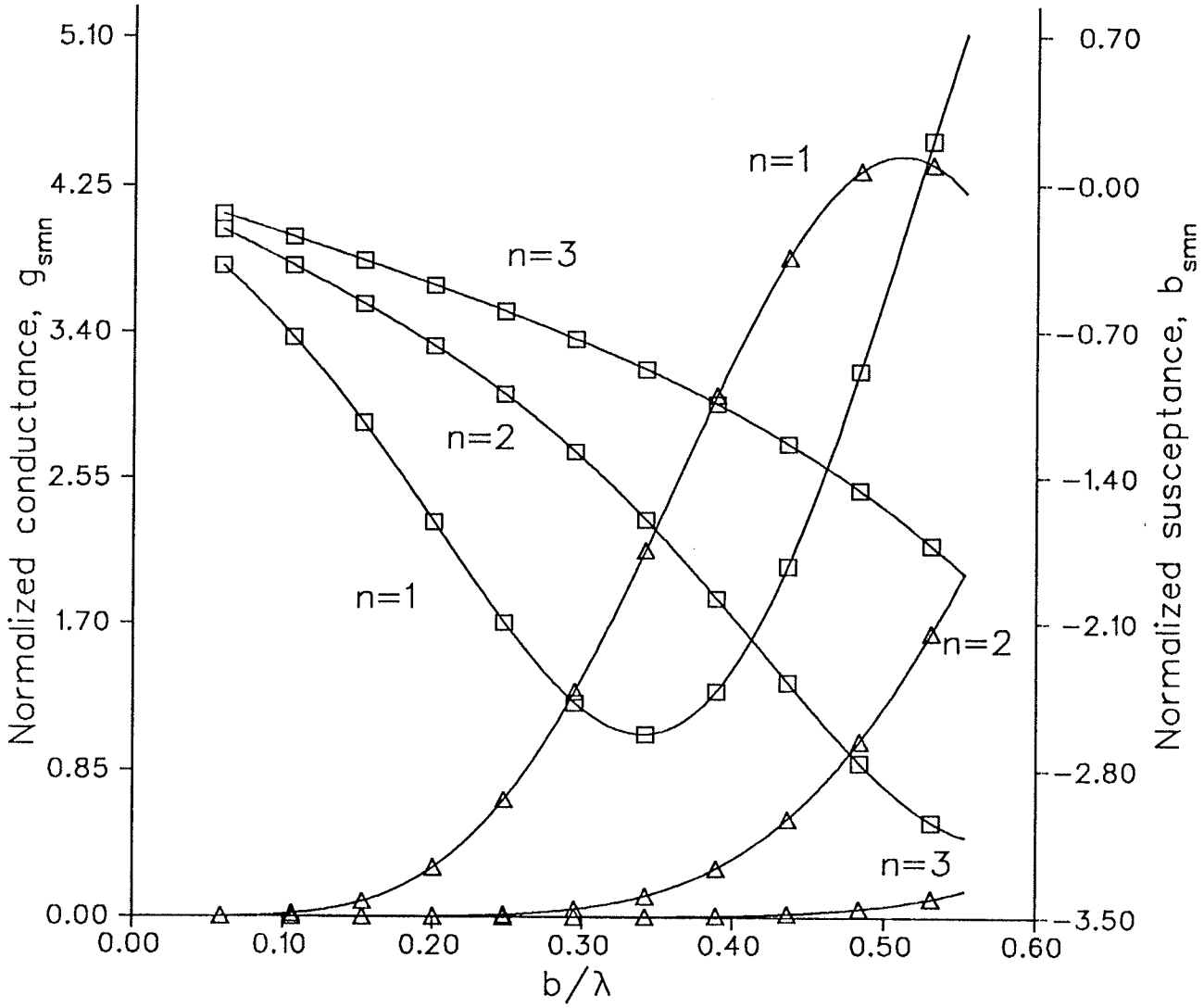

Fig.5.12: Normalized wall conductances and susceptances by $\sqrt{\mu_0/\epsilon_0}$,for $\theta_2 = 120^0$ and m = 1 ,

△ conductance

□ susceptance

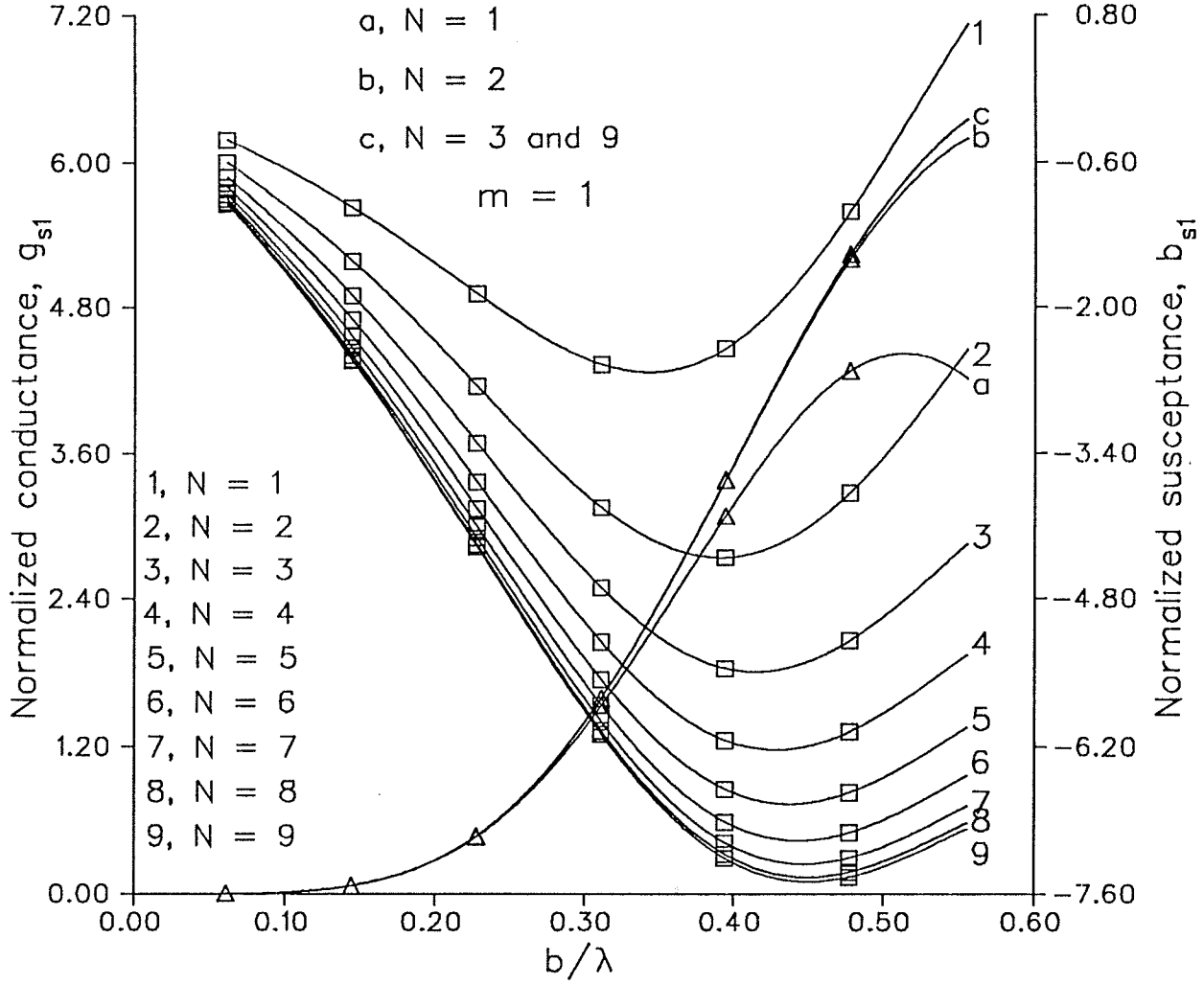

Fig.5.12a: Convergence of the wall conductance and susceptance for $\theta_2 = 120^0$, N is the total number terms selected and $\Delta\theta = 6^0$

△ Normalized conductance

□ Normalized susceptance

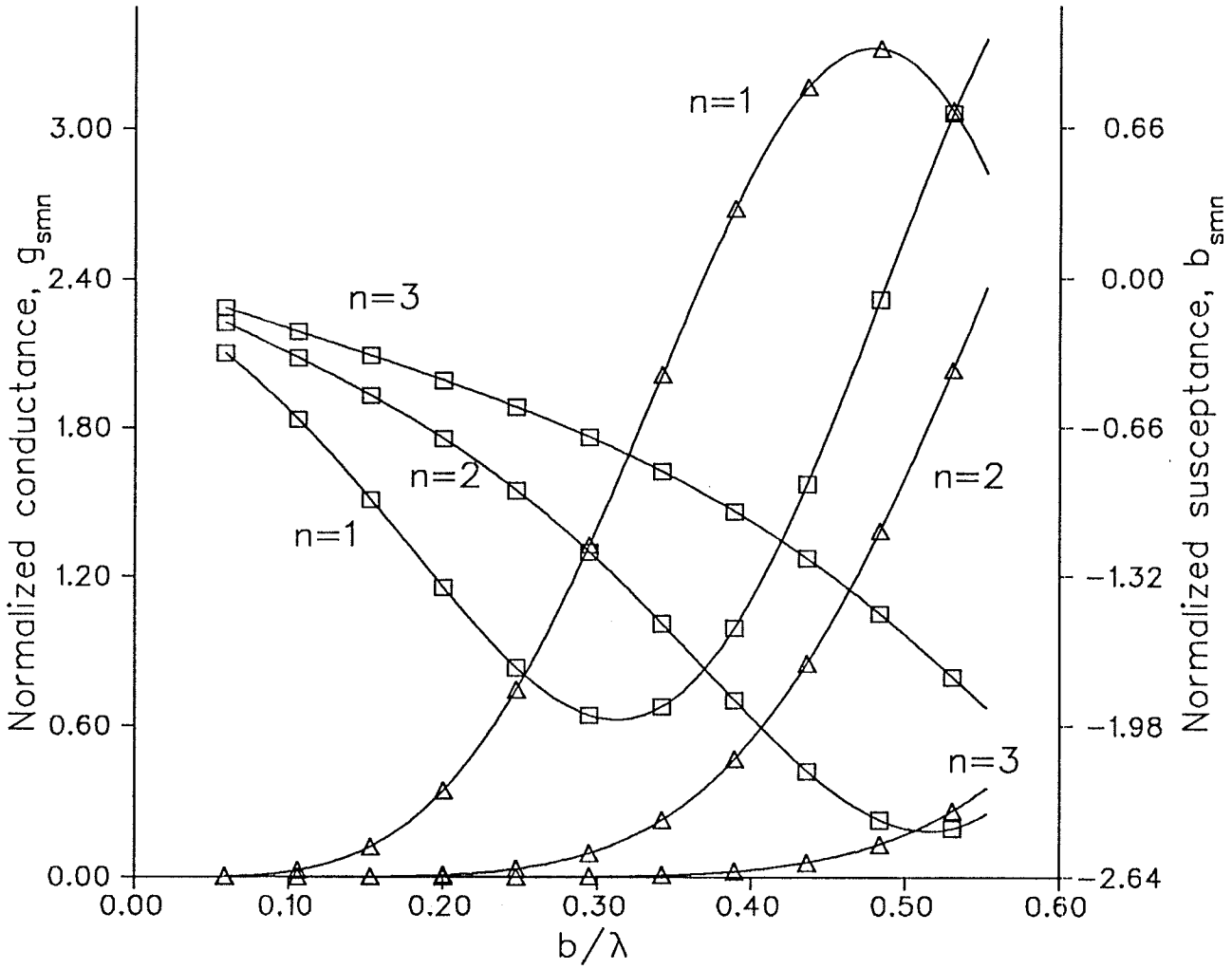

Fig.5.13: Normalized wall conductances a susceptances by $\sqrt{\mu_0/\varepsilon_0}$, for $\theta_2 = 135^0$ and m = 1 ,

△ conductance

□ susceptance

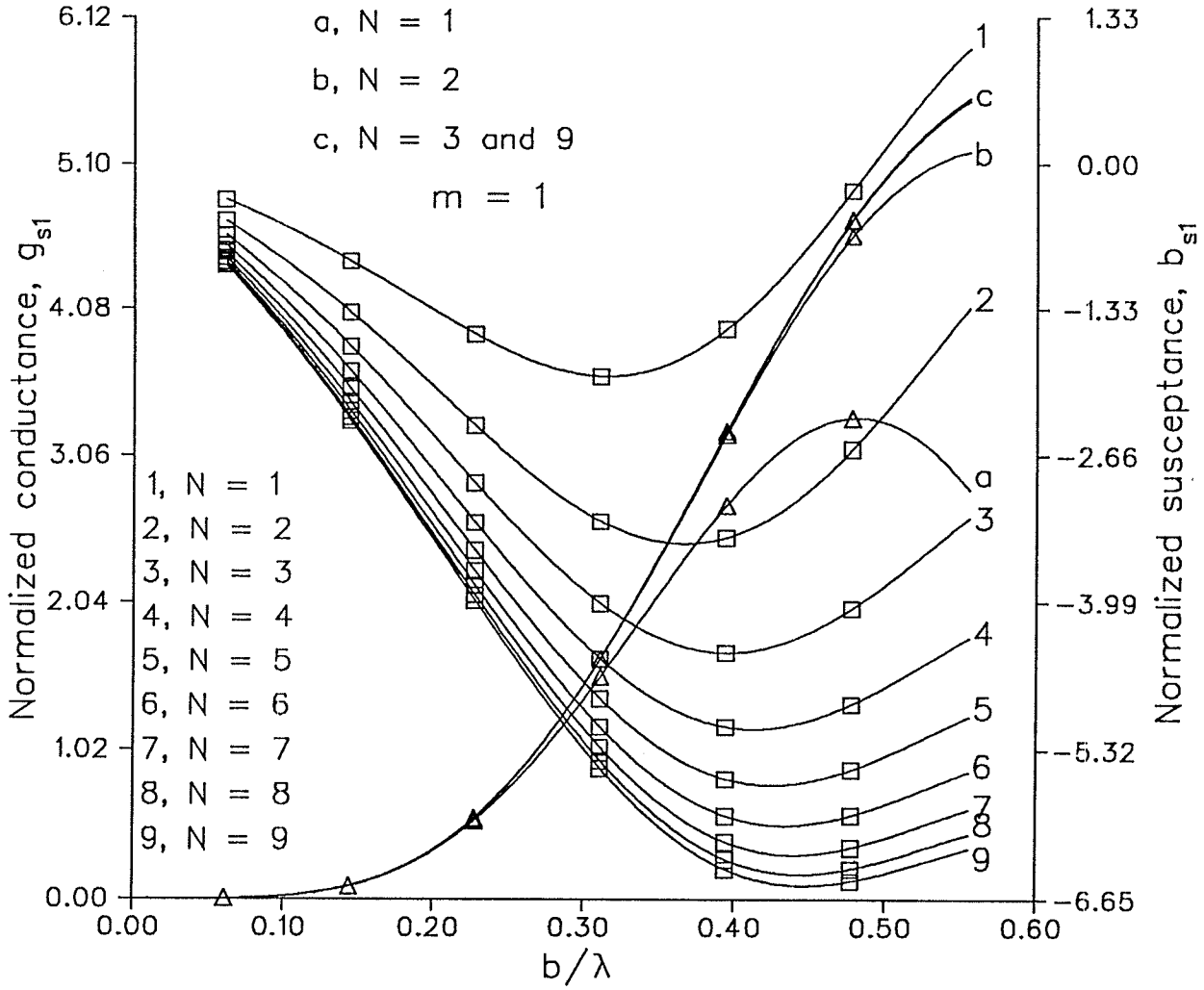

Fig.5.13a: Convergence of the wall conductance and susceptance for $\theta_2 = 135^0$, N is the total number terms selected and $\Delta\theta = 6^0$

△ Normalized conductance

□ Normalized susceptance

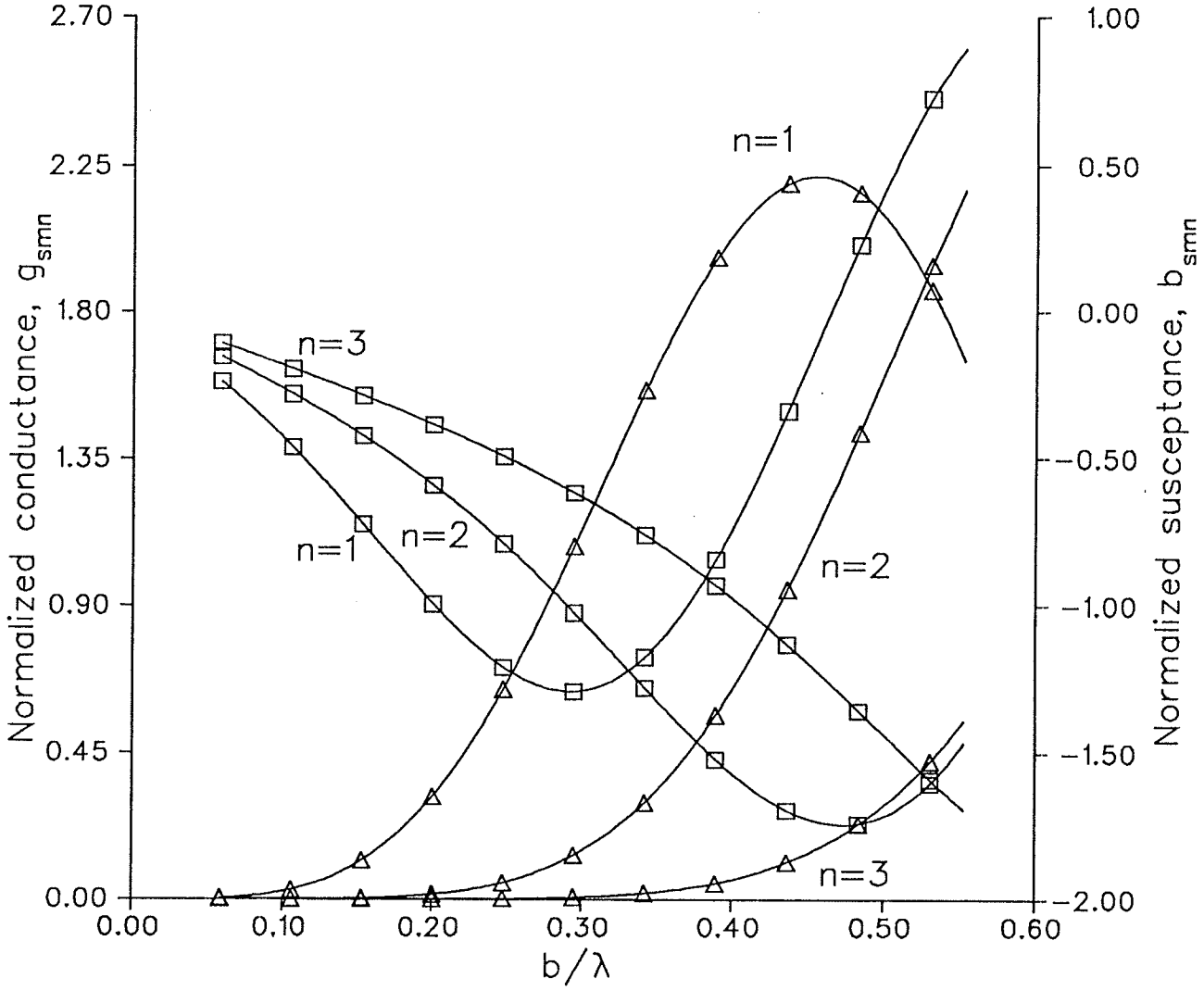

Fig.5.14: Normalized wall conductances a susceptances by $\sqrt{\mu_0 \epsilon_0}$, for $\theta_2 = 150^0$ and m = 1 ,

△ conductance

□ susceptance

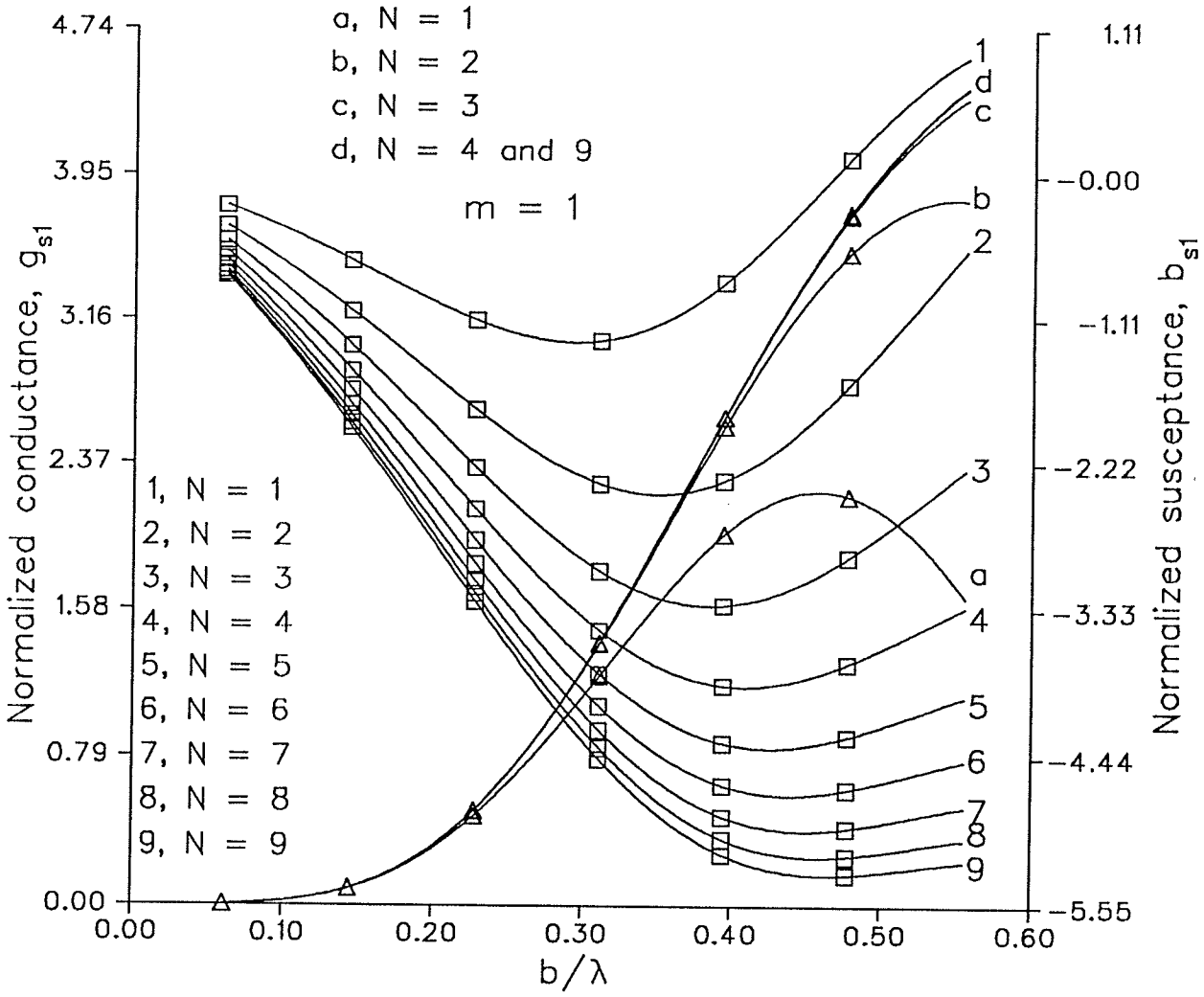

Fig.5.14a: Convergence of the wall conductance and susceptance for $\theta_2 = 150^0$, N is the total number terms selected and $\Delta\theta = 6^0$

△ Normalized conductance

□ Normalized susceptance

$$V = \int_0^d E_z \, dz \quad , \tag{5.51}$$

and W_e and W_m are the stored electric and magnetic energies per cycle, respectively, given by

$$W_e = \frac{\varepsilon}{4} \int_v \mathbf{E} \cdot \mathbf{E}^* \, dv \quad , \tag{5.52}$$

$$W_m = \frac{\mu}{4} \int_v \mathbf{H} \cdot \mathbf{H}^* \, dv \quad , \tag{5.53}$$

where the electromagnetic fields **E** and **H** are given by eqns 5.11-5.15.

P_t is the total lost power as

$$P_t = P_{rad} + P_d + P_l \tag{5.54}$$

where

$$P_d = 2 \, \omega \, W_e \tan \delta \tag{5.55}$$

$$P_l = \frac{2 \, \omega \, r_s}{N_v^m} W_m \tag{5.56}$$

and $\tan \delta$ is the loss tangent of the dielectric, and $r_s = (\pi \mu \sigma f)^{1/2}$.

The bandwidth is determined in terms of the Q factor and maximum allowable VSWR and is defined as

$$BW = \frac{VSWR - 1}{Q \sqrt{VSWR}} \tag{5.57}$$

where

$$Q = \frac{2 \, \omega \, W_e}{P_t} \tag{5.58}$$

Using the formulations developed in this section, the near field characteristics are calculated for some selected geometries.

Table 5.2 lists the resonance frequency, bandwidth and input resistance at resonance for two pairs of conical microstrip antennas with substrate dielectric constants 1.0 and 2.52. The data listed in the first and the third rows of this table are the calculated results for $\Delta\theta = 6^0$ ($\theta_2 = 90^0$ and $\theta_1 = 84^0$). The data shown in the fourth row are taken from a roughly made antenna model. The conducting cone of this antenna model was made of copper strips with conducting glue and laid on a cone shape dielectric substrate.

The data shown in this table illustrate good agreement between the calculated and measured resonance frequencies and input resistance at resonance. The calculated resonance frequency for the air dielectric case also agrees with the measured one from [38]. In [38] the measured data for the wider angles ($\theta_1 = 72^0$ and 75^0) were taken on the thick substrate of $h \approx 0.1\lambda_g$. The theoretical analysis of this dissertation is not valid for the wide angles (i.e., cannot satisfy the condition: $k_1 b\,\Delta\theta = k_1 h \ll 1$), which corresponds to the case of thick substrate in [38]. The large difference on the bandwidth between the calculated and measured data may be partly due to rough construction of the antenna model. The unsmooth cone surface and poor connection between the conducting cone and the substrate reduce the radiation power, and hence decrease the cavity power loss significantly. Their effect on the ohmic loss also increases, but this increase is much less than the decrease of the radiation loss. The reduction of the total cavity power loss causes the reduction of the measured bandwidth. The approximation in the calculation of the wall admittance is another reason for the disagreement in the bandwidth. The omitted contribution to the radiation from the *TE* modes outside the cavity may cause errors in the analytical value of the bandwidth. Also, the effect of the dielectric substrate on the radiation is omitted in the derivation of the wall conductance. Although this effect is insignificant, it increases the calculated bandwidth. For more accurate analysis, this effect and the contribution to the radiation from the *TE* modes should be included in the further research work.

$\theta_1(degree)$	$f_r(GHz)$	$BW(\%)$	$R_{in}(\Omega)$	ε_r	$b(cm)$
84	5.472811	4.25299	57.1468	1.0	1.861
85(a)	5.46	-	-	1.0	1.861
84	2.073825	2.48893	45.2955	2.52	3.0354
84(b)	2.06	1.75	45.687	2.52	3.0354

Table 5.2: Near field characteristics of conical microstrip antennas (θ_2=90^0)
(a) measured data from [38], (b) measured data by author.

Table 5.3 illustrates the data calculated by the formulation in Chapter 3, for similar sizes conventional circular patch microstrip antennas. Two pairs of substrate height and the radius are chosen to ensure that the sizes of the circular patch are similar to those of conical microstrip antennas in Table 5.2. The radii of the circular patch are obtained by projecting the cone arm length b on the ground plane that equals b cos $\Delta\theta$. Thus, the height of the substrate is $h = b$ sin$\Delta\theta$.

$h(mm)$	$f_r(GHz)$	$BW(\%)$	$R_{in}(\Omega)$	ε_r	$b(cm)$
1.5875	4.249669	2.78627	49.5641	1.0	1.85
3.175	3.989081	4.78019	49.5755	1.0	1.85
3.175	1.727729	1.77058	49.5065	2.52	3.0188
1.5875	1.766738	0.99157	49.2977	2.52	3.0188

Table 5.3: Near field characteristics of ordinary circular patch antennas
similar in size to the antennas in Table 5.2.

Comparing the data shown in Tables 5.2 and 5.3, one can conclude that the conical microstrip antenna has a wider bandwidth. The antenna sizes in the first and the third rows of both tables are considered to be similar to each other. The bandwidths of these two conical microstrip antennas are at least 50 % larger than those of the circular ones. This increase in the bandwidth of the narrow angle conical microstrip antenna is less than twice the bandwidth of ordinary patches for the wide angle conical ones as indicated in [38]. However, the improvement in the bandwidth of the narrow angle conical microstrip antennas is still significant.

Table 5.4 illustrates the resonance frequencies, bandwidths and input resistances at resonance for $\theta_2 = 90^0$, 120^0, 135^0 and 150^0 with the same cap length of

$b = 3.0354cm$, $d = 1.06cm$ and $\varepsilon_r = 2.52$. For all these geometries, the bandwidths of the biconical microstrip antennas are wider than the bandwidth of the circular patch antenna shown in the third row of Table 5.3.

$\theta_2(degree)$	$f_r(GHz)$	$BW(\%)$	$R_{in}(\Omega)$	ν	kb
90	2.073835	2.48893	45.2955	0.619171	2.09435
120	2.185729	3.44549	14.8008	0.729252	2.20735
135	2.383275	4.52339	10.3904	0.936565	2.40685
150	2.725913	3.50199	11.4037	1.465652	2.75288

Table 5.4: Near field characteristics of biconical microstrip antennas for $\Delta\theta=6^0$.

The radiation patterns can be obtained from eqns 5.42 and 5.43. The calculated radiation patterns are shown in Figs 5.15-5.18, for the same geometries as those listed in Table 5.4. As expected, for $m = 1$ the maximum radiation is at $\theta = 0^0$. This is an important difference from the wraparound conformal microstrip antennas. The radiation in the broadside suggests that these antennas can be applied to the tip of high speed vehicles when the forward looking capability is needed. The high sidelobe appears along the grounded cone for all selected values of θ_2. As θ_2 increases, the sidelobe level decreases and the null position (at $\theta \approx 45^0$ for $\theta_2=90^0$) moves closer to the z axis. Also, as θ_2 increases, the contribution of higher order modes to the radiation power increases. At $\theta_2=150^0$, the contribution of the second mode is almost equals to that of the dominant mode. Thus, for the large values of θ_2, one must take more radiation modes, in the calculation, to ensure the accuracy of the results.

Table 5.5 shows the calculated directivity of the biconical microstrip antennas for the selected values of θ_2 as in Table 5.4 . Their directivity is higher than that of similar size conventional circular patch antennas as shown in the third row of Table 5.3.

The characteristics of biconical microstrip antennas depicted in this section show that they are excellent substitutes for wraparound conformal microstrip antennas. Also, it is shown that the conical microstrip antenna, the special case of the biconical antennas, is an excellent alternative for the circular patch microstrip antenna.

$\theta_2(degree)$	kb	$dir(dB)$	ν_{11}	μ_{11}	μ_{12}	μ_{13}
90	2.09435	8.82446	0.619171	2.0	4.0	6.0
120	2.20735	9.29955	0.729252	1.42412	2.90434	4.39575
135	2.40685	9.86992	0.936565	1.24508	2.54899	3.86854
150	2.75288	10.42490	1.46565	1.1565	2.27797	3.45786

Table 5.5: Far field characteristics of biconical microstrip antennas.

5.6. Summary

A new type of conformal microstrip antenna, the biconical microstrip antenna, was proposed in this chapter. The theoretical analysis of these antennas was based on the modal expansion method, in which the electromagnetic fields inside the cavity were expanded in terms of the existing spherical wave eigenfunctions, i.e., the cavity modes. The investigation of the eigenvalues of the ϕ dependent spherical wave functions for biconical microstrip structures showed that the only existing cavity modes are *TE* modes and for each nonzero order ($m>0$), there is an unique degree ν. To match the fields between the cavity and free space, the wall admittance at the aperture was studied in this chapter. In a closed form, the expressions of the wall admittance were obtained to complete the modal expansion for the biconical microstrip antennas. The characteristics of biconical microstrip antennas were illustrated for some selected geometries. The analysis shows that they can provide wider bandwidth, higher gain and the ability of forward radiation. Their superior performances suggest that they could be very useful antennas in many applications, especially, when the forward radiation is necessary. Their main disadvantage is in the difficulty of their fabrication.

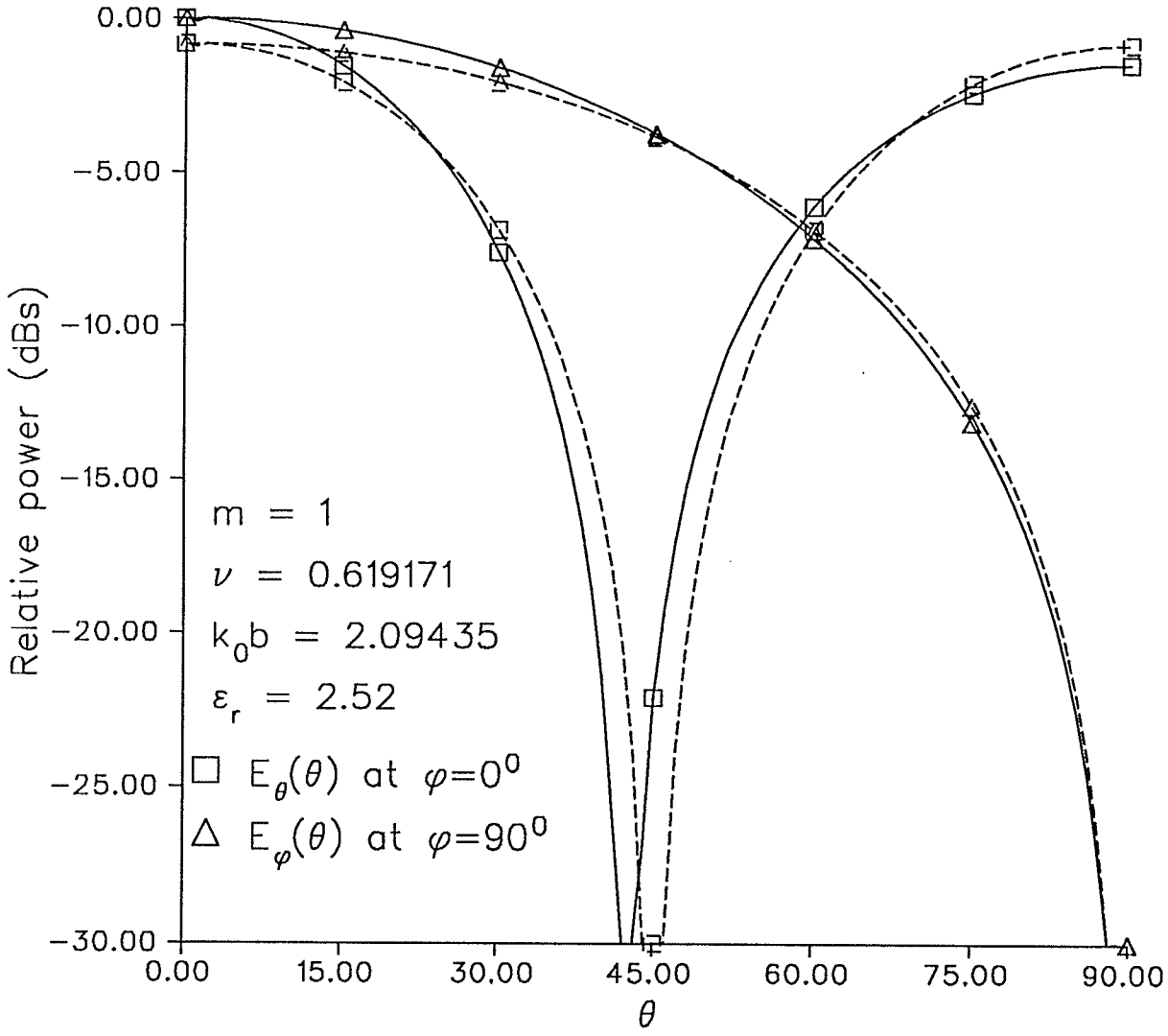

Fig.5.15: Computed radiation patterns for $\Delta\theta=6^0$ and $\theta_2=90^0$

—— Summation of first three radiation modes

---- Only the first mode ($\mu_{11} = 2$)

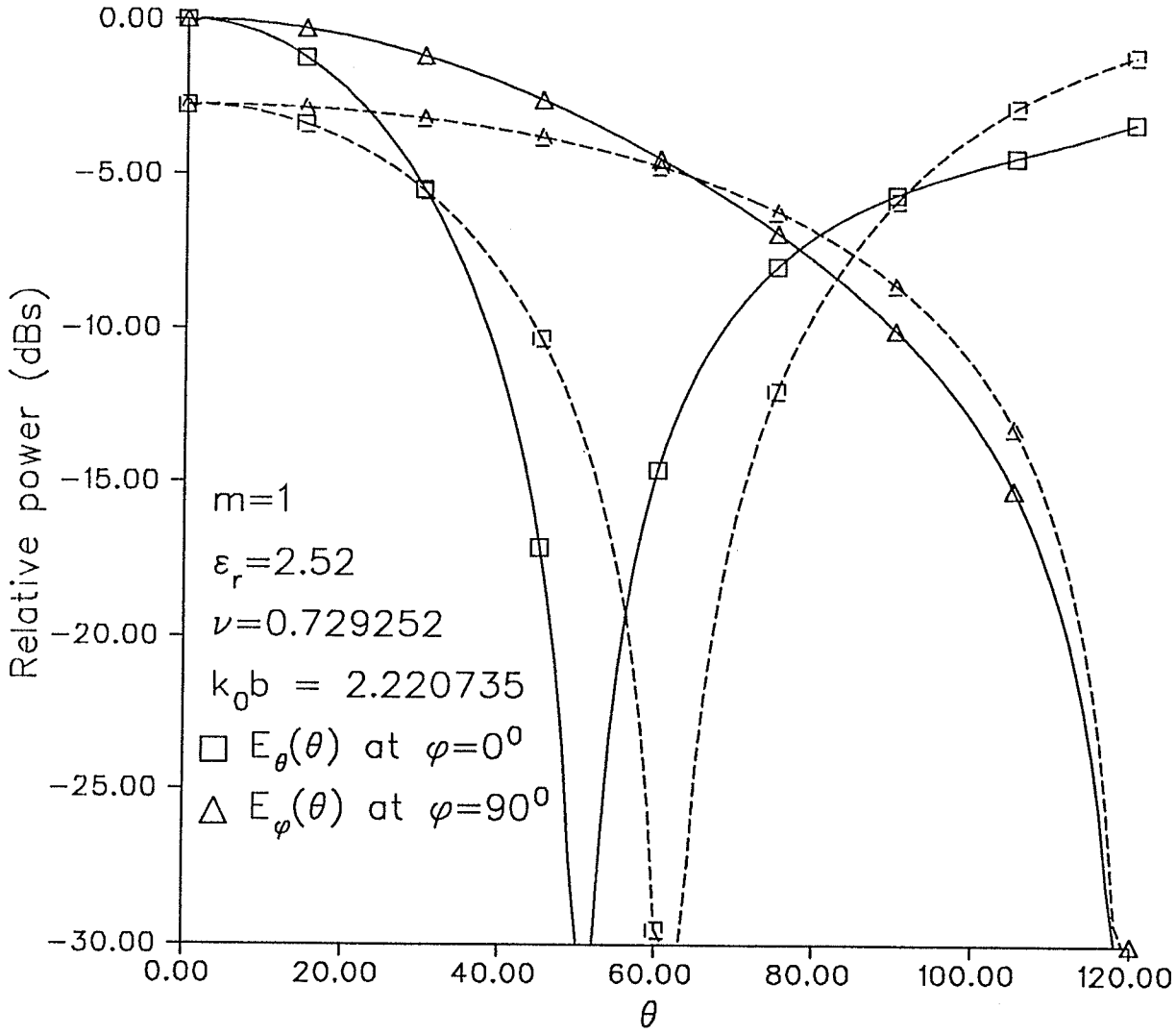

Fig.5.16: Computed radiation patterns for $\theta_2=120^0$ and $\Delta\theta=6^0$

—— Summation of first four radiation modes

--- Only the first mode (μ_{11} = 1.424123)

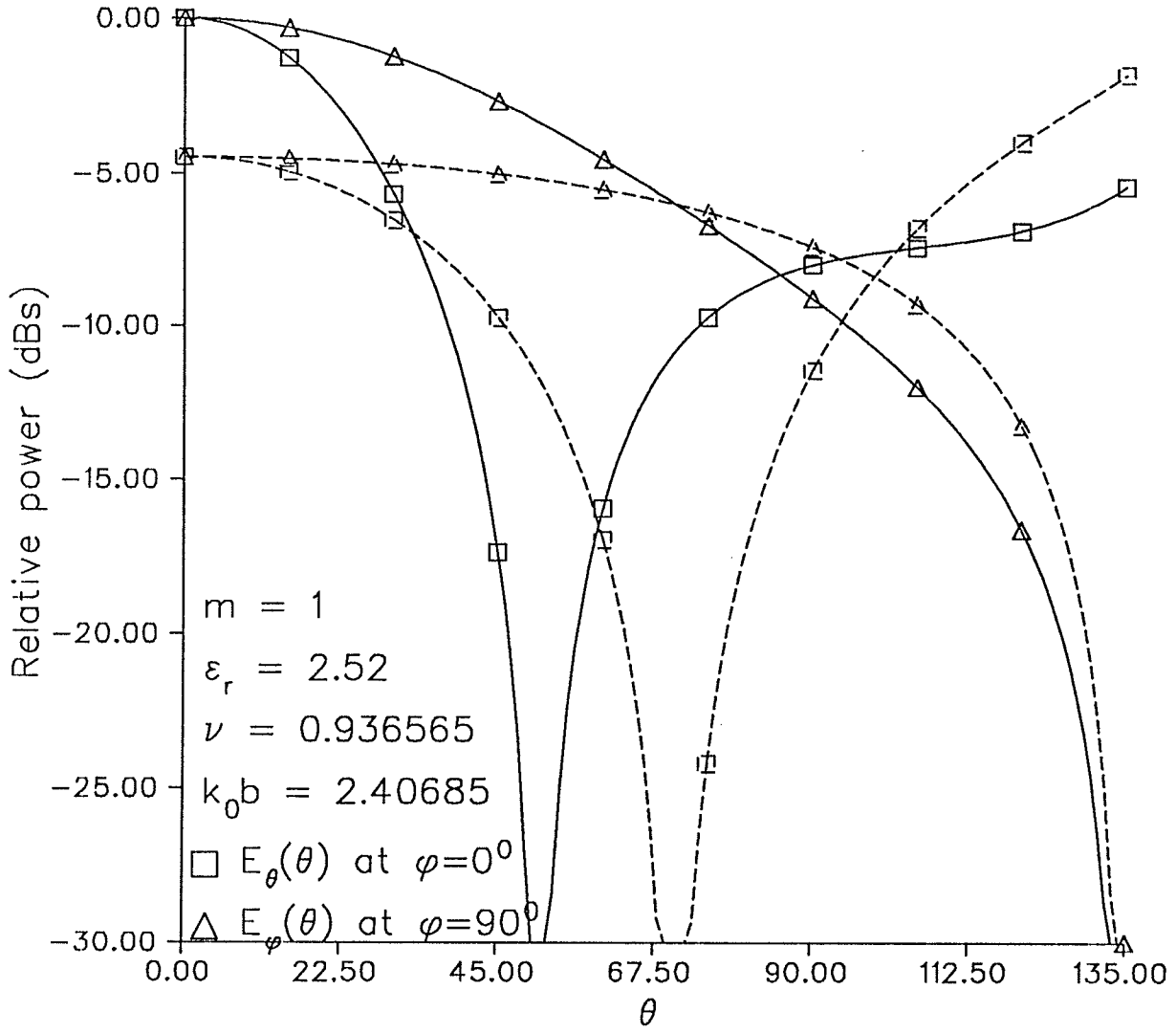

Fig.5.17: Computed radiation patterns for $\theta_2=135^0$ and $\Delta\theta=6^0$

___ Summation of first four radiation modes

--- Only the first mode (μ_{11} = 1.245677)

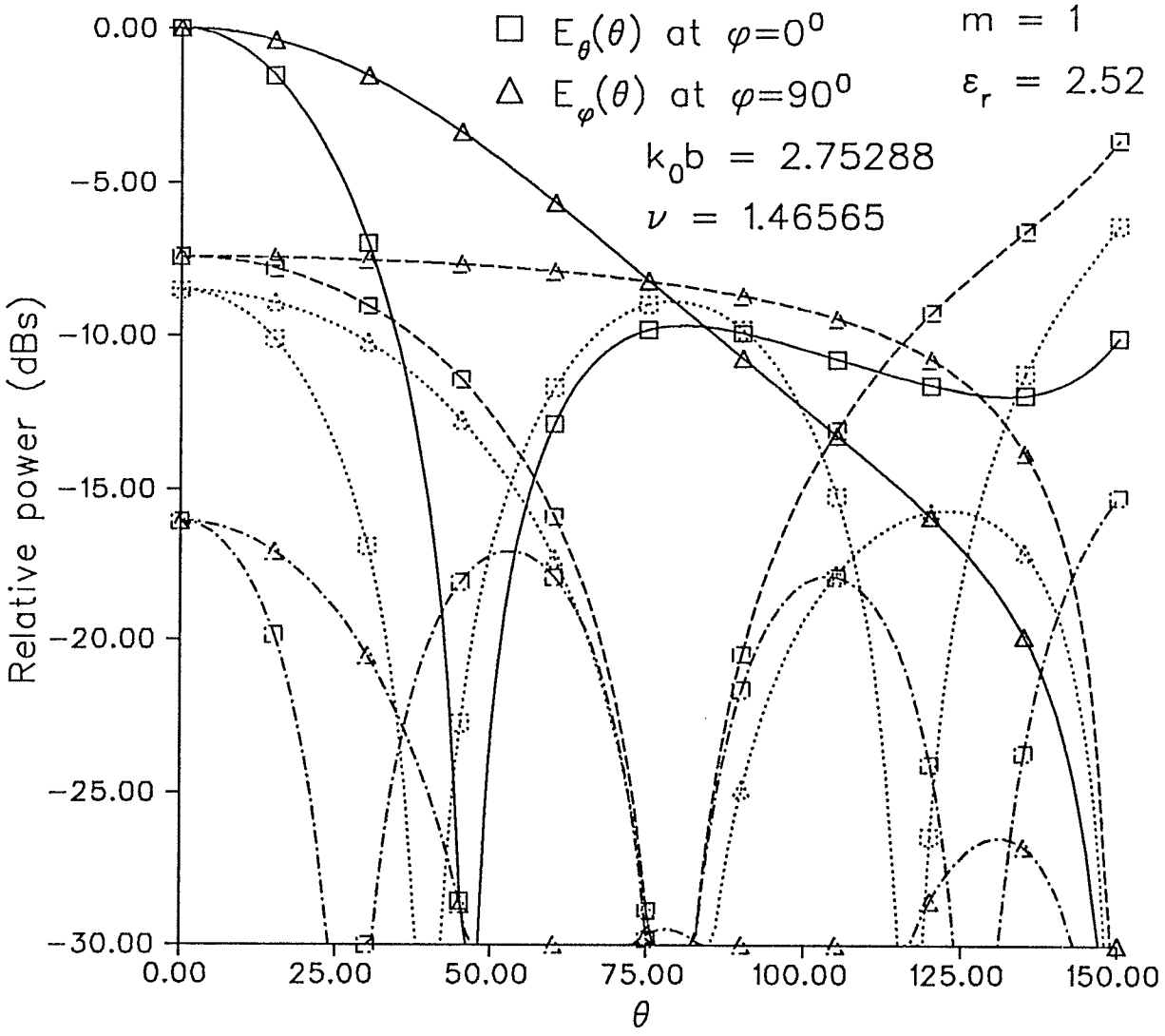

Fig.5.18: Computed radiation patterns for $\theta_2=150^0$ and $\Delta\theta=6^0$

—— Summation of first four radiation modes

---- Only the first mode (μ_{11} = 1.11565)

..... Only the second mode (μ_{11} = 2.27797)

-.-.- Only the third mode (μ_{11} = 3.45786)

Chapter 6
Summary and Further Work

6.1. Summary

Some new types of microstrip antennas were proposed in this dissertation. They were concentrically shorted circular patch microstrip antennas, annular ring patch microstrip antennas shorted at the outer periphery and biconical microstrip antennas. The modal expansion method was used to analyze their characteristics.

The analysis of concentrically shorted circular patch microstrip antennas showed that they are useful antennas with higher gain, improved bandwidth and controllable input impedance values. Their geometry and flexible characteristics provide the antenna designer with adequate parameters for controlling their electrical performance parameters to meet different design specifications.

The good agreement between the analytical and experimental results of the centrally shorted circular patch antennas shows that the modal expansion method was a powerful technique for investigating symmetric resonant structures. The method was, therefore, applied to analyze the annular ring microstrip antenna shorted at the outer periphery and the biconical microstrip antenna.

The study of annular patch microstrip antennas shorted at the outer periphery illustrated that they can provide a wider range of gain, symmetric principal plane patterns and varying input impedance values. Their superior features, when operating at the dominant TM_{11} mode, remedy the poor performance of the conventional annular ring patch microstrip antennas operating at the TM_{11} mode. Their flexible characteris-

tics give the antenna designer ample opportunity to control their electrical performance parameters to satisfy the requirements of different applications.

The investigation of the biconical structures illustrated that only the *TE* modes with nonzero order, which is of interest, can be excited in the structure, and for each mode, a unique eigenvalue ν exists. The antenna was then modeled as a biconical cavity bounded by a finite admittance wall at the spherical surface of its edge. The fields inside the cavity were expanded in terms of the existing cavity modes, i.e., the radial *TE* modes. Their wall admittance was also studied. By applying the equivalence principle to the aperture of the cavity, the fields inside and outside the cavity were linked and the wall admittance was obtained by the radiation power and the energies reactively stored outside the cavity. Their calculated characteristics were shown for a few selected geometries. The analysis showed that they are excellent substitutes for the so called wraparound conformal microstrip antenna. Also, it was shown that the conical microstrip antenna, the special case of the biconical ones, is an excellent alternative for the circular patch microstrip antenna.

With their superior and unique properties, the antennas proposed in this dissertation enlarge the already large microstrip antenna family and extend their use to new applications.

6.2. Recommendation for Further Research Work

A few valuable and interesting problems may be generated from this dissertation.

In the case of annular ring patch microstrip antennas shorted at the outer periphery, the effect of the fringing field at the inner radiating ring may be more delicately studied further either by analytical or numerical methods.

For more accurate analysis of the biconical microstrip antenna, the wall admittance of such structure should be studied as exactly as possible. First, an effort should be made to take all fields outside the cavity into account, i.e., the *TE* modes should be included in the study of the wall admittance or impedance. Second, the wall admittance may be determined more accurately by an attempt to include the effect of the grounded dielectric substrate in the analysis.

Another interesting research topic arising from these new conformal microstrip antennas is the investigation of their variants, such as the ring shape conical and biconical microstrip antennas. Also, the investigation of introducing shorts at the inner or outer periphery of the ring shape conical and biconical microstrip antennas can be an interesting project. One can expect, desirable features may be obtained from the introduction of these shorts.

References

[1] Bahl,I.J., S.S. Stuchly and M.A. Stuchly, "A New Microstrip Radiator for Medical Applications," *IEEE Trans. Microwave Theory and Tech.,* Vol.MTT-28, pp 1464-1468, No.12, December 1980.

[2] Cuhaci,M. and D.S. James, "Radiation from Triangular and Circular Resonator in Microstrip," *IEEE MTT-S Int. Microwave Symp. Digest,* 1977, pp.348-441

[3] K.C. Gupta and B.Bandhauer, "On the design of Wide-band Multiple-Coupled Lines Microstrip Antennas," *IEEE AP-S Int.Symp. Digest,* vol.3, Jun. 1988

[4] C. Wood, "Improved Bandwidth of Microstrip Antennas Using Parasitic Elements," *IEE Proc. Pt.H,* vol.127, No.4, Aug. 1980, pp.231-234.

[5] S.A.Long and M.D.Walton, "A dual-frequency Stacked circular disc antennas," in *Dig. Int. Symp. Antennas Propagat. Soc.,* College Park MD., pp 260-263, May 1978.

[6] I.J.Bahl, P. Bhatia and S. S. Stuchly, "Design of Microstrip Antennas Covered with a Dielectric Layer," *IEEE Trans. on Antennas Propagat.,* vol. AP-30, No.2 May 1982, pp.314-318.

[7] Y. Lin and L. Shafai, "Characteristics of Concentrically Shorted Circular Patch Microstrip Antennas," *IEE Proceedings, Pt.H* Vol.137, No.1, pp.18-24.

[8] Y. Lin and L. Shafai, "A Study of the Annular Ring Patch Shorted at the Outer Periphery," *IEEE AP-S Int. Symp. Digest,* 1990, Vol.1, pp.143-146.

[9] Howell,J.Q., "Microstrip Antennas," *IEEE AP-S Int. Symp. Digest,* 1972, pp.177-180.

[10] Muson,R.E.,"Conformal Microstrip Antennas and Microstrip Phased Arrays," *IEEE Trans. on Antennas and Propagat.,* Vol. AP-22, 1970, pp.74-78.

[11] C. M. Krowne, "Cylindrical-Rectangular Microstrip Antenna," *IEEE Trans. on Antennas and Propagat.,* Vol. AP-31, 1983, pp.194-199.

[12] Das,N and Chatterjee,J.S., "Conically Depressed Microstrip Patch Antenna," *Proc IEE. Pt.H,* Vol. 130, No.3 April 1983, pp.193-196.

[13] A.G. Derneryd, "Linearly Polarized Microstrip Antennas," *IEEE Trans. on Antennas Propagat.,* Vol. AP-24, Nov. 1976, pp.846-851.

[14] A.K. Bhattacharyya and R. Grog, "Generalized Transmission Line Model for Microstrip Patches," *Proc IEE. Pt.H,* Vol.132, No.2 April 1985, pp.93-98.

[15] Y.T. Lo, D.Solomon and W.F.Richards, "Theory and Experiment on Microstrip Antennas," *IEEE Trans. on Antennas Propagat.,* Vol. AP-27, Mar. 1979, pp.137-145.

[16] K.R. Carver and E.L. Coeffy, "Theoretical Investigation of the Microstrip Antenna," *Physic. and Sci. Lab.,* New Mexico State Univ., Las Cruces, Tech. Rep. PT-00929,

[17] L.S.Shen, "Analysis of a Circular-Disc Printed-Circuit Antenna," *Proc.IEE.,* Vol.126, No.12, Dec. 1979, pp.1220-1222.

[18] Y. Lin and L. Shafai, "Eigenvalues of Nonzero-Integer Order Spherical Wave Functions of Coaxial and Biconical Structures," *Antenna Technology and Applied EM Proc.(88),* Winnipeg, August 1988.

[19] Y. Lin and L. Shafai, "Wall Admittance of Biconical Microstrip Antennas," *IEEE Int. Symp. Digest, Vol.1, pp.434-437.* June 1989.

[20] Deschamps, G.A.,"Microstrip microwave Antennas," Presented at the *3rd USAF Symposium On Antennas,* 1953.

[21] J.R. James, P.S. Hall and C. Wood, *Microstrip Theory and Design Peter Peregrinus Ltd.,*

[22] I. J. Bahl and P. Bhartia, *Microstrip Antennas Artech House,* 1980, pp.19

[23] A.K. Bhattacharyya and R. Grog, "Input Impedance of Annular-Ring Microstrip antenna using circuit theory approach," *IEEE Trans., Vol.AP-33, No.4, April 1985, pp.369-374* Vol.132, No.2 April 1985, pp.93-98. Jan. 1981, pp.90-94.

[24] Hasbashy, Tarek M., Jin Au Kong and Wheng Cho Shew, "Resonance and radiation of the elliptic disk Microstrip Structures - I. Formulation," *IEEE Trans., Vol. AP-35,* Aug. 1987, pp.877-886.

[25] R. Chadha and K. C. Gupta, "Green functions for Circular Sectors, Annular Rings and Annular Sectors in Planar Microwave Circuits," *IEEE Trans. Antennas Propagat., Vol. AP-29,* Jan. 1981, pp.68-71.

[26] Bhattacharya, A. K. and L. Shafai, "Method of reducing mode-degeneracy problem in annular-Ring patch antennas," IEE Proc. Pt.H Vol.134 No.6, Dec. 1987, pp.550-556.

[27] P. K. Agrawal and M. Bailey, "An analysis for microstrip antennas," *IEEE Trans., Antennas Propagat., Vol. AP-25,* No.6 Nov. 1977, pp.756-759.

[28] E. H. Newman and P. T. Tulyathan, "Analysis of microstrip antennas using moment method," *IEEE Trans. on Antennas Propagat.,* Vol. AP-29, Jan. 1981, pp.47-53.

[29] M. C. Bailey and D. Deshpande, "Integral Equation Formulation of Microstrip Antennas," *IEEE Trans on Antennas Propagat., Vol.AP-30,0,0,* July 1982, pp.651-656.

[30] David M. Pozar, "Input Impedance and Mutual Coupling of Coax-fed Microstrip Antennas," *IEEE Trans. on Antennas Propagat.,* Vol. AP-30, Nov. 1982, pp.1191-1196.

[31] A. A. Kishk and L. Shafai, "The Effect of Various Parameters of Circular Microstrip Antennas on their Radiation Efficiency and the Mode Excitation," *IEEE Trans. on Antennas Propagat., Vol. AP-34,* Aug. 1986, pp.969-976.

[32] Sullivan Peter L. and Daniel H. Schaubert, "Analysis of an aperture Coupled Microstrip Antennas," *IEEE Trans. on Antennas Propagat., Vol. AP-34,* Aug. 1986, pp.977-984.

[33] Alexopoulos, N.G. and David R. Jackson, "Fundamental superstrate (cover) effect on printed circuit antennas," *IEEE Trans. on Antennas Propagat., Vol.32,* No.6, Nov. 1984, pp.1178-1186.

[34] Y. Lin and L. Shafai, "Moment-Method Solution of the near-field distribution and far-field patterns of microstrip antennas," *IEE Proc., Pt.H, Vol.132* Oct. 1985, No.6, pp.369-374.

[35] T.Itoh and W. Menzel, "A full-wave Analysis method for open microstrip structures," *IEEE Trans. on Antennas Propagat., Vol. AP-29,* Jan. 1981, No.1, pp.63-68.

[36] K. Araki and T.Itoh, "Hankel Transform domain analysis of open circular microstrip radiating structures," *IEEE Trans. on Antennas Propagat., Vol. AP-29,* Jan. 1981, No.1, pp.69-73.

[37] D. Pozar and S. M. Voda, "A Rigorous Analysis of a Microstripline Fed Patch Antenna," *IEEE Trans. on Antennas Propagat.,* Vol.AP-35, Dec. 1987, No.12, pp.1343-1250.

[38] Jeddari, Mahdjoubi, Terret, P. Danisl, "Broadband Conical Microstrip Antenna," *Electronics Letters,* Vol.21, Sept. 1985, No.20, pp.896-898.

[39] W. C. Chew and J. A. Kong, "Radiation characteristics of a circular microstrip antenna," *J. Appl. Phys.,* 51(7), pp.3907-3915, July 1980

[40] S.E. El-Khamy, R.M. El-Awadi and E-B.A. El-Sharrawy, "Simple Analysis and Design of Annular Ring Microstrip Antennas," *Proc.IEE.,* vol.133, Pt.H, No.3, pp.198-202, June 1986

[41] E.E. Collin "Foundations of Microwave Engineering," *McGraw - Hill, New York, 1966*

[42] J. A. Kong, "Theory of Electromagnetic Waves," *John Wiley & Sons, New York, 1975*

[43] S.B. Fouseca and A. J. Giarola, "Microstrip Disk Antennas, Part I: Efficiency of Space Wave Launching" *IEEE Trans. Antennas Propagat.,* vol. AP-32, pp.561-567, June. 1984

[44] Lier, E, "Rectangular microstrip patch antennas," (Ph.D. thesis, Univ. Trondheim, Norway, 1982)

[45] A.C. Ludwig, "The Definition of Cross Polarization," *IEEE Trans. Antennas Propagat.,* Vol. AP-21, pp.116-119, Jan. 1973

[46] H. Arai and N. Goto, "A Ring Cavity Antenna of Wide beamwidth," *1989 IEEE AP-S Int. Symp. Digest,* Vol.III, pp.1316-1319, 1989.

[47] Wolf, "Antenna Analysis," *1989 IEEE AP-S Int. Symp. Digest,* Vol.III, pp.1316-1319, 1989.

[48] Weng Cho Chew and Jin Au Kong, "Effect of Fringing Fields on Capacitance of Circular Microstrip Disk," *IEEE Trans., Microwave Theory Tech.,* Vol. MTT-28, pp.98-104, 1980.

[49] K. Minderhoud, A Microstrip Antenna Design for Use in Globe Positioning System," (Bachlor Thesis, Univ. of Manitoba, Canada, 1990)

[50] C.T.Tai,"On the Theory of Biconical Antennas," *J.Appl.Phys.,* Vol.19, pp.1155-1160,1948

[51] J.R.Wait,"Electromagnetic Radiation from Conical Structures," in Antenna Theory, Part I by R.E.Collin and F.J.Zucker, *McGraw-Hill,* New York, Chap.12, 1969

[52] R.H.Harrington, "Time-Harmonic Electromagnetic Fields," *McGraw-Hill,* New York, 1961

[53] M.Abramovitz and F.Oberhettinger, "Handbook of Mathematical Functions," *Dover Pub.Inc.,* New York, 1970

[54] W.Magnus, F.Oberhettinger and R.P.Soni, "Formulas and Theorems for the Special Functions of Mathematical Physics," *Springer-Verlag* vol. AP-32, pp.561-567, June. 1984

[55] K. R. Carver and J. W. Mink, "Microstrip Antenna Technology," *IEEE Trans. Antennas Propagat.,* Vol. AP-29, pp.2-24, Jan. 1981.